Dissertation ETH No. 19175

High-speed acousto-optic imaging of neuronal network activity in the intact mouse brain

A Dissertation submitted to
ETH ZURICH
for the Degree of Doctor of Sciences

Dissertation presented by

Benjamin Friedrich Grewe
Diplom Physiker, University of Heidelberg
born December 14th, 1980, Ahlen, Germany

accepted on the recommendation of

Prof. Dr. Richard Hahnloser, examiner ETH
Prof. Dr. Fritjof Helmchen, co-examiner UNI-ZH
Prof. Dr. Markus Rudin, co-examiner ETH

Year 2010

High-speed acousto-optic imaging of neuronal network activity in the intact mouse brain

"Ein Abend, an dem sich alle Anwesenden völlig einig sind, ist ein verlorener Abend."

Albert Einstein

Summary

High-speed acousto-optic imaging of neuronal activity in the intact mouse brain.

In the mammalian brain stimuli that are received from the outer world are represented as coordinated patterns of activity in neuronal populations. These patterns are processed, integrated and evaluated in higher-order brain areas on a time scale that ranges from a few to hundreds of milliseconds. Investigating these neuronal activity pattern therefore requires a measurement technique that provides an adequate temporal resolution. While large-scale electrical recordings can measure population spiking activity in behaving animals, the speed of optical neuronal activity measurements so far has been limited to several Hertz (1-30 Hz typical rate). Nevertheless optical methods feature some crucial advances compared to electrical measurements, such as the possibility to sample complete local network populations, the revealing of specific cell types, the detection of inactive neurons and they enable to obtain spatial relationships of individual neurons within their network.

Overcoming previous scanning speed limitations, here we demonstrate a novel improved version of a 2-photon laser scanning microscope for *in vivo* imaging that employs an orthogonal pair of acousto-optic deflectors (AODs) which allowed real-time measurements of neuronal network activity. Using an effective dispersion compensation unit (DCU) we compensated for the dispersive effects that were caused by the AOD-scanners and succeeded to reshape the laser beam profile and the laser pulse length. Further microscope optimizations for best laser beam transmission resulted in a total transmission efficiency of about 25% (700 mW) below the objective. These optimizations together rendered our system suitable for *in vivo* imaging down to a depth of approximately 300 μm. The lateral microscope resolution of 1-1.6 μm thereby allowed a clear identification of neuronal cells and cell somata; axial resolution was 4.1-6 μm. The maximum total scanning field of 305 μm x 305 μm contained up to 200 neurons.

Employing a novel random-access-pattern-scanning (RAPS) mode with acousto-optic deflectors we were able to perform *in vivo* calcium imaging of mouse neocortex with greatly improved temporal resolution and obtained fluorescence measurements from 34-91 layer 2/3 neurons at 180-490 Hz sampling rate. Most important, the new scanning mode enabled us to detect single action potential-evoked fluorescence calcium transients with a signal-to-noise ratio of 2-5. In addition high-speed RAPS imaging of neuronal somata allowed us to determine neuronal spike times with a precision of a few milliseconds (5-15 ms). For analyzing higher frequent trains of action potentials we developed a new automated 'peeling' algorithm that enabled to reconstruct more complex spike trains from superimposed calcium fluorescence traces of up to 20-30 Hz AP-frequency.

Demonstrating the potential of the new AOD-scanning technique we could resolve spatiotemporal trial-to-trial variability of sensory evoked neuronal spiking responses for cell populations in the barrel and visual cortex of mice. We think that AOD 2-photon laser scanning in combination with RAPS and with an automated spike reconstruction will facilitate real-time investigations in neuronal network activity and thus will help to gain a more detailed understanding of how incoming information is processed in local neuronal networks of the mammalian brain. We assume that a better understanding of the modes of neuronal network operation finally also may help to analyze dysfunctions of such neuronal networks which are prevalent in several brain diseases.

Zusammenfassung

Schnelle akusto-optische Messungen neuronaler Netzwerkaktivität im intakten Gehirn von Mäusen.

Sinnesreize aus der uns umgebenden Welt werden im Gehirn in Form von definierten elektrischen Erregungsmustern in dichten Netzwerken von Nervenzellen abgebildet. Die Reizverarbeitung geschieht dabei über die zeitliche Abfolge von Nervenzellimpulsen, welche sich üblicherweise innerhalb einiger Tausendstel bis Hundertstel Sekunden abspielt. Um die Informationsverarbeitung in neuronalen Netzwerken zu verstehen, ist es daher entscheidend, Messmethoden mit hinreichender zeitlicher Auflösung zu entwickeln. Während direkte elektrische Messungen neuronaler Aktivität mit Hilfe von Elektroden eine sehr hohe zeitliche Auflösung bieten, können optische Messungen bisher die neuronalen Impulsmuster nur ungenügend, mit einigen Hertz, auflösen (max. 10-15 Hz Messrate). Trotzdem bieten optische Messmethoden gegenüber elektrischen entscheidende Vorteile wie z.B. die Möglichekiet, komplette Zellnetzwerke zu messen, spezielle Zelltypen zu unterscheiden oder auch die räumliche Organisation der Neuronen mit einzubeziehen.

Im Hinblick auf die Geschwindigkeit bei optischen Messungen ist es im Rahmen dieser Arbeit nun gelungen, ein neuartiges 2-Photonen Mikroskop zu entwickeln, welches über zwei orthogonal angeordnete akusto-optische Deflektoren (AODs) schnelle Echtzeitmessungen neuronaler Aktivität erlaubt. Mit einer effektiven Kompensation der rämlichen und zeitlichen Dispersionseffekte, welche von den akusto-optische Kristallen erzeugt werden, gelang es, das Anfangsprofil des Laserstrahls und die ursprüngliche Pulslänge wiederherzustellen. Die Laserstrahltransmission des optimierten Mikroskops erreichte dabei ca. 25%, was ca. 700 mW unter dem Objektiv entspricht. Die maximal verfügbare Laserintensität ermöglichte *in vivo* Messungen neuronaler Aktivität in Gewebetiefen bis zu 300 μm. Die laterale Auflösung des AOD-Mikroskops von 1-1,6 μm reichte aus, um Zelltypen und neuronale Zellsomata eindeutig zu identifizieren (z-Auflösung 4.1-6 μm). Das gesamte 2D-Scanfeld von 305 μm x 305 μm beinhaltete dabei bis zu 200 Neurone.

Unter Verwendung einer neu entwickelten Scanning-Methode (RAPS), bei dem kleine Punktraster innerhalb der Neurone gescannt werden, war es möglich, Kalziumfluoreszenzsignale von 34-91 Neuronen in neokortikaler Schicht 2/3 mit Messraten von 180-490 Hz aufzunehmen. Dabei erlaubte es die neue RAPS-Messmethode, sogar Kalziumfluoreszenzsignale aufzunehmen, welche durch einzelne neuronale Zellimpulse erzeugt wurden (Signal-Rausch-Verhältnis von 2-5). Zudem war es möglich, die Impulse der Nervenzellen mit einer Genauigkeit von 5-15 ms zu rekonstruieren. Auch höher frequente Zellaktivität, welche zu Überlagerungen der Kalziumsignale führt, konnte mit Hilfe eines neu entwick-

elten Algorithmus zur automatischen Fluoreszenzdatenanalyse bis zu einer Aktivitätsfrequenz von 20-30 Hz aufgelöst werden.

Durch Anwendung der neuen AOD-Scantechnik gelang es uns, zeitlich und räumlich verteilte Aktivität von neuronalen Zellpopulationen im barrel-Kortex und im visuellen Kortex von Mäusen bei wiederholter Stimulation aufzunehmen. Wir denken, dass die schnelle AOD 2-Photonen Laser Scantechnik in Kombination mit dem RAPS Scanverfahren und dem Algorithmus zur automatischen Fluoreszenzdatananlyse in Zukunft optische Echtzeitmessungen neuronaler Aktivität ermöglichen wird. Mit dem neuen Messverfahren lässt sich demnach die Informationsverarbeitung in neuralen Netzen des Gehirns sehr viel detaillierter und umfassender untersuchen und auch visualisieren. Ein verbessertes Verständnis der Prinzipien der normalen, nicht gestörten Informationsverarbeitung im Gehirn kann letztendlich auch für die Erforschung von Fehlfunktionen neuronaler Netzwerke wie zum Beispiel bei Hirnerkrankungen von entscheidendem Vorteil sein.

Contents

1 Introduction

The human brain is probably one of the most complex structures that is known to current science. Containing hundreds of millions of densely interconnected neurons that communicate on a fast time scale, it is responsible for generating behavior, emotions, memories and our thinking. Although the roots of brain research can be traced back to the ancient Greeks, most of the current knowledge about our brain has been gained during the last 200 years. During this period the introduction of new technologies essentially helped researchers to investigate the brain and its function on a more detailed level that today ranges from the macroscopic scale down to molecular dimensions of some nanometers. Understanding the basic working principles of our brain throughout these scales no doubt will also help to understand and characterize prevailing brain diseases such as epilepsy or depression that are probably caused by dysfunctions of local brain circuits.

We hope that the novel *in vivo* high-speed scanning microscopy technique described in this work will further facilitate investigations of fast neuronal activity and thus help gaining new insights into the dynamics of neuronal networks in the brain.

1.1 A short history of brain research

In the 6^{th} century BC the ancient Greeks had already begun to postulate that the location of our mind and our thinking is located in our brain. Alcmaeon of Croton, one of the most eminent natural philosophers and medical theorists, dissected the optic nerve and identified its connection to the brain. He also theorized about how sleep could be mediated by the brain. Nevertheless other Greeks also had divergent theories regarding the function of the brain. Hippocrates for example, an old Greek physician who lived in the 3^{rd} century BC and probably one of the most outstanding figures in the history of medicine, pointed to the brain as the origin of intelligence, while his later colleague and famous philosopher Aristotle believed the heart to be the source of all intelligence.

Several hundred years later most of the neuroscience research was done by some Islamic scientists. One of the most notable achievements during this time was made in the 10^{th} century AC by Najab ud-din Muhammad who identified a number of psychiatric disorders that may afflict humans. Among these findings he detailed psychiatric diseases that we know today as mania, psychosis, depression and neurosis. Also within the next few centuries a number of other symptoms related to dysfunctions of the brain were identified as hallucinations, dementia, vertigo and stroke.

A major breakthrough of brain research has been made during the late 1900s which included the use of one of the first microscopes. Two excellent scientists Camillo Golgi and Santiago Ramon y Cajal both discovered the existence of neurons as a basic working unit within the network structure of our brain. In 1906 they shared the Nobel Prize in Physiology or Medicine. Throughout the last few decades the study of the brain continued moving into physiological, chemical and molecular research and became generally known as neuroscience. In the late 20^{th} century until today people enormously have got benefit from the development of new fast measurement techniques such as electrical and optical recordings of neuronal activity that in combination with automated computer analysis allow the investigation of neuronal systems on scales that range from some *centi*meters down to some *micro*meters.

1.2 The structure of the brain

While the complex biological structure of the brain can substantially differ across species some common principles of brain architecture are conserved across a wide range of mammalian brains. Inferred from neuroanatomical studies it is well known that the brain consists of six main regions: the telencephalon (cerebral hemispheres), the diencephalon (thalamus and hypothalamus), the mesencephalon (midbrain), the cerebellum, pons and medulla oblongata [Kandel et al., 2000]. All of these areas have an individual macroscopic structure but if we would make more fine distinctions on the basis of neural structure, chemistry and connectivity thousands of distinguishable brain regions could be defined. Some of these macroscopic structures such as the cortex have evolutionary folded over hundreds of centuries to fit within the available space of the skull and consist of several cell layers. Other brain regions such as the olfactory system contain clusters of many small nuclei. Because the cerebral cortex is greatly enlarged in primates and even more in humans it represents the part of the brain that most clearly distinguishes mammals from other vertebrates.

Localized functional units in the brain. The idea to further divide the cortex into sub regions with respect to their functionality is described in detail by numerous investigations that refer to the so called 'brain mapping' [Yu et al., 2005, Otzenberger et al., 2005, Ogawa et al., 1992]. The first knowledge about functional units within the brain was gained during medical dissections; the neurologist Broca first noticed that one of his speech disorder patients had a small lesion within the 3^{rd} winding of the frontal lobe [Broca, 1861]. Because windings of the neocortex were individually folded during evolution, they are not appropriate structures to define functional sub regions of the mammalian brain. More recently Welker and Wolley [Welker and Woolsey, 1974] could show that on the other hand the somatosensory system of rats could be well defined and identified as a sub region of the cortex. In addition they could confirm that within the primary sensory cortex all sensations were represented with respect to their importance of perceiving sensory input from the outer world. To illustrate this the functional representation of the somatosensory cortex and the visual cortex of a rat is shown in Figure 1.1.

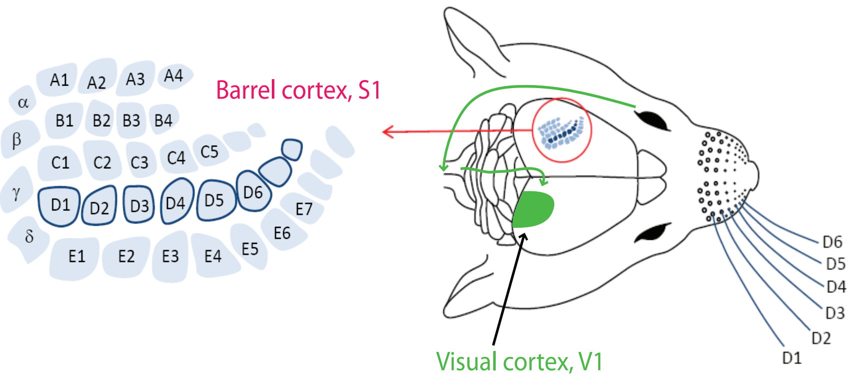

Figure 1.1: *Visual and somatosensory cortex (S1 and V1) of a mouse brain (right). Within the somatosensory system every whisker is represented by a barrel like structure (left scheme) that processes incoming sensory information. Also in the visual cortex the representation of visual receptive fields is translated into small functional brain areas.*

The cortical layers. Because of the characteristic distributions of cell types and the prevalence of afferent as well as efferent connections to other cortical regions the cortex can be divided into several layers. Staining across the cortical areas allowed neuroanatomists in the early 20^{th} century to reveal the position of neuronal cell bodies and the intra-cortical axon tracts [Brodmann, 1909]. Thus they were able to develop a detailed description of the laminar structure including all cortical layers of the cortex for different species. Finally Korbinian Brodmann could show in 1909 convincingly that the cerebral neocortex in the mammalian brain can be grouped into six cortical layers, ranging from the pial surface to the white matter. The cortical layer representation is arranged as follows:

- **I Lamina molecularis** (contains few scattered neurons as well as glial cells)
- **II Lamina granularis externa** (afferent; contains small pyramidal neurons, numerous stellate neurons and some inter-neurons)
- **III Lamina pyramidalis externa** (aff-/efferent; predominantly small and medium-size pyramidal neurons as well as non-pyramidal neurons)
- **IV Lamina granularis interna** (afferent; contains different types of stellate, pyramidal neurons and some inter-neurons)
- **V Lamina pyramidalis interna** (efferent; contains mostly large pyramidal neurons and some inter-neurons)
- **VI Lamina multiformis** (efferent; contains few large pyramidal neurons and many small spindle-like pyramidal neurons and inter-neurons)

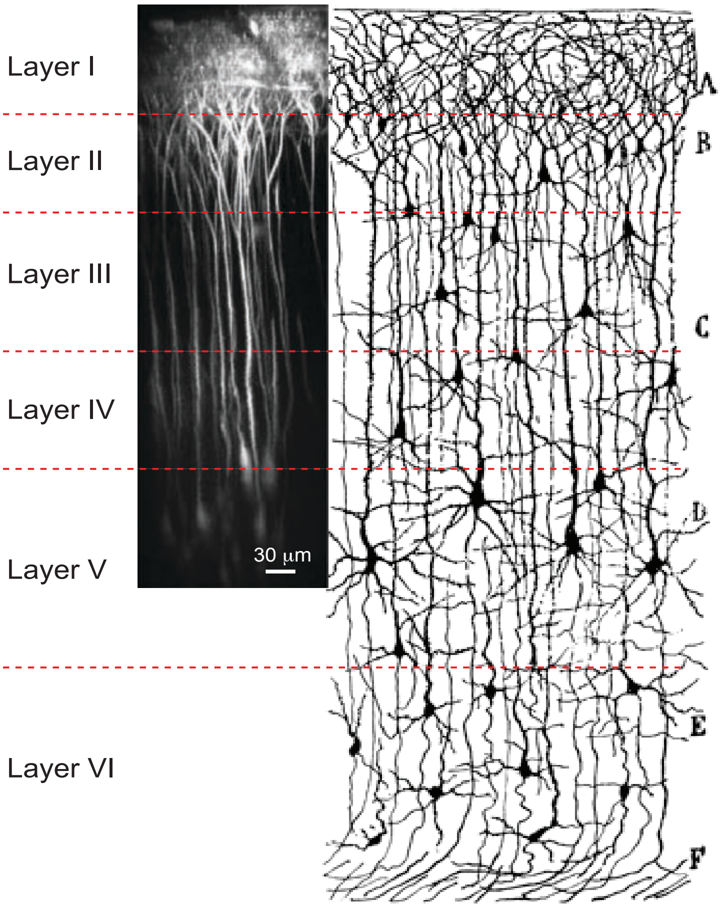

Figure 1.2: *Six layers of the mouse neocortex (right) adapted from Santiago Ramon y Cajal 1904; fluorescence image of stained layer 5 pyramidal cells 26 years later (left), adapted from [Engelbrecht* et al.*, 2009]. The left image was taken with a 2-Photon Laser Scanning Microscope (2PLSM) that enabled to acquire images within the living brain of mice.*

1.3 Levels of research investigation

The human and the animal behavior as well emerge from neural computations that are implemented across spatial scales from the microscopic level of synapses to the macroscopic level of interconnected brain areas. The latter can be investigated by electroencephalography (EEG) that enables to record the intrinsic electrical signals of the brain or by functional magnetic resonance imaging (fMRI) that can be tuned to measure changes in blood oxygen concentration (BOLD contrast), cerebral blood volume (CBV) or flow (CBF) in response to sensory stimulation (for rev. see [Rudin et al., 2003]). At the intermediate, the mesoscopic level, where single neurons can be identified, neural information processing occurs in complex microcircuits containing up to tens of thousands of excitatory and inhibitory neurons. Table 1.1 and Figure 1.3 illustrate the different scales of the brain.

Scales of the Brain	Extend
Nervous System	1 m
Brain	10 cm
Brain Regions	1 cm
Neuronal Networks	1 mm
Neurons	100 μm
Synapses	1 μm
Molecules/Atoms	1 nm

Table 1.1: Levels of brain research investigations adapted from Churchland [Churchland and Sejnowski, 1992]

The first approach to probe extended neuronal networks at the 'mesoscopic' level were single electrode recordings. Today multi-electrode recordings enable to measure population spiking activity in behaving animals [Churchland et al., 2007], but they sample only a small fraction of the underlying local network and are limited in revealing individual cell types or the spatial organization of the network. As an alternative approach optical imaging techniques such as 2PLSM in combination with functional fluorescent indicators are rapidly developing [Kerr and Denk, 2008, Wilt et al., 2009, Grewe and Helmchen, 2009]. The main advantage of optical techniques is that they allow to investigate spatiotemporal dynamics of well-identified neuronal populations with single-cell resolution and in living animals.

1.3.1 Neuronal Networks

An essential part of understanding the brain's function is the characterization of large scale neuronal networks that consist of smaller neuronal microcircuits. These networks can process visual, sensory or auditory information that is coming from the outer world as coordinated activity patterns via defined neuronal populations. In the next step these activity patterns are further interconnected, integrated and sent into higher-order brain areas eventually resulting in activity patterns of motor neuron populations that finally generate behavior.

The human brain for example consists of about 10^{10} - 10^{12} densely packed neurons that are highly interconnected via their axons and dendrites. Building up higher order networks that enable feature extraction of incoming information, each single neuron within such a network is capable to receive and integrate information and to project the result to downstream neurons. In many cases connections between single neurons are not unidirectionally organized and thus can create positive and negative feedback-loops that enable very localized processing by forming a dense local microcircuit connectivity [Douglas et al., 1995]. These highly interconnected networks thus can mediate diverging or converging information flow over large scales of the brain and across different networks.

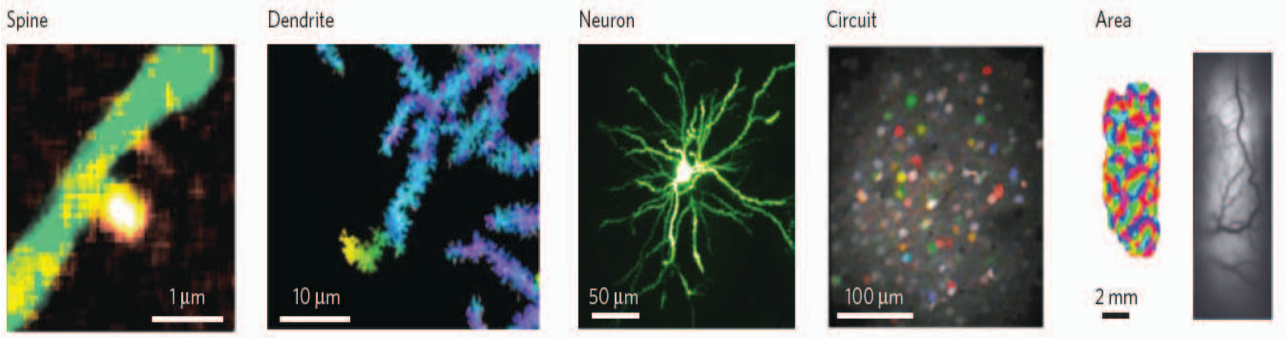

Figure 1.3: *The primary strength of imaging approaches is their spatial resolution allowing physiological events to be localized with high spatial precision over a wide range of scales. Representative examples shown are of calcium compartmentalization in a single hippocampal* ***spine*** *measured using a genetically encoded calcium sensor and 2PLSM; local calcium transient triggered by parallel-fibre synaptic input to a fine spiny branchlet in the* ***dendritic tree*** *of a cerebellar Purkinje cell; a layer-2/3* ***pyramidal neuron*** *filled with a calcium dye and visualized in mouse visual cortex in vivo using 2PLSM; an orientation* ***circuit*** *map in rat visual cortex measured using 2PLSM; optical imaging of voltage-sensitive-dye fluorescence to record receptive-field properties across an* ***area*** *of cat visual cortex (adapted from [Scanziani and Hausser, 2009])*

During the course of neuronal activity key steps of information processing also occur on the level of local microcircuits that contain up to ten thousand cells (for reviews see [Grillner et al., 2005, Luebke and Feldmeyer, 2007, Silberberg et al., 2005]). In the neocortex each neuron has been estimated to project to an average of 10,000 postsynaptic neurons while receiving about the same number of synaptic inputs from presynaptic cells. Whereas connections between cells could be morphologically characterized across different cortical layers and generalized to some extent [Douglas and Martin, 2004, Luebke and Feldmeyer, 2007, Silberberg et al., 2002, Lefort et al., 2009] it is poorly understood how local networks process and integrate incoming signals during ongoing brain activity. A simple reason is that experimental techniques to measure neuronal networks are still limited as this would require comprehensive measurements of spatiotemporal dynamics from several thousands of neurons *in vivo* with a suitable temporal resolution in time.

Performing such measurements would allow to describe the dynamic organization of a local population with n neurons by the temporal evolution of the n-dimensional brain-state vector which contains 1 for all active, action potential-generating cells and 0 for all inactive cells [Buonomano and Maass, 2009]. In addition hidden states reflecting sub threshold membrane potential or second messenger concentrations can dynamically change as well and may influence network dynamics significantly. For distinct sensory inputs or behaviors the trajectory of the brain-state vector then passes through particular sub-volumes of the high-dimensional state space which corresponds to specific sequences of co-active ensembles of neurons that are engaged during particular computational tasks. To understand the principles of microcircuit operation we need to identify these coactive ensembles within local neuronal populations and reveal their dynamic properties when performing real tasks.

Despite of fundamental importance of information propagation and processing in these neuronal populations the underlying principles and dynamic organization of neural networks including their subunits remain poorly understood. The aim of this work is was to advance optical imaging with the primary objective to record from a larger set of neurons *in vivo* with a time resolution close to milli-seconds.

1.3.2 Neurons

In 1891 Ramon i Cajal described in his 'neuron doctrine' that our nervous system consists of discrete individual cells. Activity measurements of these 'cells' to further confirm his theory were hardly even possible and had to wait till the introduction of new techniques such as sharp electrode recordings in the early 1950s or the patch clamp technique (1976) that allowed to directly record intra-cellular electrical activity (for rev. see [Sakmann, 2006]) which at the end confirmed the hypothesis that the neuron is the main information processing cell type in the central nervous system (CNS). First measurements revealed that neurons were electrically excitable and were able to integrate and encode information via changes of their membrane potential. If a certain threshold above their resting membrane potential is reached, a so called 'action potential' (AP) can be triggered at the axon hillock. The AP propagates along the axon where axonic boutons form synapses together with post-synaptic target neurons. Upon arrival of an action potential at an axonic bouton of the presynaptic cell neurotransmitter molecules are released which cause the opening of ligand gated postsynaptic ion channels in the postsynaptic cell. Whether the postsynaptic cell is excited or inhibited by this projection depends on the neurotransmitter that is released. Depending on the type of neurotransmitter excitatory inward currents (e.g. glutamate) or inhibitory outward currents (e.g. GABA) can be induced. Postsynaptic neurons usually integrate these excitatory and inhibitory postsynaptic potentials (EPSP or IPSP respectively) via their dendrites and at the soma which then, if the threshold is reached, can trigger again an action potential at the soma of the postsynaptic cell. In the simplified case the electrical activity of a neuron could be characterized by the initiation of an 'action potential' that represents '1' in information coding, whereas '0' would represent the neurons electrical baseline. This approach is of further importance to simplify the investigations in large sets of interconnected neurons that build up neuronal networks.

The majority of neocortical neurons in the mammalian CNS possess elaborated axons and dendrites that form numerous synaptic contacts with their post- and pre-synaptic partners. Featuring diverse morphological and physiological properties which are essential for synaptic integration neurons can process incoming signals within smaller neuronal circuits [Hausser et al., 2000, Yuste and Tank, 1996].

1.4 Probing neuronal activity in the intact brain

Extracellular electrical recordings are the classical method to measure neuronal population activity. To sample the extracellular local field potential which originates from the activity of many neurons a thin single wire can be directly inserted into the brain. Alternatively several improved techniques that use tetrodes, electrode arrays or silicon probes allow more detailed electrical recordings from neuronal cell populations (for rev. see [Scanziani and Hausser, 2009]). While large-scale electrical recordings can in principle measure population spiking activity in behaving animals [Churchland et al., 2007] they sample local networks only sparsely and are limited in revealing cell types or spatial relationships. These needs have increased the prominence of optical recording techniques such as 2-Photon Laser Scanning Microscopy (2PLSM) that has revolutionized fluorescence imaging by enabling relatively deep imaging down to several hundred microns in optically thick, light scattering tissue *in vivo* [Denk et al., 1990, Zipfel et al., 2003, Larson et al., 2003]. In particular 2-photon microscopy of functional fluorescent indicators provides new opportunities for measuring the spatiotemporal dynamics of well-identified neuronal populations with single-cell resolution. In addition 2PLSM [Denk et al., 1990] has the particular advantage to enable calcium imaging in the working brain (reviewed in [Helmchen and Denk, 2005]). Providing a penetration depth of several hundred microns in the intact tissue 2PLSM is excellently suited to study the structure and function of cells and neuronal networks within their native environment (for rev. see [Grewe and Helmchen, 2009, Kerr et al., 2005].

1.4.1 Principles of 2-Photon Laser Scanning Microscopy (2PLSM)

The first concept of a 2PLSM was demonstrated in 1990 by W. Denk and D. Webb [Denk et al., 1990]. By now 2PLSM has become the prevailing method for imaging in highly scattering tissue and has subsequently been applied to various types of tissues. Perhaps the most interest within the neuroscientific field of research was gained by the use of 2-photon imaging in the intact brain of living animals (*in vivo*). While the theoretical basis of 2-photon absorption processes has already been described in 1931 by Maria Goppert-Mayer [Göppert-Mayer, 1931] the experimental observation of the 2-photon absorption or excitation process had to await the invention of the laser, because typical 2-photon cross-sections for dye excitation are extremely small [Kaiser and Garret, 1961, Svoboda et al., 1997]. Today excitation efficiency has been further increased by using high-power titanium sapphire (Ti:Sa) laser oscillators that generate short femtosecond laser pulses and thus provide high photon densities that allow a sufficient level of 2-photon excitation within the focal spot (Fig. 1.4). This section explains the basic principles of the 2-photon excitation used for 2-photon laser scanning microscopes, followed by a short description of the standard instrumentation to build up a 2-photon microscope for *in vivo* imaging.

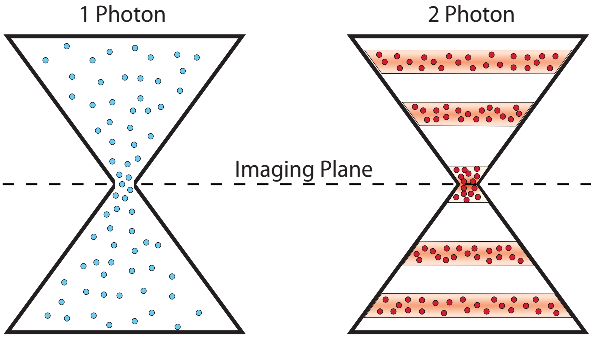

Figure 1.4: *Photon particle view of the single- and 2-Photon absorption process. Fluorescence excitation for 1- and 2-photon microscopy. In confocal microscopy a continuous wave ultraviolet or visible light laser excites fluorophors throughout the volume. In 2-photon microscopy an infrared laser provides pulsed illumination such that the density of photons is sufficient for simultaneous absorption of 2-photons. Thus fluorescence excitation is mainly restriceted the focal point.*

The 2-photon excitation process. 2-photon microscopy is based on a simultaneous absorption of 2-photons within time-windows of less than 10^{-15} s. The resulting transition of the molecule's energy state can alternatively be induced by a single photon with half the wavelength or twice the energy. During single photon absorption processes fluorophors are excited from the initial energy ground state to a higher vibrational energy state. For an efficient excitation the energy difference between these two states has to match the energy of the absorbed photon ($\Delta E_{1P} = E_1 - E_0$) whose energy E is given by $h\nu_{1p}$ with h the Planck constant and ν_{1p} the light frequency (Fig. 1.5). The exited molecule is now in a higher energy state and will relax with a certain probability to it's original ground state by emitting a single photon. Due to some smaller preceding vibrational relaxations to the lowest vibrational energy levels of the excited state the energy of the fluorescence photon is typically slightly lower than the energy of the excitation photon. This results in a slight positive shift of the wavelengths of the excitation compared to the emission photons which is also known as Stoke's shift. Additionally excitation of dye molecules to a higher energy state can be induced by the absorption of two or even more photons. Assuming a mathematical virtual level after the first photon is absorbed the theory allows the absorption of a second photon with basically the same energy to reach the final state of excitation. While the total energy difference ($\Delta E = E_1 - E_0$) of the molecule's energy state is conserved this energy difference can also be provided by absorbing 2 photons of half the energy.

As most fluorescent dyes absorb light within the visible spectral range (single photon absorption) near-infrared light is often used for microscopic applications that employ of the 2-photon excitation principle. In general the 2-photon absorption spectra of dyes are rather broad [Svoboda and Yasuda, 2006] which has the advantage that green and red fluorescent dyes can be excited simultaneously using the same wavelength. Because most of the dye molecules show extremely small 2-photon cross-sections it is essential to concentrate photons in space and time.

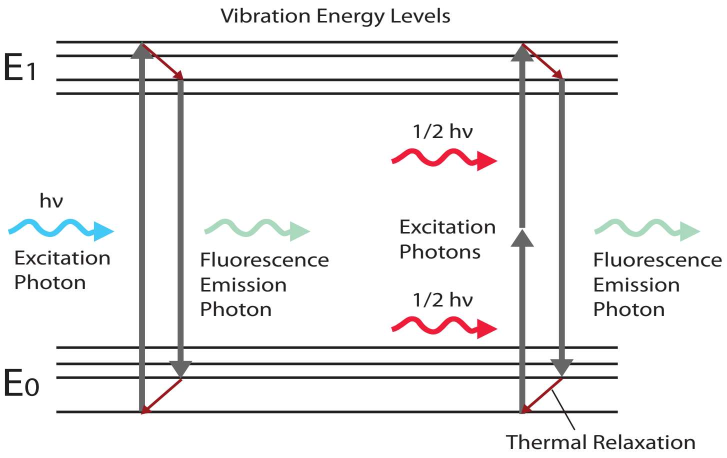

Figure 1.5: *Jablonski Diagram of the one- and 2-photon absorption process. By the absorption of a single photon or two photons of half the energy a fluorescent dye converts from its energy ground state* $\mathbf{E}_0$ *to a higher energy state* $\mathbf{E}_1$*.*

2-photon microscope instrumentation. Today complete multi-photon microscopes are commercially available from several companies, but alternatively the microscope can be custom built which is cheaper and opens the possibility to adapt and customize various parts of the microscope. However this requires a lot of technical knowledge about the microscope hardware, experience how to perform optical adjustments and some skills in software programming; hence several freeware versions of laser scanning software are available [Pologruto et al., 2003]; for rev. see [Helmchen and Denk, 2005]. The most important and probably the most expensive part of a multi-photon microscope is the pulsed laser source (Fig. 1.6). Widely used is a Titanium-Sapphire laser oscillator (Ti:Sa) that provides pulse repetition rates of about 80-100 MHz which typically match fluorescence lifetimes and thus balance excitation efficiency and onset of saturation. In addition Ti:Sa laser sources can be tuned over a large spectral range, typically 680-980 nm. Key features of such laser systems are the maximally available laser power and the output pulse length that directly depends on the size of the resonator within the laser. The maximally available output power of commercially available Ti:Sa laser systems currently ranges between 2-4 Watt with respect to the central part of the wavelength tuning range. Even with substantial losses in the optical pathway this output power is sufficient for most 2-photon applications. Depending on the optical components within the microscope the laser pulse length can be substantially broadened. Because the amount of laser pulse broadening increases proportional to the inverse laser pulse length, the intrinsic optimal pulse length can not be strictly defined; it could happen for example that a relatively short laser pulse ends up as a longer pulse than the initially longer pulse would end up. The temporal dispersion effects that cause pulse broadening can be nearly completely compensated by using gratings, prisms [Treacy, 1969, Diels et al., 1985] or a special combination of a prism and

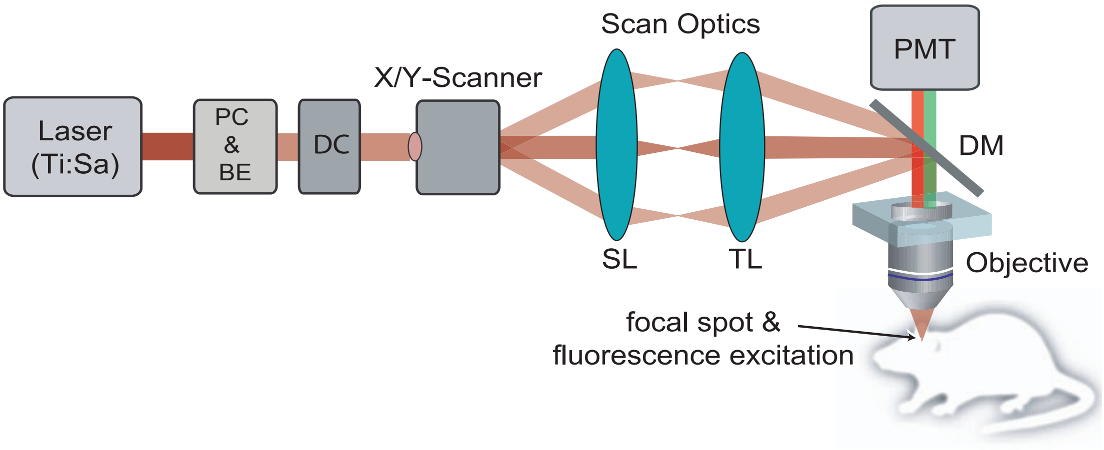

Figure 1.6: *Generic setup of a 2-Photon Laser Scanning Microscope.*
Basic components of a 2-photon microscope are (from left to right):
1. *a pulsed high-power near infrared (NIR) laser source*
2. *the beam expander (BE) to expand the laser beam and a Pockles Cell (PC) to modulate the intensity of the laser beam*
3. *a dispersion compensation (DC) to compensate for temporal and spatial dispersive effects, caused by lenses, objectives or scanners.*
4. *a laser scanning device such as movable mirrors or AOD s*
5. *scan optics; scan lens (SL), tube lens (TL) and the microscope objective*
6. *dichroic mirror (DM) and a photon detector, typically a photomultiplier (PMT).*

AOD-scanners [Grewe et al., 2010]. Such arrangements allow reshaping the original pulse length which increases the 2-photon absorption probability and thus the levels of fluorescence excitation.

Most commercially available laser scanning microscopes are speed limited during frame scanning , where the whole scanning field is scanned line by line. Frame-scanning is relatively slow (typically frame rates around 1-30 Hz) and wasteful because the major fraction of time is used to scan background areas rather than to scan structures of interest such as neurons. A promising alternative scanning scheme which may offer improved acquisition speed, is random- access scanning where the laser focus rapidly jumps from one point of interest to the next one by using a fast scanning device such as an acousto-optic deflector. In addition 2PLSM may enable optical stimulation and control of neuronal activity with a high temporal precision by using emerging genetic tools to express light-sensitive ion-channels (e.g., channelrhodopsin [Rickgauer and Tank, 2009] or caged glutamate [Kantevari et al., 2010]) in neurons.

1.4.2 Deep tissue imaging of neuronal population activity

Being a nonlinear microscopy technique, 2-photon imaging employs ultra short laser pulses with an emission spectrum around the near infrared region (NIR) to excite fluorescent probes. Using light of longer wavelength basically has two main advantages: 1. Because multiple excitation photons combine their energies during fluorescence excitation, the emitted photons have higher energies compared to the excitation light and thus shift the emission to shorter wavelengths within the visible spectrum which is different from traditional fluorescence imaging such as confocal microscopy. For commonly used fluorescent dyes this allows a sufficient excitation with light in the NIR wavelength range (720-920 nm) whereas the emission light can be well separated and detected within the visible spectral range. Furthermore near-infrared light penetrates deeper into light scattering tissue while effects of photo-toxicity are minimized due to the lack of endogenous one-photon absorbers in most biological tissues within this spectral range [Squirrell et al., 1999]. 2. Another major advantage of 2-photon imaging is that the fluorescence signal intensity (FSI) depends supra-linearily on the density of photons (I) with $FSI \propto I^n_{Photon}$. Here n is determined by the excitation process (2-,3-,... photon excitation) while for the 2-photon absorption process $n = 2$. As a result multi-photon fluorescence excitation is mainly restricted to a small region around the focal spot. The lack of excitation in out-of-focus areas thus further reduces effects of photo-damage and increases tissue viability which is crucial during long-term imaging experiments [Squirrell et al., 1999]. The most important feature when using 2-photon imaging is that NIR-light is less sensitive to light scattering in biological tissue, which allows to excite fluorescent dyes down to depths of several hundreds microns. By the same reasons multi-photon imaging reduces effects of photo-bleaching which is extremely helpful when performing repeated long-term imaging studies of the same sample. In addition the localization of the excitation spot can provide excitation-based three-dimensional imaging to measure a fluorescence staining throughout a volume [Göbel et al., 2007].

1.4.3 Visualizing cellular activity using calcium indicators

Currently calcium imaging is the prevailing optical method for probing neuronal ensembles *in vivo* [Garaschuk et al., 2006a, Göbel and Helmchen, 2007a, Takahashi et al., 2007]; reviewed in [Grewe and Helmchen, 2009]. Fluorescent calcium indicators are able to report intracellular calcium concentration changes evoked by action potentials which indirectly allows to infer neuronal spiking (Fig. 1.7). Calcium sensitive dyes are advantageous over voltage-sensitive dyes due to their high dynamic range, good signal-to-noise ratio (SNR), versatile labeling options and low photo toxicity. A tight correlation between spiking activity and somatic calcium transients has been confirmed by many studies, and single action potentials are detectable under favorable conditions [Kerr et al., 2005, Kerr et al., 2007, Greenberg et al., 2008, Sato et al., 2007]. During trains of action potentials individual calcium signals summate which then reflects changes in spike frequency [Ohki et al., 2005, Yaksi and Friedrich, 2006]. More recently new *in vivo* labeling techniques have triggered numerous calcium imaging studies, mostly employing 2-photon microscopy due to its superior depth penetration [Helmchen and Denk, 2005]. A highly successful approach during the last recent years has been bolus loading of cell populations in specific brain areas with traditional synthetic indicators, e.g. Oregon Green BAPTA-1 (OGB-1), Fluo-4 or Rhod-2 [Stosiek et al., 2003, Garaschuk et al., 2006b]. Although light scattering and movement problems have so far prevented the direct detection of synaptic input patterns *in vivo* - with rare exceptions; see ref. [Bollmann and Engert, 2009, Jia et al., 2010] - membrane permeable acetoxymethyl ester (AM) type calcium dyes have been used very successfully applied to monitor network activity in neuronal and glia cells *in vivo*, both under anesthetized and awake conditions [Ohki et al., 2005, Stosiek et al., 2003, Greenberg et al., 2008, Dombeck et al., 2007]. Recent work includes studies on the zebrafish olfactory system [Yaksi et al., 2007, Tabor et al., 2008, Yaksi et al., 2009], on the optic tectum in zebrafish larvae [Sumbre et al., 2008, Ramdya and Engert, 2008], on visual cortex of cats [Kara and Boyd, 2009], ferrets [Li et al., 2008] and rodents [Greenberg et al., 2008, Mrsic-Flogel et al., 2007, Rochefort et al., 2009] as well as on rodents somatosensory cortex [Kerr et al., 2007, Sato et al., 2007, Winship and Murphy, 2008], motor cortex [Dombeck et al., 2007] and cerebellum [Göbel and Helmchen, 2007b, Ozden et al., 2008, Engelbrecht et al., 2008, Flusberg et al., 2008].

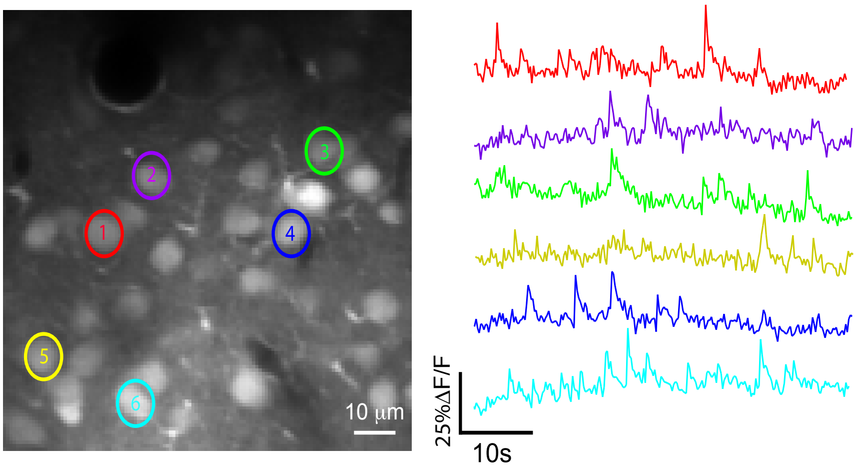

Figure 1.7: *Neuronal fluorescence signals, measured with 2PLSM.* **left***: Image of a neuronal cell population in mouse barrel cortex, labeled with the calcium sensitive dye OGB-Bapta 1. Image was acquired with a standard 2-photon microscope (4 Hz frame-scanning).* **right***: Relative calcium fluorescence signals (ΔF/F) were measured at the somata of six neurons that were marked in the left image.*

Intra-cellular calcium dynamics. Calcium is a major signaling ion in neurons, modulates synaptic input and can induce membrane voltage fluctuations that often trigger changes in the intracellular calcium concentration itself. Because the intracellular calcium concentration is about 10,000 times lower compared to the extracellular space, intracellular calcium indicators have been successfully used to infer supra-threshold activity in neurons [Berger et al., 2007]. A major breakthrough came with organic calcium-sensitive dyes which take advantage of the pronounced calcium concentration gradient across the plasma membrane. Under best conditions these dyes allow to detect the calcium influx well, mediated by a single channel within a spine head using 2-photon microscopy [Sabatini and Svoboda, 2000]. Thus they are often used to monitor the occurrence of both action potentials and synaptic input to spines.

But even with these outstanding indicators the fast onset time course of the intracellular calcium signal which is triggered by an action potential still has to meet the speed limitations of *in vivo* imaging. The fast time course (typically some milliseconds) thus makes it challenging to reliably detect single action potentials and to accurately reconstruct the underlying spiking pattern [Greenberg et al., 2008, Vogelstein et al., 2009]. While the major changes of the electrical membrane potential are caused by sodium and potassium channel activation the maximum calcium influx happens during the re-polarization phase of the action potential [Llinas and Jahnsen, 1982, Borst and Helmchen, 1998]. An example of a typical somatic calcium transient, shown in Figure 1.8 (adapted from [Grewe et al., 2010]), illustrates a typical somatic Ca^{2+}-fluorescence transient from a neuron somata that was filled with the intracellular calcium dye OGB-1 while measuring the electrical membrane potential.

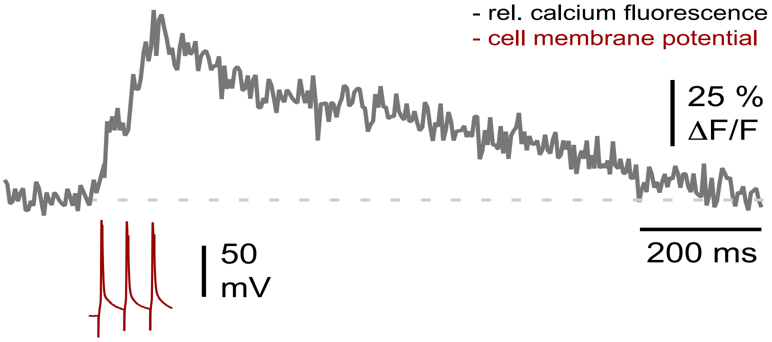

Figure 1.8: *Example of a somatic calcium fluorescence transient that was evoked by three subsequent APs. Before recording, the neuron was filled with the calcium sensitive dye (OGB-1, 200µm) via a patch pipette. AP's have been initiated electrically by injecting short current pulses at the soma. Fluorescence was acquired by using a standard 2-photon microscope that enabled to scan a single line over the soma. Sampling rate 512 Hz. All traces were recorded in vitro (acute slice preparation, P14, rat). Adapted from [Grewe* et al., *2010]*

While this example nicely demonstrates fast calcium fluorescence measurements of a single neuron, the aim would be to translate this measurement scheme to the *in vivo* situation and measure the activity of an extended neuronal population while maintaining a high temporal resolution.

Using population calcium imaging to investigate network dynamics Figure 1.9 illustrates an example of how population calcium imaging is utilized to reveal sensory coding by neuronal ensembles. The example shows visually-evoked neuronal calcium transients in the binocular region of cat visual cortex [Kara and Boyd, 2009]. In this case individual neuronal responses showed variable tuning across the population with respect to both ocular dominance (OD) and binocular disparity (BD). In addition the spatial maps for OD and BD tuning were found to have orthogonal orientation (Fig. 1.9). Similar neuronal 'tuning maps' could be revealed for the auditory cortex of mice where the activity of specific neurons was correlated to the frequency of single- and multi- tone stimulation [Rothschild et al., 2010] or for the olfactory bulb of zebra fishes where small populations of cells were found to respond to the prevalence of a certain odor component within an odor-mixture.

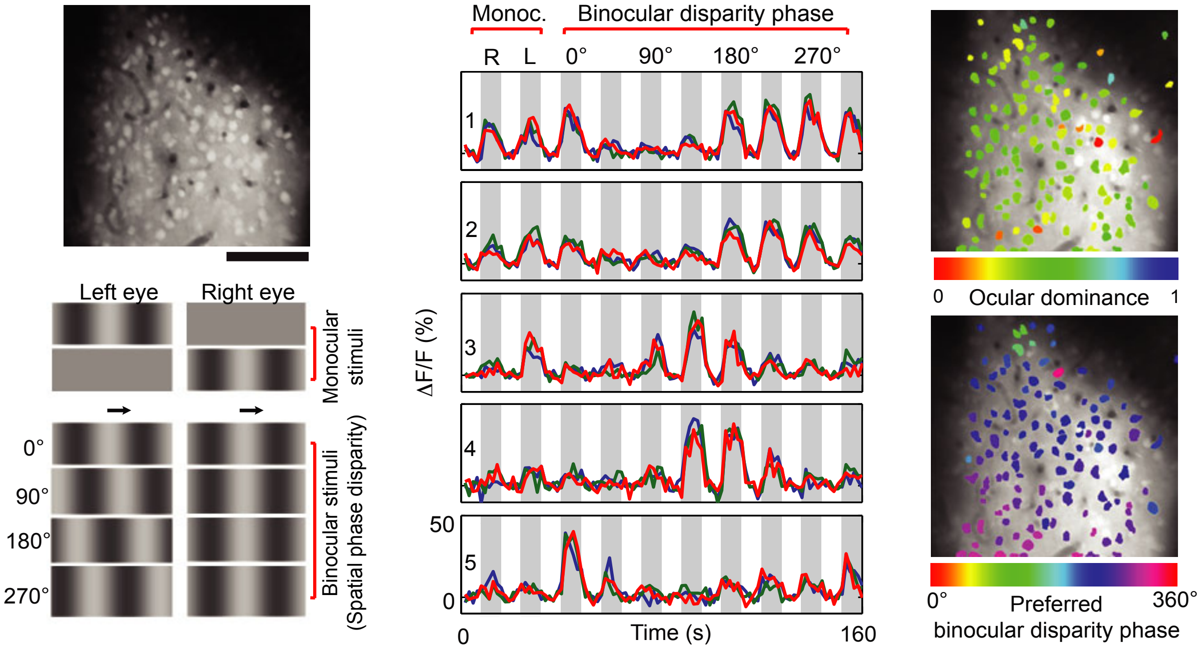

Figure 1.9: *Example of in vivo 2-photon calcium imaging of neuronal ensembles from cat visual cortex [Kara and Boyd, 2009]. A cell population in cat visual cortex about 200µm below the pia labeled with the calcium indicator OGB-1 (upper left, scale bar 100 µm). Calcium transients in response to monocular and binocular stimuli (lower left) are shown for five cells in the middle column (three trials superimposed). Colored maps of preferred ocular dominance and binocular disparity phases are shown on the right hand.*

1.5 Speed optimized state-of-the-art high-resolution imaging techniques

In spite of the success of *in vivo* calcium imaging for the visualization of neuronal ensemble activity, a number of challenges to sufficiently record neuronal ensemble activity still remain (for rev. see [Grewe and Helmchen, 2009]). One critical issue is the limited temporal resolution. A first strategy to improve imaging speed is to simultaneously excite fluorescence at multiple spots. For example wide-field illumination, spinning-disk confocal microscopy or light-sheet illumination techniques [Holekamp et al., 2008] together with readout by fast cameras or photodiode arrays nowadays support frame rates of several hundred Hertz (for review see [Takahashi et al., 2007]). Multi-spot excitation has also been implemented in laser-scanning systems either by splitting the laser beam in multiple beamlets creating an array of laser foci [Kurtz et al., 2006, Niesner et al., 2007] or by creating arbitrary excitation patterns in a 'scanless' approach using a diffractive spatial light modulator [Nikolenko et al., 2008]. Disadvantages of multi-spot excitation are the reduced laser power available per spot and strong sensitivity to light scattering which leads to cross talk between imaged pixels and reduced image resolution. Consequently depth penetration is limited ($d < 150\mu m$) and applications so far have been mainly restricted to extracted tissues and slice preparations (exception see [Kurtz et al., 2006]).

Mostly used for deep tissue imaging in the intact brain are conventional 2-photon laser scanning systems that use galvanometer-driven mirrors to deflect a laser beam across the field of view. This method of laser scanning is inherently limited by inertia of the scanning mirrors. In order to achieve the speeds necessary for monitoring fast physiological signals such as neuronal ion or Ca^{2+}- transients users typically reduce their region of interest to a small, low resolution scanning area [Kerr et al., 2005] or to a single line [Smetters et al., 1999, Stosiek et al., 2003, Zipfel et al., 2003]. Improving imaging speed with single-focus laser-scanning techniques is more difficult because a tradeoff between speed and the spatial extent of imaging is necessary (the latter determining the maximum number of simultaneously sampled areas). While line scans enable recordings of a few neurons at kilo-Hertz rate this rate reduces to a few Hertz or less when 2D movies of larger groups of cells are taken. In this case a useful strategy to increase acquisition speed is to restrict fluorescence excitation to the structures of interest and minimize background scanning. For this purpose laser scanning with galvanometric mirrors has been adapted to scan arbitrary free line scans on pre-selected subpopulations of cells [Göbel and Helmchen, 2007b, Nikolenko et al., 2007, Lillis et al., 2008]. In the extreme case galvanometers can be driven hard near their maximum acceleration to rapidly move the laser focus from one area to another remote area where it is slowed down again to scan only a few cells [Lillis et al., 2008] (Figure 1.10 a). This approach has been used in vitro so far and should be easily adaptable for *in vivo* measurements.

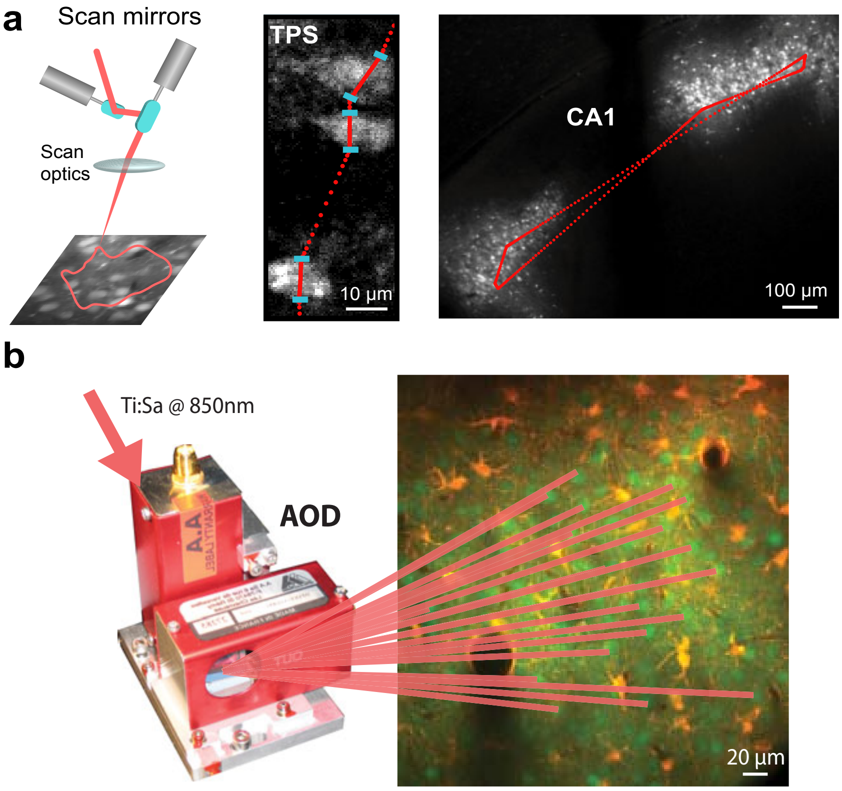

Figure 1.10: *Fast scanning techniques for neuronal population imaging. (**a**) Imaging of extended neural networks in acute hippocampal brain slices using targeted path scanning (TPS) [Lillis* et al.*, 2008]. Cell populations were bulk-loaded with Calcium Green-1 and scanned with standard galvanometric scan mirrors (left). The scan path was predefined by selection of pairs of points outlining segments of interest (blue markers). Each segment was sampled at a constant velocity, while the intervals between segments were traversed using maximal acceleration and deceleration (middle). Scan rates of about 100 Hz could be achieved in the CA1 region over extended fields of up to 1.1 mm (20x objective). (**b**) For this PhD-project a custom selected acousto-optic deflector performs high-speed laser scanning of neuronal cell populations, that were previously stained with the calcium sensitive fluorescence dye. left: High-resolution AOD-scanner that enables point-to-point transition times of* 10 15 *s. right: in vivo image of a cell population that was previously stained with the calcium sensitive dye OGB-1 (neurons) and the calcium in-sensitive marker SR101 (astrocytes).*

Alternatively improving the scanning speed can be addressed adequately by the use of an acousto-optic deflector (AOD) as a laser scanner [Goldstein et al., 1990, Bullen et al., 1997]. The AOD-scanner is inertia free as it deflects the laser beam by changing the applied acoustic-wave-frequency. Because the deflection angle which is determined by the acoustic frequency can be changed rapidly within some microseconds AOD-scanners provide a fast scan rate and high scanning stabilities over mechanical scanning devices. Furthermore AODs allow full and deliberate restriction of scanning to the structures of interest [Saggau, 2006]. Employing acoustic waves in two crossed AOD crystals a laser beam can be deflected with controllable angles in 2D. Due to the rapid AOD transition time between focus positions (typically a few microseconds) more than 80,000 points can be addressed per second enabling kilo-Hertz scan rates for arbitrary sets of pre-selected positions [Otsu et al., 2008]. Drawbacks of AODs are their dispersive effects (spatial and temporal) that need to be compensated especially when using femtosecond laser pulses and their relatively low diffraction efficiency. Nevertheless, optimizing dispersion compensation and laser beam transmission should make AOD imaging suitable for *in vivo* application. So far AOD scanning has been only been applied in vitro to measure action-potential evoked calcium transients at multiple dendritic sites in individual cells [Otsu et al., 2008, Reddy et al., 2008, Iyer et al., 2006] and in groups of neuronal dendrites [Otsu et al., 2008]. Because *in vivo* 2-photon imaging with AOD's necessitates the compensation of both spatial and temporal dispersive effects, AOD imaging at higher speeds has not been demonstrated in the intact brain. Challenging this, the development of a novel 2-photon microscope that is suitable for *in vivo* imaging and that employs fast acousto-optic deflectors has been the major topic of this project.

The random-access pattern scanning (RAPS) strategy. In most commercially available laser scanning microscopes 'frame scanning' or so called 'raster scanning', where the whole field of view is scanned line by line is state of the art. Scanning one line typically takes about 1-2 ms resulting in an average image acquisition time of 512-1024 ms per frame(512x512 pixel). Such frame scanning always wastes a large fraction of scanning time on the background rather than scanning structures of interest. The only way to improve the acquisition speed is acousto-optic 'random-access scanning', where the laser focus rapidly 'jumps' from one point of interest to the next one. The feasibility of AOD mediated 'random-access scanning' has been already demonstrated for 2D imaging [Bullen et al., 1997, Iyer et al., 2006, Salome et al., 2005]. Here, we aimed to develop a 2-photon laser scanning microscope that employs acousto-optic x/y-deflectors which allow scanning of about 83,000 points per second. The fundamental new idea of our method is to use discontinuous scan-pattern for fast data acquisition in preselected regions of interest.

1.6 Goals and strategy for this PhD-project

The main goal of this project was to develop a 2-Photon Laser Scanning Microscope that employs fast acousto-optic deflectors as x/y-scanners and to optimize all microscope components for imaging in the intact brain. The new scanning technique should enable 2D-frame scanning and allow high-speed optical measurements of pre-selected regions of interest. Therefore the aim was to choose the AOD-scanner properties to allow for optimization of the optical resolution, the laser beam transmission and the scanning speed. After the microscope hardware has been optimized and the random-access scanning modes had been implemented in the scanning software, this project further included a detailed evaluation of the microscope properties in terms of spatial and temporal resolution and laser beam transmission as well as the characterization of how fast and accurate neuronal signals can be measured by employing random-access 2-photon imaging in the intact brain of mice. Assuming a temporal scan resolution of about 10-15 μs the aim was to obtain functional activity patterns in extended neuronal populations, best with single-cell and single-spike resolution at very high sampling rates. The latter aim included the development of an automated data analysis algorithm that allows extract the neuronal activity that was covered in the fluorescence data traces. Then if recurring response patterns have been recorded the reconstruction accuracy of the spiking reconstruction algorithm can be investigated by performing dual recordings of neuronal activity (electrical and optical recordings). Once the spike detection sensitivity and accuracy has been evaluated the aim was to demonstrate an example of application for the novel technique. Thus we aimed to record sensory-evoked activity patterns in response to visual stimulation or whisker stimulation in layer 2/3 of visual cortex and barrel cortex of anesthetized mice.

The specific goals within this PhD-project are:

- The technological development of an AOD-based 2-photon laser scanning system, which includes the installation of the microscope hardware (x/y/z-motorized microscope stage, scan optics, etc.) as well as the development of electronic driver circuits for the AOD-scanners and the design and development of a scan control software in LabView.

- The design of a sufficient and effective dispersion compensation unit that allows to compensate for the spatial and temporal dispersive effects caused by the AODs.

- To obtain the first images of fluorescent beads and then optimize the microscope parameters (resolution, transmission efficiency, etc.) for high-speed measurements at multiple sites or regions. At the end this includes an evaluation of the optimized parameters.

- To perform first calcium imaging experiments *in vivo* and to further optimize the scanning procedure for the optimal signal-to-noise-ratio (SNR) while avoiding increased effects of photo-bleaching and photo-toxicity during cell scanning.

- To acquire data of network activity of a large set of neurons that respond to sensory stimulation at high sampling rates followed by a detailed analysis of scanning procedure properties as well as of the accuracy of neuronal spiking reconstructions.

- To demonstrate how the new scanning technique can facilitate to resolve typical stimulus evoked activity patterns of neuronal cell populations in the primary visual cortex and in the mouse barrel cortex.

- To explore the possibility for employing newly emerging genetically encoded dyes (used as reporters for intracellular calcium concentrations) for population imaging with the high-speed AOD-microscope system.

The research strategy for this project.

While the final goal of this project, the fast optical measurements of neuronal network activity in the intact brain was described previously, the research strategy to achieve this last goal is described in detail in this section (Fig. 1.11). During the starting phase the project involved the design and the assembly of the microscope hardware including the AOD-scanners and their driving electronics. The properties of the acousto-optic TeO_2-crystals had to be custom selected to allow a relatively short point-to-point transit time (t=10-15 μs). This would allow scanning of selected regions or cells with approximately 50,000-100,000 points per second while maintaining a large scanning field. However when using AODs to scan femtosecond laser pulses a mechanism that compensates for their dispersive effects needs to be considered.

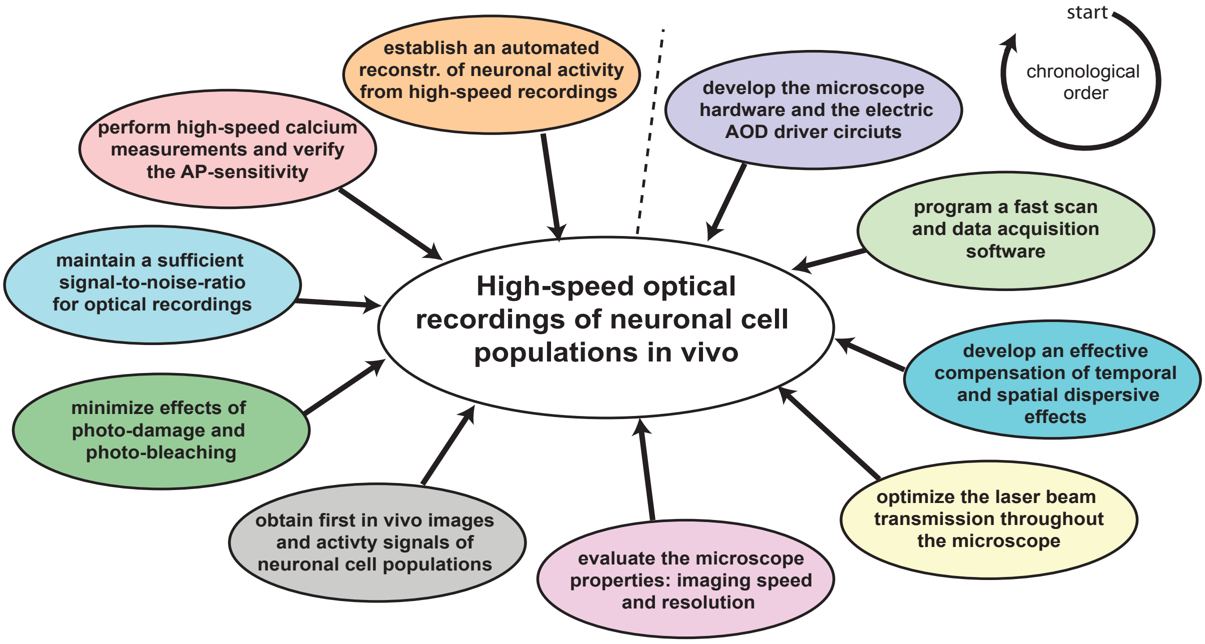

Figure 1.11: *The research strategy for this PhD-project.*

In parallel to the hardware development a software that controls the AOD-scanners while acquiring the fluorescence signals needed to be programmed. Then after several optimization procedures to improve important parameters of the microscope such as laser beam transmission and the microscope resolution all parameters have to be evaluated to verify the applicability of the novel microscope for deep tissue 2-photon imaging. The new fast random-access scanning method can then be combined with state of the art staining techniques for *in vivo* labeling of cell populations with commonly available fluorescent calcium indicator dyes. In addition counter-staining techniques can be used to distinguish cell types such as neurons or glial cells. The next step was to acquire the first *in vivo* images of neuronal cell populations and to measure their activity signals employing fast calcium imaging (for illustration see Fig. 1.10b). After further optimizations to improve the signal-to-noise ratio and to minimize photo-bleaching during random-access cell imaging the measurement sensitivity of the microscope system to obtain neuronal activity signals needs to be evaluated. The last step was to develop an automated data analysis algorithm that allows to extract the neuronal spiking activity from the recorded fluorescence traces.

2 Physical and Technical Background

2.1 The acousto-optic effect

Acousto-optic devices are based on the photoelastic effect according to which acoustic signal applied on an acousto-optic crystal produces a strain and thereby changes the optical properties of the crystal. The acoustic signal is injected into the crystal by means of a piezo-electric transducer, and while propagating it induces regions of compression and relaxation. If an optical beam passes through the crystal it may be deflected, modulated and additionally frequency shifted. The inhomogeneous changes of the optical properties caused by the propagating strain also induce changes in the refractive index of the material. A simple mathematical description of the photoelastic effect depends on the directional properties of the acousto-optic material and thus requires a tensor relation between the elastic strain and the photoelastic coefficients. Phenomenologically this effect can be described by the variations of the optical index coefficients B_i caused by the applied strain [Xu and Stroud, 1992, Goutzoulis and Pape, 1994]:

$$\Delta B_i = p_{i,j} * s_j \tag{2.1}$$

where $p_{i,j}$ is the photoelastic tensor with the components $i, j = 1, 2, ..., 6$. In case of an acousto-optic effect strain components s_j are produced by an acoustic wave that travels through a transparent medium. Stated in simple words: the acoustic wave is accompanied by a wave of refractive index variations.

2.2 Physical principles of acousto-optic devices (AODs)

In the basic operation mode of AODs a radio-frequency (RF) signal is applied to a piezo-electric transducer that was fused to a suitable acousto-optic crystal. This piezo-electric transducer generates a high-frequency acoustic wave which creates a 'phase-grating' while traveling through the crystal with the acoustic velocity of the optic material and the acoustic wavelength depending on the frequency of the RF signal. As a result any incident laser beam will be diffracted by this dynamic grating. By varying the AOD construction properties AODs can be operated in two different basic interaction modes, the 'Bragg'- and the

Raman/Nath -mode.

Conditions of light interaction. To determine the interaction regime the parameter Q is defined as the quality factor of the interaction regime that can be either Bragg - or Raman-Nath . The quality factor Q is given by:

$$Q = \frac{2 \quad \phi_0 L}{n \quad ^2} \tag{2.2}$$

where ϕ_0 is the wavelength of the incident laser beam, n is the refractive index of the crystal, L is the distance the laser beam travels throughout the acoustic wave (see Fig. 2.1), and is the acoustic wave length. The type of laser beam deflection now can be distinguished as follows:

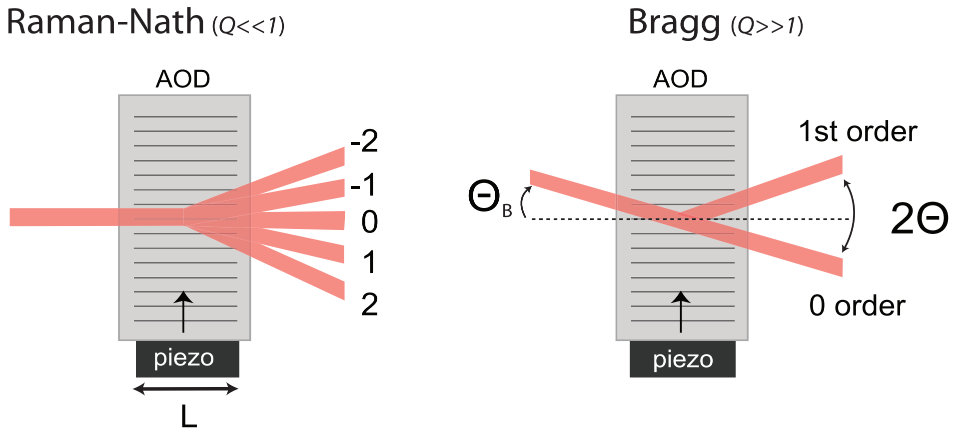

Figure 2.1: *Acousto-optic modes of operation depending on the quality-factor Q.* ***Raman-Nath regime****: The incident laser beam is normal to the acoustic wave vector. This mode results in several diffraction orders (...,-2, -1, 0, 1, 2, 3,...). The* ***Bragg regime****: at one particular incidence angle* $_B$ *only one diffraction order is produced while other diffraction orders annihilate by destructive interference.-*

Q 1: The Raman-Nath regime. The incident laser beam is approximately normal/orthogonal to the acoustic wave vector. Several diffraction orders appear (...,-2, -1, 0, 1, 2, ...) with intensities given by the Bessel-functions.
Q ≫ 1: The Bragg Regime. Using a certain, fixed incident angle only one diffraction order with up to 75% of the incident beam intensity is produced while the other orders mostly annihilate by destructive interference.

Because of higher diffraction efficiencies most acousto-optic devices (also that one used for this project) operate in the Bragg-regime. This enables laser beam diffraction efficiencies of about 75% per AOD. The typical setup of an AOD that operates in the Bragg-regime is shown in Figure 2.2. For this study an orthogonal pair of AODs was used for 2D-scanning.

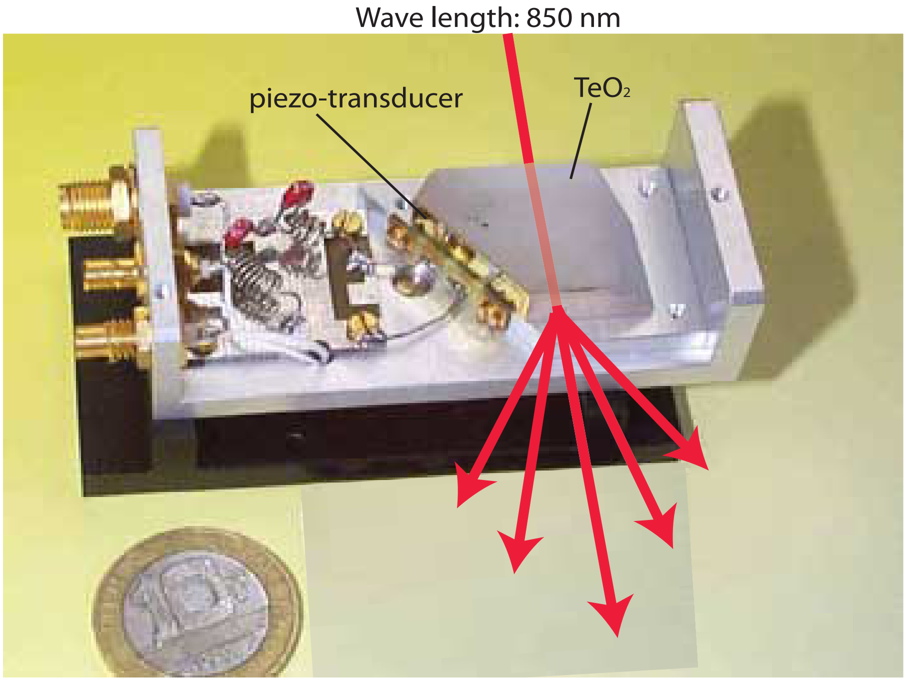

Figure 2.2: *Acousto-optic deflector for one dimensional scanning of the laser beam. Adapted from the AOD manufacturer homepage,* ***http://opto.braggcell.com*** *. (In this study an orthogonal coupled pair of AODs has been used to enable a two-dimensional scanning).*

Construction of the wave vectors. In the simplest case an acousto-optic interaction can be described by using the momentum vectors of the light and the acoustic waves. Because momentum conservation yields in the Bragg-regime we can derive the formula as follows (see also Fig. 2.3):

$$K_d = K_i \quad K_{acoustic} \tag{2.3}$$

The K-wave vectors can be calculated according to [Xu and Stroud, 1992]:

$K_i = \frac{2\ n_i}{_0}$ - wave vector of the incident beam
$K_d = \frac{2\ n_d}{_d}$ - wave vector of the diffracted beam
$K_{acoustic} = 2 \quad \frac{F_{acoustic}}{V_{acoustic}}$ - wave vector of the acoustic wave

here $F_{acoustic}$ is the sound frequency of the acoustic wave that travels through the crystal with the velocity $V_{acoustic}$. The refractive indices for the incident and diffracted beam are n_i and n_d, respectively. An additional consideration of the energy conservation leads to:

$$F_d = F_i \quad F_{acoustic} \tag{2.4}$$

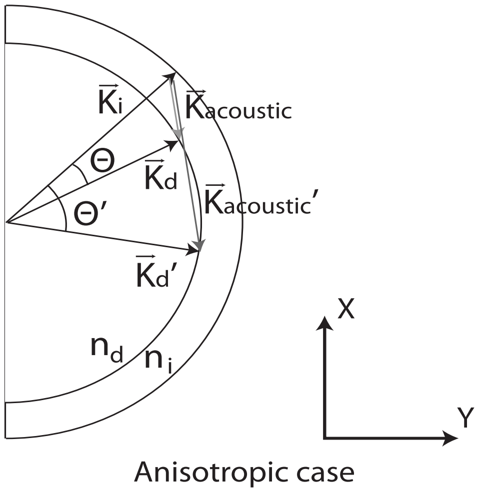

Figure 2.3: *Wave vector diagram for the general case of anisotropic diffraction of an incident light beam. The vectorial combination of the incident light wave vector (K_i) and the acoustic sound wave vector ($K_{acoustic}$) results in an deflection of the incident light (wave vector K_d) by the angle Θ. Because in most cases when light travels through a birefringent crystal the refractive index depends on the propagation direction of light with respect to the crystal lattice, the directional change of the incident light wave vector is accompanied by a change in the actual refractive index ($n_i \rightarrow n_d$).*

Equation 2.4 demonstrates that the optical frequency of the diffracted beam F_d differs by the frequency of the acoustic wave $F_{acoustic}$ compared to the frequency of the incident laser beam F_i. In general this 'Doppler-Shift' can be neglected, if $F_{acoustic} \ll F_d$ or F_i but can be of great interest for example in heterodynamic applications that employ further wave length separations.

Although a wide range of different materials and designs are used to build acousto-optic devices in general two modes of operation can be described which are the longitudinal or isotropic mode and the slow-shear mode or an-isotropic mode. While these operation modes share common principles of momentum and energy conservation (both in Bragg mode) they feature different properties in terms of diffraction efficiency and scanning-speed.

Isotropic interaction - The longitudinal mode. Isotropic interaction of light with acousto-optic material is also inferred as a longitudinal mode of interaction. In this case the acoustic wave travels longitudinally through the crystal while the incident and the diffracted laser beams face the same refractive index. The symmetry is conserved, the angle of incidence is found to match the angle of diffraction, and the polarization is not altered. While this mode would allow the fastest acousto-optic deflection of light with a sound velocity of about 4000 m/s and extremely short transition or scanning times the diffraction efficiency is generally low (10%-24%, see [Goutzoulis and Pape, 1994, Xu and Stroud, 1992]). This makes the application of the longitudinal mode difficult especially when higher diffraction efficiencies over a broader angular-scanning range are needed.

An-isotropic interaction - The slow shear mode. An an-isotropic acousto-optic interaction occurs only in optically an-isotropic crystals and involves separate diffraction between the ordinary and the extraordinary optical beams. Since these beams face different refractive indexes this acousto-optic interaction induces a rotation of the polarization of the diffracted laser beam by 90° with respect to the polarization of the incident laser beam. As illustrated in Figure 2.3 for a birefringent crystal the diffracted light wave vector K_d can differ in magnitude and direction from the incident light wave vector K_i. Therefore a direction change of the diffracted wave vector K_d to K'_d can be induced by changing the magnitude of the acoustic wave vector $K_{acoustic}$ to $K'_{acoustic}$. As a result the optical beam can be deflected at different angles simply by varying the frequency of a well collimated acoustic beam that propagates along a fixed direction through the crystal. This also implies that the angular spread of the acoustic wave vector requires much less phase matching across a particular acoustic bandwidth which results in a high diffraction efficiency within a broad angular range (typically 70-75% per AOD, [Goutzoulis and Pape, 1994, Xu and Stroud, 1992]). Because of these advantages slow-shear AODs are mostly used for large aperture devices that enable high-resolution scanning for a wide range of applications such as 2-photon imaging.

2.3 Dispersive effects of acousto-optic devices on femto-second laser pulses

Because AODs usually consist of two TeO_2 bi-refractive crystals, their dispersive nature causes spatial and temporal dispersion when using ultrashort NIR-laser pulses (Fig. 2.4) which results in pulse broadening and beam distortions and essentially reduces the fluorescence signal and the imaging resolution. During the past decade these effects have limited the application of 2D AOD-scanners for 2-photon imaging applications. While several studies demonstrate a separated compensation of the dispersive effects caused by the AODs [Lechleiter et al., 2002, Iyer et al., 2006], the optical microscope pathways were often complicated and yielded a very poor laser beam transmission, too low for *in vivo* applications.

As spatial and temporal dispersion caused by the acousto-optic grating are interconnected which opens the possibility to simultaneously compensate for both kinds of dispersion by one compensation mechanism [Zeng et al., 2006]. As shown in Fig. 2.5 an active AOD-scanner can be described by a grating that deflects the incident light according to its wavelength. The dynamic deflection angle θ is given by:

$$\theta = \frac{\lambda f}{V_{acoustic}} \tag{2.5}$$

where λ is the wavelength, f is the active frequency of the acoustic wave and $V_{acoustic}$ is the speed of the acoustic wave within the TeO_2-crystal. The time-bandwidth-product yields

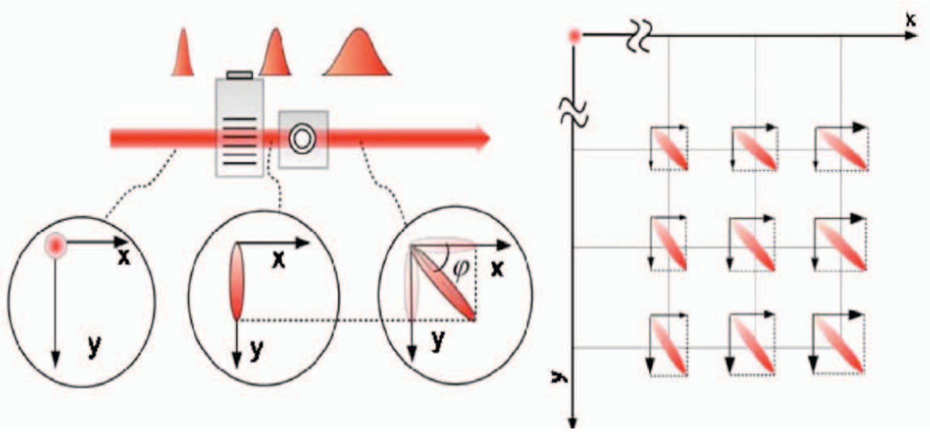

Figure 2.4: *Ultrashort laser pulses that are deflected by an AOD experience temporal (upper left) and spatial (lower left) dispersion which leads to laser pulse broadening and distortions of the laser beam profile respectively (right). Adapted from [Zeng* et al.*, 2007]*

that ultrashort laser pulses are not monochromatic which results in an altered deflection angle for different spectral components of the laser pulse. As a result the spectral components are spread along the direction in which the acoustic wave propagates which at the end forms an elliptically distorted focal spot. This effect is known as spatial dispersion τ_A and can be calculated for the active AOD by the derivation of equation 2.5 to ϕ:

$$\tau_A = \frac{d\sigma}{d\phi} = \frac{f}{V_{acoustic}} \tag{2.6}$$

For a single 1D AOD-scanner with a center frequency of 95 MHz and an acoustic sound velocity of 650 $m\ \ s$ the spatial dispersion constant τ can be calculated: $\tau_{A\ \ 1D} = 360\ \ 2 \ll (f\ \ V_{acoustic})\ 1000 = 0\ 0085\ \ \ nm$. The final integrated spatial dispersion of the combined 2D AOD-scanner can be calculated as a vector combination of the two separate dispersions of each deflector which after vectorial combination results in: $\tau_{A\ \ 2D} = \tau_{A\ \ 1D} \ll \overline{2} = 0\ 012\ \ \ nm$. Assuming a spectral pulse with of $\ \ 10nm$ (FWHM at 140 fs pulse length) the total dispersion angle would be 0 12 , which is about 4% of the total AOD-scan angle (47 $mrad$). Figure 2.4 shows an illustration of the shape of the focal spot due to the spatial dispersive effect. The orientation angle of each elliptical spot varies slightly across the scanning field due to the different x/y-frequency ratio of the different scan positions. The original round spot changes to an ellipse along the y-axis after passing the y-AOD deflector and twists by an angle of $\ \ = \arctan f_y\ \ f_x$, where f_x and f_y are the acoustic frequencies of each AOD respectively. Additionally to the spatial dispersive effects the length of the ultrashort NIR-laser pulses can be substantially extended because different spectral components travel with different speeds within the acousto-optic crystal. This effect is known as temporal dispersion (Fig. 2.4 (upper left))

Basic principles of spatial and temporal dispersion compensation. Classical pulse compressors employ two dispersive devices to form a pair configuration [Fork et al., 1984]. As a basic principle the first device introduces an angular dispersion and the second dispersive device re-collimates the light beam (Fig. 2.5). While the light beam with its angular dispersion propagates throughout these two dispersive elements its different wavelength components travel on different optical pathways (longer or shorter) which introduces a negative group-delay dispersion (GDD). Within the arrangement of the two dispersive elements, the induced negative GDD cancels out the positive GDD from any other components of the optical pathway and thus acts as pulse compressor. If the second dispersive element within the paired configuration is replaced with an AOD-scanner the principle of dispersion compensation still holds because the AOD can also act as a dispersive element. In this setup both spatial and temporal dispersion caused by the AODs can be compensated simultaneously while the original scanning function of the AOD is not disturbed. Figure 2.5 illustrates an optical arrangement where an acousto-optic modulator (AOM, fixed acoustic-frequency) or a prism is combined with an AOD to form a pair of dispersive elements that compensate for the dispersion caused by the AOD-scanner. Simply explained the AOD itself is in turn part of the dispersion compensation unit (DCU). In general any dispersive element that provides angular dispersion such as a prism, an AOM or a grating could be used in this arrangement. As shown in the next section a simple prism approach can be adapted and optimized to provide a sufficient compensation of spatial and temporal dispersion caused by a 2D AOD-scanner.

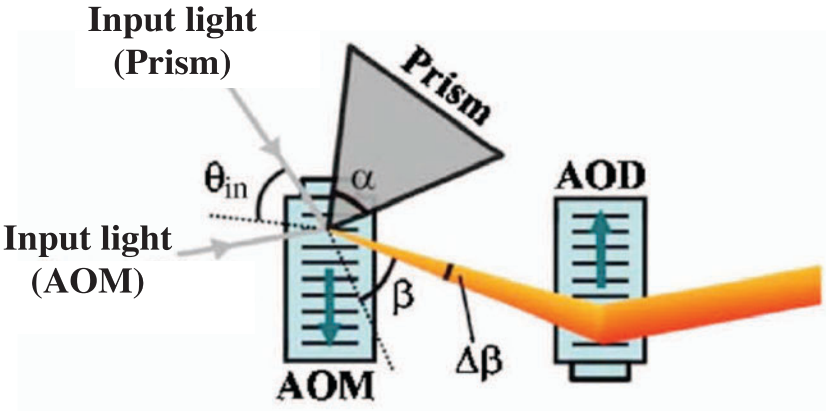

Figure 2.5: *Paired configuration to compensate for spatial and temporal dispersive effects simultaneously caused by the AOD; for simplicity only one AOD (used for only one-dimensional scanning) is shown schematically. The first element of this setup can be a grating, a prism or an AOM. In this scheme* $_{in}$ *and* π *are the light incident and output angles of the prism, is the prism apex angle and* π *is the angle of the induced spatial dispersion. Modified from [Zeng* et al.*, 2007].*

2.4 Dispersion compensation theory - the single prism approach.

Because the AOD-scanners in combination with femtosecond laser pulses induce spatial as well as temporal dispersion, dramatically reducing the microscope's resolution and its fluorescence excitation efficiency both, spatial and temporal dispersion need to be compensated. For our project we decided to compensate for both effects simultaneously by using a single prism approach.

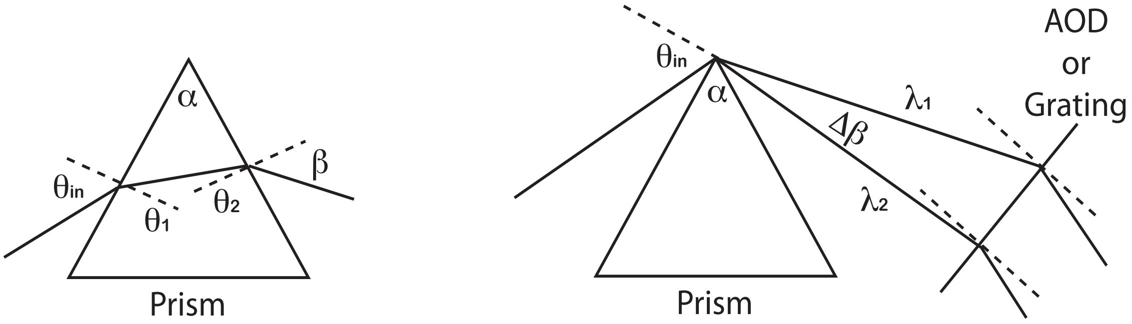

Figure 2.6: *Optical pathway of laser beam angle transformation in relation to the prism (left) and the prism-AOD configuration (right).*

Spatial dispersion compensation. Figure 2.6 shows the geometry of the compensation scheme with an isosceles-triangle prism. As shown in Figure 2.5 a non monochromatic laser beam has an incident angle θ_{in} to the prism and exits the prism at the angle β, although due to the material dispersion $dn/d\lambda$ the different spectral components exit the prism at different angles . The angle transformation relation by the prism is given by:

$$\sin\theta_{in} = n\sin\theta_1 \tag{2.7}$$

$$\sin\beta = n\sin\theta_2 \tag{2.8}$$

$$\theta_1 + \theta_2 = \alpha \tag{2.9}$$

where α is the apex angle of the prism and n is the refractive index of the prism. Differentiation of equations 2.7 and 2.9 with respect to n and substituting equation 2.7 and 2.9 into 2.8 results in the following equation (taken from [Zeng et al., 2007]) :

$$\frac{d\beta}{dn} = \frac{n\sin n}{(1 - n^2\sin^2\alpha - \sin^2\theta_{in}\cos 2\alpha + \sin 2\alpha\sin\theta_{in}(n^2 - \sin\theta_{in})^{1/2})^{1/2}(n^2 - \sin^2\theta_{in})^{1/2}} \tag{2.10}$$

The final spatial dispersion constant is given by the angular dispersion of the prism:

$$\sigma_p = \frac{d\beta}{d\lambda} = \frac{d\beta}{dn}\frac{dn}{d\lambda} \tag{2.11}$$

While $d\beta/dn$ is given in equation 2.10 now $dn/d\lambda$ needs to be solved. The term $dn/d\lambda$ can be calculated adequately by deriving the classic empirical 'Sellmeier Equation' (Equ. 2.12) with respect to λ and inserting the according material constants B_1, B_2, B_3 and C_1, C_2, C_3 (provided by www.Shott.com). The 'Sellmeier Equation' and its derivation is given by:

$$n = \sqrt{1 + \frac{B_1\lambda^2}{\lambda^2 - C_1} + \frac{B_2\lambda^2}{\lambda^2 - C_2} + \frac{B_3\lambda^2}{\lambda^2 - C_3}} \tag{2.12}$$

$$\begin{aligned} \frac{dn}{d\lambda} = 1/(2n) \Bigg(& \frac{2B_1\lambda(\lambda^2 - C1) - (B_1\lambda^2(2\lambda)}{(\lambda^2 - C_1)^2} \\ & + \frac{2B_2\lambda(\lambda^2 - C_2) - B_2\lambda^2(2\lambda)}{(\lambda^2 - C_2)^2} \\ & + \frac{2B_3\lambda(\lambda^2 - C_3) - B_3\lambda^2(2\lambda)}{(\lambda^2 - C_3)^2} \Bigg) \end{aligned} \tag{2.13}$$

If we combine the equations 2.10 and 2.13 to equation 2.11, the spatial dispersion constant σ_p is dependent on the angle of incidence θ_{in} and on the prism properties such as the apex angle α and the refractive index of the prism material (n) which both determine the prism dispersion characteristics (see also Fig. 2.7). For the design of the dispersion compensation with a single prism it would be ideal if the incident angle of laser beam and prism matches the Brewster angle of the prism. This would enable maximal laser beam transmission, and the beam path inside the prism would be symmetric and thus does not induce any distortions of the laser beam profile. In the following study we will test two prisms: one standard prism that is commercially available from Thorlabs (SF11 glass) and one that was custom designed (NSF66 high index glass) to match the needs and advantages as discussed above. However for both prisms the spatial dispersion constant inversely increases with the angle of incidence(Fig. 2.7, apex angles 60°, wavelength 850 nm). Figure 2.7 shows the dependency of the refractive index n to the wavelength, and how the spatial dispersion constant finally depends on the laser beam incident angle. To find the appropriate incident angle that matches the negative spatial dispersion caused by the two AODs, σ_P has to be adjusted so that $\sigma_P = \sigma_A = 0.012°/nm$. (see also grey circles in Fig. 2.7, right). The incident angles at $\sigma_P = \sigma_A = 0.012°/nm$ were found to be 53.4° (SF11) and 68.6° (NSF66).

Temporal dispersion compensation. The temporal dispersion constant of this configuration can be derived by calculating the optical path difference between the different spectral components of the laser pulse. Similar to [Nakazawa et al., 1988] the temporal dispersion constant can be calculated as:

$$\frac{\Delta\tau}{\Delta\lambda} = \frac{\lambda L}{c} \frac{d\beta}{dn} \frac{dn}{d\lambda} \frac{f}{V_{acoustic}} \tag{2.14}$$

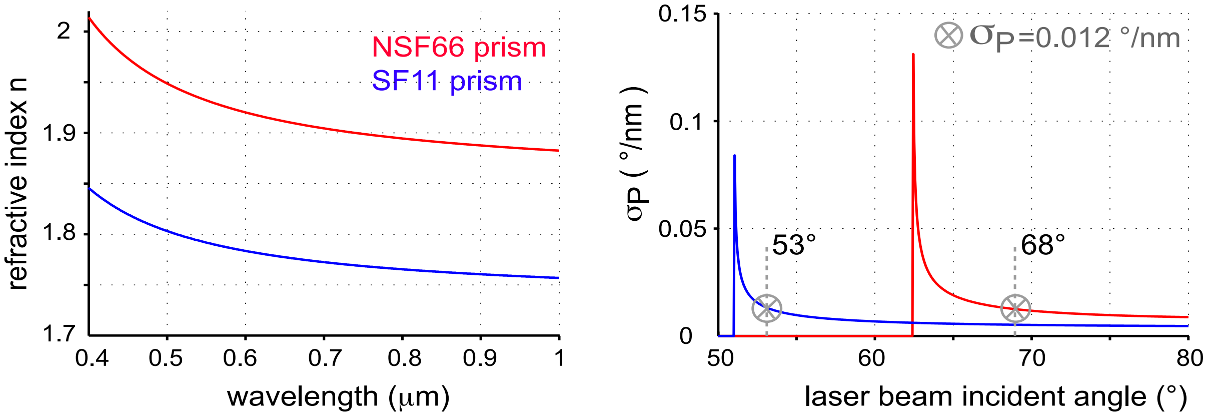

Figure 2.7: *The refractive index n of the prism material (SF11 blue and NSF66 red) is plotted over the wavelength (**left panel**). The relation of the prism dispersion constant σ_P to the according laser beam incident angle (**right panel**). For optimal light transmission this angle should be close to the Brewster-angle. The calculated Brewster angles were 60.4° for the SF11-glas and 62.1° for the NSF66-glas.*

where L is the distance between the prism and the AOD, c is the speed of light, f is the frequency of the acoustic wave, $V_{acoustic}$ is the velocity of the acoustic-wave in the crystal and $d\beta/dn$ is already expressed in equation 2.10. While the temporal dispersion constant is dependent on θ_{in}, the prism properties $(\alpha, n, dn/d\lambda)$ and the AOD properties $(f, V_{acoustic})$, it is also proportional to L. Similar to the spatial dispersion constant (σ_P, Fig. 2.7) the temporal dispersion constant increases inversely with the angle of incidence σ_P.
The corresponding group delay dispersion is given by:

$$GDD = \left(-\frac{\lambda^2}{2\pi c}\right)\frac{\Delta\tau}{\Delta\lambda} \tag{2.15}$$

The material dispersion $dn/d\lambda$ is negative for most of the prism material (such as for SF11- and NSF66-glass) for the NIR-range. The GDD provided by this configuration is negative and thus can compensate for the positive GDD that is caused by the AOD-crystals and the additional optical elements such as the scan- and tube- lenses or the microscope objective. In summary these analytical expressions explain the underlying principles of the simultaneous compensation of spatial and temporal dispersive effects.

Compensation differences for 1D and 2D AOD-scanning applications. When switching from one AOD to a pair of orthogonally arranged AODs the same compensation principles hold. The differences for the 2D AOD scanning compared to the 1D case are (1) the direction of the spatial dispersion of the 2D AOD is rotated by 45° with regard to the 1D AOD-scanner; (2) the amount of dispersion that needs to be compensated is larger according to the vector-addition of the individual amounts of each AOD-scanner. Balancing out these changes can be performed by rotating the dispersive element to adjust the altered orientation of the spatial dispersion caused by the 2D AODs. Additionally the angle of incidence has to be increased to compensate for the larger amount of spatial dispersion. After these alignments the distance between the dispersive element (prism) and the 2D AODs has to be increased until an optimal temporal dispersion compensation has been achieved.

2.5 Properties of acousto-optic deflectors

For most applications a high pointing precision in combination with a suitable diffraction efficiency is required when the laser beam is scanning over a probe. To match these needs usually large aperture TeO_2-AODs (10-30 mm aperture size, slow shear mode) are used to allow the deflection of large diameter laser beams which decreases the intrinsic optical divergence and thus increases the pointing precision or for imaging applications, the scan-resolution. The main performance parameters of an acousto-optic deflector are listed in table 2.1:

Characteristic	Parameter	Typical values
Center frequency	f_c	70-100 MHz
Acoustic frequency bandwidth	ΔF_Θ	30-40 MHz
Total AOD scan angle	Θ	30-50 mrd
Active AOD aperture	D	4-30 mm
Total diffraction efficiency	η_D	1-80 $\%W$
Access time	ΔT_{access}	6-50 μs
Time-bandwidth product	TB	900-2000 $MHz * s$
RF input power	P	1-3 W
Optical wavelength	λ	0.3-10.6 μm

Table 2.1: Typical parameters for acousto-optic deflectors (here TeO_2, slow shear mode) that have been used for microscopic applications.

Resolution properties for AOD-scanning. The static resolution of an AOD is defined as the maximum number of resolvable directions or scanning points of the diffracted or deflected laser beam over the total scanning angle.

For every collimated laser beam with the diameter d ($1/e^2$, TEM00-type beam) the natural beam divergence $\Delta\phi$ is equal to:

$$\Delta\phi = \frac{\lambda}{d} \tag{2.16}$$

Note: The maximum laser beam diameter is limited by the active AOD aperture (D_{max}). If the total scan angle of the deflector is defined as Θ, the total number of resolvable spots can be defined by:

$$N = \frac{\pi}{4}\frac{\Theta}{\Delta\phi} = \frac{\pi}{4}\frac{\Theta * D_{max}}{\lambda} \tag{2.17}$$

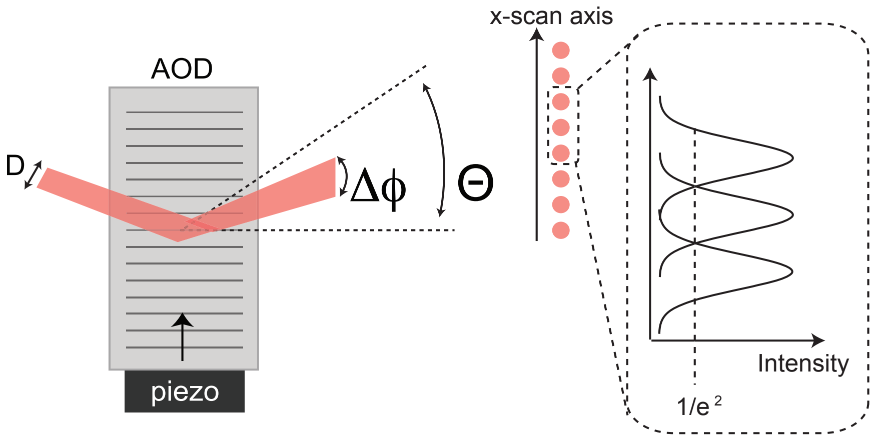

Figure 2.8: *Schematic illustration of the acousto-optic scanner and the resolution properties. In this scheme D is the laser beam diameter, is the total scan angle and is the divergence of the diffracted laser beam.*

While this equation holds for all types of scanners for acousto-optic deflectors the total scanning angle can be calculated according to equation 2.5:

$$= \phi \frac{F}{V_{acoustic}} \tag{2.18}$$

where ϕ is the optical wavelength of the incident laser beam, F is the acousto-optic bandwidth and $V_{acoustic}$ the acoustic velocity within the crystal. Combining the equations 2.17 and 2.18 results in:

$$N = \frac{}{4} \quad F \frac{D_{max}}{V_{acoustic}} = \frac{}{4} \quad F \ll T_{access} \tag{2.19}$$

In equation 2.19 the number of resolvable spots (N) is equal the acousto-optic bandwidth (F) multiplied with the access or transition time (T_{access}) of the AODs . This transition time corresponds to the time that the acoustic wave needs to travel through the active aperture of the AODs and thus is effectively needed to commutate the laser beam from one scanning position to another. Often an acousto-optic deflector thus is characterized by the time-bandwidth product (TB) that is given by $TB = \quad F \ll T_{access}$.

Diffraction efficiency of acousto-optic deflectors. The total diffraction efficiency of an acousto-optic deflector (ν_D) is usually expressed in units of %/W and is defined as the intensity ratio of the percentage of the incident optical beam which is diffracted $(I_d \; I_i)$ to the applied RF power P (in W). The total diffraction efficiency (ν_{Total}) can be described as:

$$\nu_{Total}(f \; T_{access}) = sin^2 \quad \overline{\nu_D(f \; T_{access})} \quad sin^2 \quad \overline{\nu_D} \tag{2.20}$$

The diffraction efficiency of an acousto-optic deflector ν_D is defined as the product of the strength of the acousto-optic an-isotropic interaction (ν_M) within the crystalline material and the degree (η_{match}) to which the acoustic wave vector is momentum matched to the incident optical wave vector $\eta_D = \eta_M * \eta_{match}$. As described by [Goutzoulis and Pape, 1994] the strength of an acousto-optic interaction can be found through a coupled mode analysis in which the interaction is described by an electric field wave equation where the index of refraction includes the acoustically induced perturbation. The strength for an an-isotropic acousto-optic interaction (η_M) is given by:

$$\eta_M = \frac{K_i^2 M * P * L}{8 \cos^2 \Theta H} \tag{2.21}$$

where K_i is the momentum of the incident optical wave, P is the acoustic power of the transducer, L is the path length of the optical beam in the acoustic field, H is the height of the acoustic sound field, Θ is the Bragg-incident angle of the laser beam at the center frequency and M is the AOD 'figure of merit' (a quality factor of the AOD-crystal). The matching of the acoustic wave vector and the optical wave vector η_{match} can be calculated as follows:

$$\eta_{match}(\gamma) = (\frac{\sin \pi\gamma L/\Lambda}{\pi\gamma L/\Lambda})^2 \tag{2.22}$$

where γ is the the angle between the acoustic wave vector and the light wave vector and Λ is the acoustic wave length. Multiplication of these equations allows to calculate the total diffraction efficiency:

$$\eta_{Total} = \sin^2 \sqrt{\eta_M * \eta_{match}} = \sin^2 \sqrt{\frac{K_i^2 M * P * L}{8 \cos^2 \Theta H} * (\frac{\sin \pi\gamma L/\Lambda}{\pi\gamma L/\Lambda})^2} \tag{2.23}$$

Computing this equation while varying the angle of deflection for one AOD leads to the typical AOD diffraction efficiency characteristic (Fig. 2.9). To evaluate the theoretical result from equation 2.23 the diffraction characteristic for the complete angular tuning range of the AOD was additionally measured (one AOD was swept through the frequency bandwidth while the other one was driven at the center-frequency (Fig. 2.9, right).

In summary we conclude that custom selected acousto-optic deflectors in combination with an effective dispersion compensation allow a sufficient laser beam transmission and scan resolution which makes AOD-scanners suitable for *in vivo* 2-photon imaging applications.

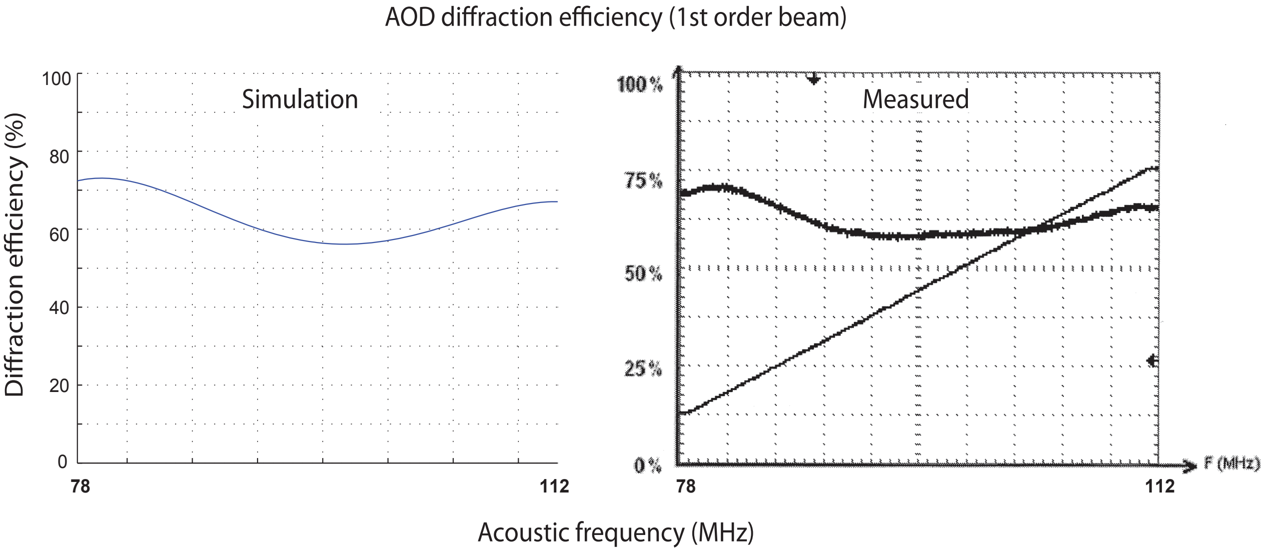

Figure 2.9: *Diffraction efficiency diagram (left: simulated; right: measured) shows* ν_{Total} *in % over the acousto-optic bandwidth of the 2D AODs that were mainly used for this study. While the acoustic frequency for one AOD (x) was set to the center frequency (95 MHz) the second AOD (y) was swept through from 78-112 MHz. The input power was optimized to the technical recommended maximum of 2.5 W.* ν_{Total}*-values were calculated by formula 2.23 that was integrated in a Matlab routine (AOD_Calc.m); for the detailed Matlab program code and the according parameters please refer to the appendix section.*

3 Development of a 2-Photon Laser Scanning Microscope with AODs

While standard 2-photon microscopes usually employ galvanometric mirrors, which allow frame-scanning at several Hertz, a promising alternative is to use fast acousto-optic deflectors for laser beam scanning. AOD-scanners enable transitions of the laser focus within several microseconds between any two positions in the scanning area. Such fast transitions avoid waste of scanning time on background regions and enable random-access scanning from preselected points of interest only (e.g. neurons). Disadvantages of AODs are their limited laser diffraction efficiency (about 55% transmission for a xy-pair of AODs) and the large optical dispersion of the acousto-optic crystal which causes laser pulse broadening and spatial deformation of the laser focus. Dispersive effects can either be minimized by using relatively long laser pulses (0.5-1.8 ps; [Iyer et al., 2006, Otsu et al., 2008, Reddy et al., 2008]) which however reduces 2-photon fluorescence excitation, or they need to be compensated with additional diffractive elements [Zeng et al., 2006, Kremer et al., 2008, Zeng et al., 2007] (see also previous section). In this chapter we provide detailed instructions and recommendations how to assemble an AOD-based laser scanning 2-photon microscope including all optimization procedures to render the microscope suitable for *in vivo* imaging applications (see also [Grewe et al., 2010]).

3.1 Instrumentation of the microscope

Our AOD-microscope was designed as a ”fixed-stage” microscope that can be moved over the sample. This design provides large space below the objective lens and also supports stable simultaneous electrophysiological recordings during *in vivo* imaging experiments using a table-mounted micro-manipulator. The complete microscope was built around a X-95 aluminum column mounted onto a motorized x/y-stage (Fig. 3.1a). As scanning device we chose two orthogonally mounted AODs that have been custom selected for an adequate scan-resolution over a large field of view (FOV) and optimal laser beam transmission (active AOD aperture - 10 mm, 47 $mrad$/2.9° total scan angle, 55% transmission at λ=850 nm). Several important issues need to be considered when assembling the microscope. First, the AOD specifications together with the choice of objective and the scan- and tube-lens combination determine the image resolution and the field-of-view size. As the maximal

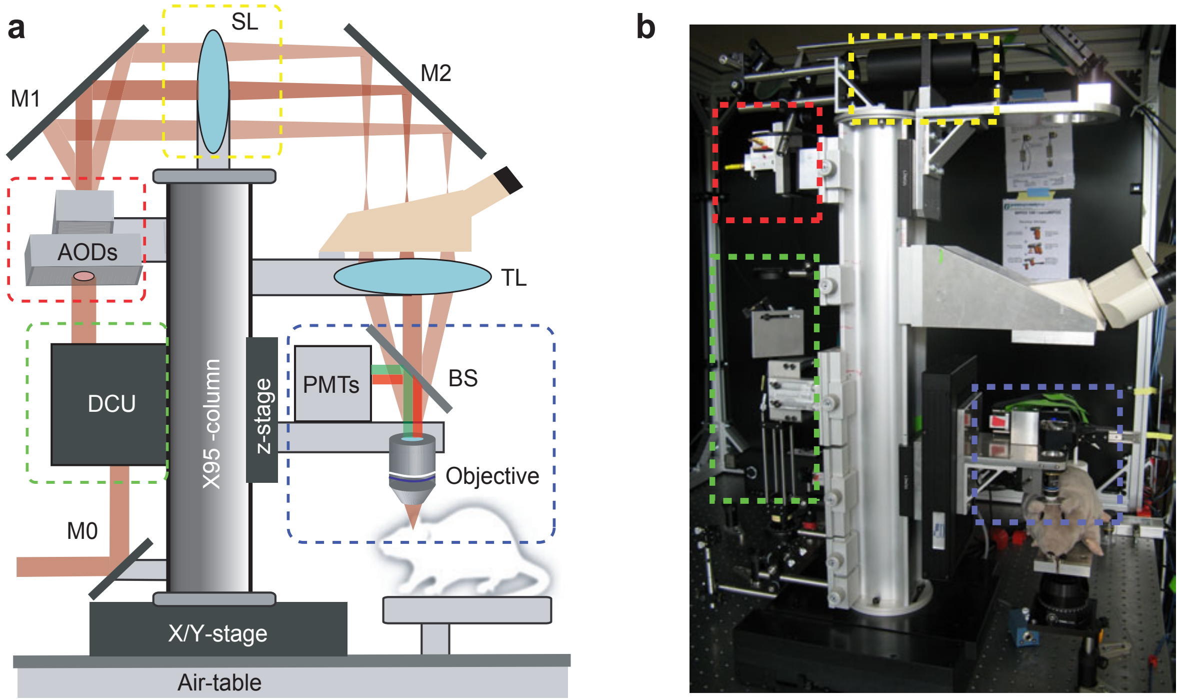

Figure 3.1: *AOD-based microscope setup for high-speed calcium imaging. (**a**) Schematic drawing of the 2-photon microscope setup mounted on an air-table. A motorized x/y-stage supports movements of the complete microscope over the sample. Above the dispersion compensation unit (DCU) two orthogonal AODs were used for x/y-scanning. Scan lens (SL) and tube lens (TL) were chosen to provide a large FOV with a 40x objective. M0, M1 and M2 are broadband NIR mirrors. BS is a dichroic mirror (**b**) Photography of the finalized 2-photon setup. Colored squares indicate the optical components of the microscope setup as follows: yellow, scan lens / red, AODs / green, DCU / blue, detection pathway and objective*

AOD scan angle is limited (47 $mrad$) the number of resolvable spots N is limited too depending on the laser beam size at the AOD aperture. For a Gaussian laser beam of full 1 e^2 width D and the wavelength ϕ the number of resolvable spots (N) is given by $N = 4 \ll \ll D \ \phi$ (see equ. 2.19 in the previous section, taken from [Kremer et al., 2008]). If the best possible resolution is the main interest, the laser beam should be expanded to fill the AOD-aperture (to maximize N) and the FOV size should be maximally $S \ll N$ where S is the diffraction-limited spatial resolution as determined by the effective numerical aperture (NA) of the microscope objective. With slightly underfilled AOD aperture (D = 7.9 mm) we calculate 342 resolvable spots for our system. For the best microscope resolution the number of resolvable spots would determine a maximum FOV size of 170 m x 170 m. In our setup however we were more interested in a large FOV to enable functional imaging of neuronal cel populations. Therefore we chose a larger FOV and accepted that the image resolution was limited by the AOD pointing precision to about 1 micron in the FOV center (theoretical focal spot size of about 0.9 micron, [Grewe et al., 2010]). To obtain a certain FOV size one has to choose the right combination of scan and tube lenses for a particular microscope objective. Based on our FOV size we chose the objective, and the scan lens (Note: The tube lens should be selected so that the objective's magnification is maintained, e.g. $f_{TL} = 180mm$ for Olympus or Nikon objectives). Since the combination of the scan and tube lens acts as a telescope and changes the laser beam diameter, the corresponding demagnification (or magnification) should match the factor required to image the laser beam at the AOD aperture into the objective's back aperture. In our system we obtained a maximum FOV of $305\,\mu m * 305\,\mu m$ with a 40x objective (scan- and tube-lens telescope demagnification of 0.6). The microscope objective and the fluorescence detection system were mounted on a motorized z-stage. Green and red fluorescence signals were detected in two emission channels using photomultipliers (PMTs) digitized at 20 MHz and digitally integrated using a Free Programmable Gate Array (FPGA) evaluation board. Scan signals for the AODs and data acquisition were controlled with software custom-written in the LabView 2009 environment (see below).

Materials

The list of major components and suppliers is as follows:

Laser & Accessories:

- Ti:sapphire laser system, e.g. Chameleon Ultra II, Coherent, Dieburg, Germany (>2.8 W average power at 850 nm wavelength)
- Laser intensity modulator, Pockels cell, Model 350-80, Conoptics, Danbury, USA
- Variable beam expander, S6ASS2075, Silloptics, Wendelstein, Germany
- Broadband mirrors, BB1-E03 & BB2-E03, Thorlabs, Newton, USA
- Mirror holders, KMS/M, Thorlabs, Newton, USA
- IR-viewer, IRV1-1700, Newport, Irvine, USA
- Power meter, PM100D & S350C, Thorlabs, Newton, USA

Microscope stand:

- Optical table, RS2000 (+ 4 Stabilizer, L2000), Newport, Irvine, USA
- X/Y-motorized stage, KT310, Feinmess, Dresden, Germany
- Main column & baseplates, X95-640 column & X95 base plate, Linos, Feldkirchen, Germany
- Column holders (6-8x) , X 95 clamping carrier, Linos, Feldkirchen, Germany
- Z-stage, PMT 160 DC, Feinmess, Dresden, Germany

- XYZ-stage controller, Galil Motion Control, Rocklin, USA

Scanning apparatus and dispersion compensation unit:

- Acousto-optic deflectors, DTSXY-A12-850, AAoptoelectronics, Orsay, France
- AOD-alignment platform, PY003, pitch and jaw platform, Thorlabs, Newton, USA
- Frequency generator (2x), AD9852, evaluation board, Analog Devices Inc., Norwood, USA
- Frequency amplifier (2x), AA.AMPA-B-36, AAoptoelectronics, Orsay, France
- Scan control board (FPGA), PXI-8713R, National Instruments, Austin, USA
- Compensation prism, SF11 prism, apex angle 60°, uncoated, Thorlabs; or custom shaped prism (NSF 66, apex angle 60°, uncoated)
- Prism rotation mount, PR01/M, micrometer rotation mount, Thorlabs, Newton, USA
- $\lambda/2$-waveplate (2x), RZ-1/2-850, Thorlabs/OFR, Newton, USA
- Waveplate rotation mount (2x), RSP1/M, rotation mount, Thorlabs, Newton, USA
- Cylindrical lens telescope, $f_1 = 100$ mm, $f_2 = 50$ mm, achromatic, N-BK7, Thorlabs (only necessary for SF11 Thorlabs-prism)
- Scan lens, $f_{SL} = 300$ mm, achromatic, NIR-coating, Thorlabs, Newton, USA
- Tube lens, $f_{TL} = 180$ mm, achromatic, Olympus, Center Valley, USA
- Control computer, e.g. dc7900, quad-core, Hewlett Packard, Palo Alto, USA
- Scan software, Custom written scan software in Lab View 2009, National Instruments, Austin, USA

Detection Pathway:

- Microscope objectives, 40x LUMPlanFl/IR, NA 0.8, Olympus, Center Valley, USA (we also use a 10x UPLFLN10X2, NA 0.3, Olympus for a large-field overview of the preparation)
- Photomultiplier tubes (PMTs), e.g. R6357, Hamamatsu, Hamamatsu City, Japan
- PMT preamplifier, XPG-ADC-PREAMP, Sigmann-Elektronik, Hüffenhardt, Germany
- A/D-converter (40 MHz), custom design by CSEM, Zurich, Switzerland
- DAQ Board (FPGA), same as above (PXI-8713R)
- 2-photon beam-splitter, Cold light mirror KS 93/45°, Linos, Feldkirchen, Germany

- Dichroic mirror, DC-green, Linos, Feldkirchen, Germany
- Emission filters, HQ 535/50 (green; Chroma Technology, Bellows Falls, USA), SP 720 (red; AHF, Tubingen, Germany)

3.2 The dispersion compensation unit (DCU).

Because the temporal and spatial dispersion that is caused by the AODs strongly decreases the microscope resolution and indirectly the fluorescence signal intensity, the second key optical part is the dispersion compensation unit (DCU) (Fig. 3.2).

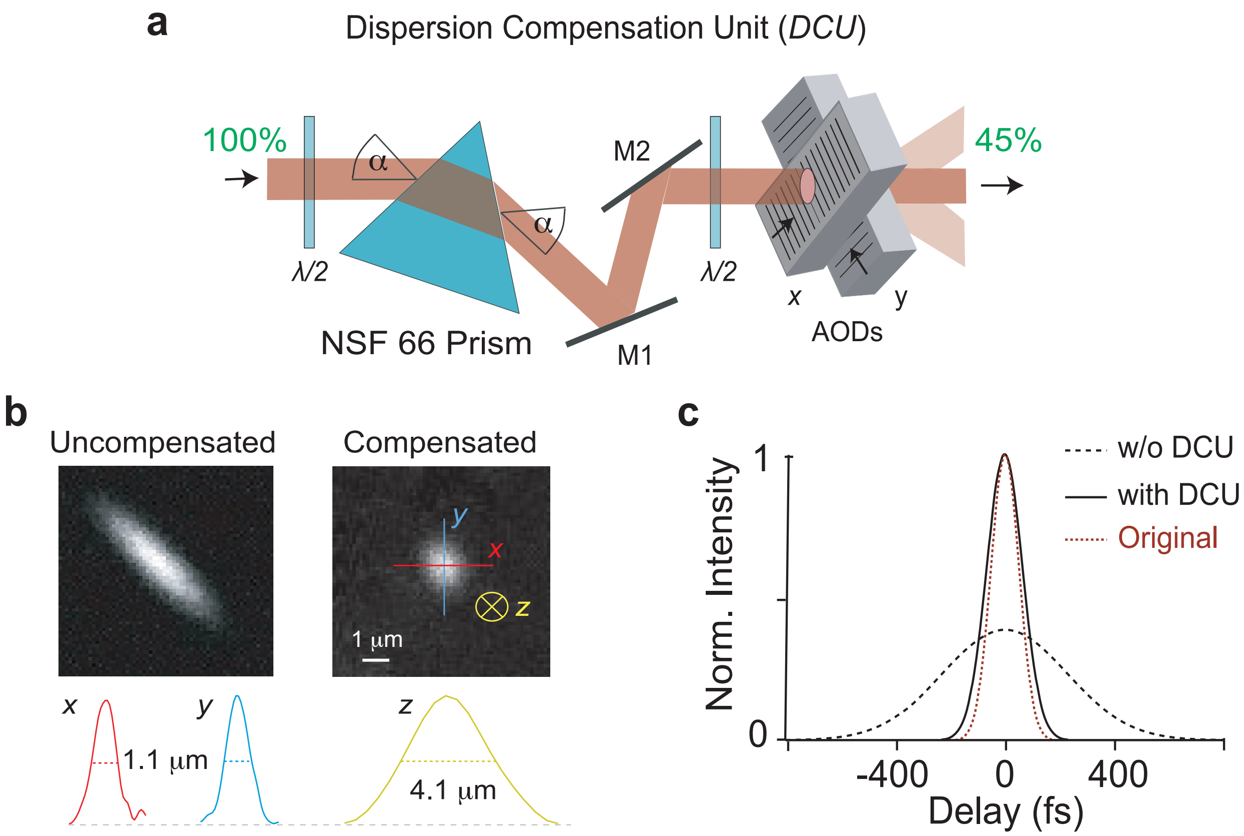

Figure 3.2: *Effects of spatial and temporal dispersion compensation. (**a**) Schematic drawing of the optical path through the single-prism DCU consisting of two $\phi/2$-waveplates and a custom prism oriented at a 45° angle to the AOD's axes. If a SF11 prism is used (see material list) an additional cylindrical telescope is necessary (not shown) to compensate for beam ellipticity caused by mismatch of the input and output angle at the prism. (**b**) 2-photon images of 500 nm fluorescent beads without (left) and with (right) the DCU. Intensity profiles along x-, y- and z-direction are shown on the bottom indicated by full width half maximum (FWHM) values. (**c**) Laser pulse width measured with and without the DCU. The original pulse width at the laser output (red) is shown for comparison.*

We modified a single-prism compensation approach [Zeng et al., 2006] and optimized it for laser beam transmission and scan resolution over a large FOV. Two $\lambda/2$-waveplates in front of the prism and the AODs respectively turned the laser beam polarization along the pathway and thereby maximized transmission through prism (85%) and the AOD pair (55%). In total 45% of the incoming light was transmitted by DCU and AOD-scanners (Fig. 3.2). With a standard SF11-glass prism the beam path is not symmetrical through the prism which makes the beam elliptical behind the prism. This effect can be corrected by using a cylindrical lens telescope (CLT) e.g. in front of the prism restoring a nearly round laser beam profile at the AOD aperture [Grewe et al., 2010]. In our latest setup we replaced the SF11-glass prism with a custom designed NSF66-glass prism for which the beam path is symmetric so that the cylindrical lens telescope can be omitted. For a detailed description of the prism design process and the underlying calculations please see the previous chapter and the appendix section at the end.

Proper alignment of a single prism (NSF66-glas, apex angle 60°, uncoated) in front of the first AODs allowed to compensate for spatial and temporal dispersive effects caused by the acousto-optic material [Zeng et al., 2006,Lechleiter et al., 2002]. By tuning the laser beam's incident angle on the prism to the theoretical value of 69° we could counterbalance the spatial dispersion effect nearly perfectly for the center of the FOV (Fig. 3.2). The appropriate distance of the prism in front of the AODs was about 35 cm which resulted in an optimal laser pulse length behind the AODs as determined with a FROG device (GRENOUILLE, Swamp Optics, Atlanta, USA). The beam profiler option of the FROG was also used for measurement of the beam diameter along the optical path.

3.3 The AOD driving electronics

In contrast to galvanometric scanning mirrors where a voltage signal directly determines the angular tuning and thus the scan position within the FOV the piezo-transducers of acousto-optic deflectors need to be driven by a high-frequency voltage - ranging from 77-114 MHz - that determines the angle of deflection. To generate these high-frequency or radio frequency (RF) signals we used Direct Digital Synthesis (DDS) which made it possible to generate any preset frequency between 10-300 MHz within some nano-seconds. For evaluation and testing purposes we employed two DDS-processors (AD9852, Analog Devices) that had been already integrated in prefixed evaluation boards. As the RF signal output of the DDS-processors is very weak their output was connected to an additional power amplifier (AA.AMPA-B-36, 4 Watt, AAoptolectronics, Orsay, France) which provided the required peak-to-peak amplitudes for driving the AODs efficiently.

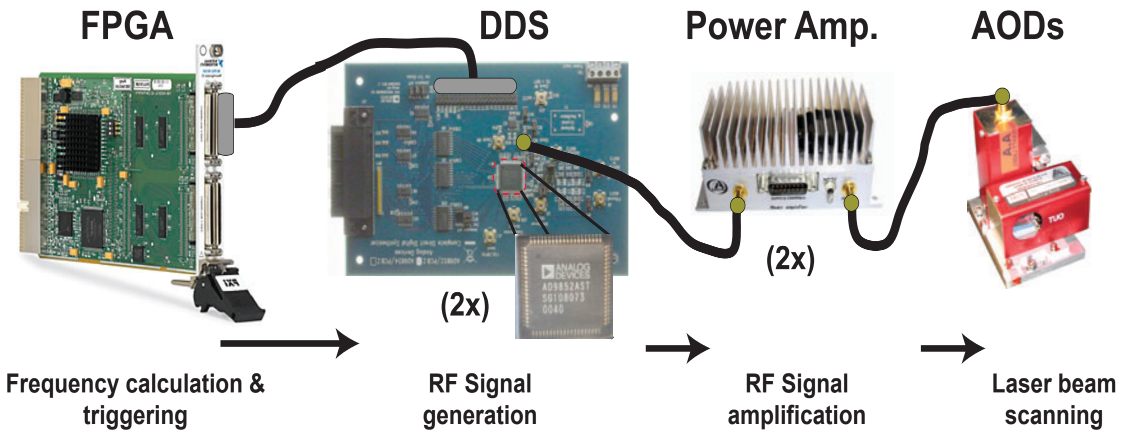

Figure 3.3: *AOD driver circuit. Electrical driver circuit which allows a fast generation of sinusoidal high-frequency voltage signals necessary to drive the AODs for efficient laser beam scanning.*

Fast scan pattern calculation on an FPGA. To calculate and trigger the according x/y-AOD-frequencies for each scanning point we used a fast Free Programmable Gate Array (FPGA) from National instruments (PXI-8713R) that allowed operation speeds of 20 MHz while executing the frequency calculation algorithm. Both scanning modes (frame-scanning and high-speed random-access scanning) were implemented on the FPGA board. Beside the data acquisition and integration of each single pixel the FPGA allowed to calculate the x/y-frequencies for the next pixel including rotation, zoom and amplitude corrections (Note: The amplitude of the RF signal directly modulates the AOD diffraction efficiency). When the x/y-frequency calculation was finished (typically 1-2 μs) the digital frequency values were transmitted to the DDS-processor while the final trigger to generate the new frequency for the next pixel was sent to the DDS at the end of each pixel integration.

3.4 Assembly of the microscope hardware

For setting up the optical light path of the microscope we recommend a backwards-construction approach as follows: (1) mount the microscope objective, (2) install tube lens and scan lens, (3) mount AOD-scanners and the dispersion compensation unit (DCU), and (4) proceed with the beam alignment. Customized mechanical parts were used to mount the various components such as the AODs, the scan- and tube-lenses and the detector pathway with the objective. We also mounted a binocular in our beam path for direct viewing of the FOV (Fig. 3.1a). A detailed protocol of the microscope construction includes the following steps:

1. First, we set up the laser, the shutter, the Pockels cell (PC), and the variable beam expander (BE).
2. Then the motorized x/y-stage was fixed on the air-table.
3. Next we mounted the X95-column with the two base plates attached onto the x/y-stage.
4. After that we mounted the linear z-stage PT160 on the X95-column by using a clamping carrier.
5. Then a custom objective holder was built and attached to the PT160 z-stage. We used a distance of about 20 cm between the optical axis and the X95-column.
6. Subsequently we designed and built the fluorescence detection pathway that includes a sliding 2-photon beam splitter, the dichroic mirrors, fluorescence filters, and PMTs. We used two channels but in principle even more channels can be added.
7. We next attached the fluorescence detection unit to the linear z-stage directly above the objective.
8. Next the tube lens was installed at the appropriate distance (focal length f_{TL}) above the objective.
9. We then mounted the scan lens at the correct distance ($f_{TL} + f_{SL}$) on top of the X95-column (we used a 45° BB2-mirror to redirect the laser beam).
10. We then mounted the AODs at the correct distance (focal length f_{SL}) on the opposite site of the column (we again used a 45° BB2-mirror to redirect the laser beam to the AOD-scanners).
11. We used a clamping carrier to mount a $\lambda/2$-waveplate (embedded in a rotation mount) in front of the AODs.
12. The prism rotation mount with the compensation prism was installed on a clamping carrier. We used a custom-built holder to install the compensation prism at an angle of 45° with respect to the AOD's axes.
13. We next attached mirror mounts for two mirrors behind the prism that redirect the laser beam to the AODs (Fig. 3.1b).
14. Then we installed a $\lambda/2$-waveplate (embedded in a rotation mount) on a clamping carrier in front of the compensation prism.
15. Last we mounted a 45° mirror at the X95-column base to reflect the laser beam into the microscope pathway. In addition we mounted two mirrors that are oriented 90° to each other onto the two linear moving parts of the x/y-motorized stage (x- or y-direction, respectively). These mirrors were used to steer the fixed input laser beam to the microscope pathway while avoiding laser beam run off during stage movements.

3.5 Alignment and optimization procedures

The microscope design is kept relatively simple with two key components that have to be properly aligned (the AOD-scanners and the DCU-prism). Given about 45% transmission through these two components the total transmission efficiency of the entire microscope should not go below 25% (850 *nm* wavelength, 40x objective). The temporal pulse broadening can be almost completely compensated by adjusting the distance between the DCU prism and the AODs, so that minimal pulse lengths are achieved behind the objective (Fig. 3.2c). Pulse width can directly be measured with an autocorrelator, alternatively the obtained fluorescence signal can be maximized. For correction of the spatial dispersion the aim is to obtain a uniform round focus shape in the FOV center with a 'full width at half maximum' (FWHM) of around 1 μm. The performance is best evaluated by imaging small (100-500 *nm*) fluorescent beads (Fig. 5.2). Note that an optimal compensation of spatial dispersion is only possible in the FOV center, and that the lateral resolution and beam ellipticity worsen towards the FOV edges and corners. The basic steps for the alignment of the microscope are as follows:

1. We took out the AODs, $\lambda/2$-waveplates and the DCU by removing the clamps from the X95-column.
2. Next we adjusted the two in-coupling mirrors that steer the laser beam into the microscope to ensure a stable laser beam alignment during stage movements (check with iris).
3. We used two or more irises to center the beam on all lenses and the objective (we also centered the laser beam on the mirrors M1 and M2).
4. After that we re-mounted the AOD scanners.
5. While driving the AODs at their center frequency we centered the laser beam by shifting the AODs laterally with respect to the laser beam.
6. Subsequently we adjusted the pitch/jaw platform below the AODs to optimize the incident angle and ensure maximum laser beam deflection efficiency (laser intensity was measured with the power meter).
7. We next installed the DCU and adjusted the incident angle of the laser beam to be close to 53° for the SF11 prism (close to 69° for the NSF 66 prism). We then realigned the laser beam behind the DCU with respect to the AODs while trying to maintain a distance between AODs and DCU-prism of about 35 *cm* which in our system nearly restored the original pulse width (Fig. 5.1).
8. Next step, we installed and adjusted the first $\lambda/2$-waveplate in front of the prism to ensure maximum laser beam transmission through the prism (measure with the power meter).

9. Then we installed the second $\lambda/2$-waveplate in front of the AODs and turned the polarization to maximize the AOD-diffraction efficiency (laser intensity was measured with the power meter).

10. We imaged small ($\leq 500\ nm$) fluorescent beads and adjusted the laser beam incident angle of the prism to achieve a homogenous bead resolution in the FOV center (round beads in the FOV center). Note: The laser beam needs to be realigned with respect to the AODs by using the two parallel mirrors of the DCU each time the incident prism angle is changed.

11. To optimize compensation of the temporal dispersion the complete DCU was shifted parallel to the X95-column. The optimal setting (shortest pulses below the objective) was achieved when the fluorescence signal was maximal. Note: We recommend performing this optimization during AOD-scanning; we realigned the laser beam for maximal signal each time after shifting the DCU.

12. During regular maintenance we recommend to first of all check the alignment of the two key components (AODs and compensation prism) which we could slightly adjust without any major laser beam run off.

3.6 Scan-software development in LabView.

To control the hardware of the AOD laser scanning microscope (Fig. 3.1a) we developed a custom scanning software ('Focus-AOD') which allows to employ standardized multifunction boards such as PXI-6229 or PXI-7813R (National Instruments, Austin, USA) for simultaneous data acquisition and control of the scanning signals. As a main function the scan-software controls the FPGA integration board which calculates and triggers the acousto-optic radio frequencies that are necessary to drive the acousto-optic deflectors to scan the laser beam. Simultaneously the scan software acquires pixel data from the photomultiplier tubes (PMTs) and integrates these values via the FPGA-card. Then these pixel data are further processed for proper real-time image visualization during the experiment. Furthermore the 'Focus-AOD' software allows a simultaneous read out of three separated input channels (14-bits each) while it should be easily adaptable to increase the number of channels for data acquisition. In principle no further data acquisition hardware except the FPGA and a fast analog-digital (A/D) -converter is required for either scan signal control nor for data acquisition (see Fig. 3.4).

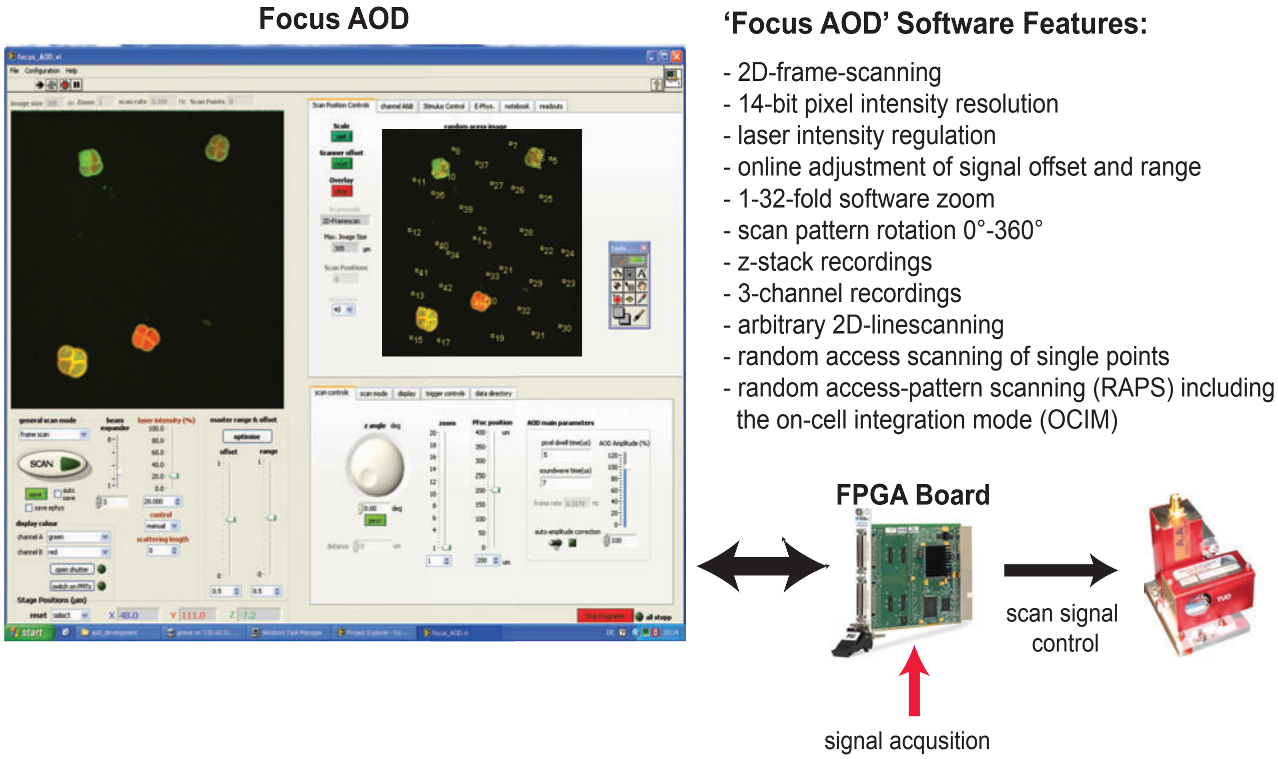

'Focus AOD' Software Features:

- 2D-frame-scanning
- 14-bit pixel intensity resolution
- laser intensity regulation
- online adjustment of signal offset and range
- 1-32-fold software zoom
- scan pattern rotation 0°-360°
- z-stack recordings
- 3-channel recordings
- arbitrary 2D-linescanning
- random access scanning of single points
- random access-pattern scanning (RAPS) including the on-cell integration mode (OCIM)

Figure 3.4: *Screen shot of the Focus-AOD-scan software within the LabView environment*

While typical pixel dwell times in biological laser scanning microscopy are about 2-3 μs this can be increased or further shortened by simply changing the software parameters accordingly which also applies to the sound wave waiting time (discussed below). For the minimum zoom factor the final size of the image only depends on the microscope optics and the maximum scan angles of the AODs.

Multi channel integration. Many applications including *in vivo* calcium imaging can involve the use of two or even more dyes with different spectral properties (e.g. the combination of the calcium sensitive dye OGB-1 and the red calcium insensitive dye Alexa Fluor-594). On the detection side the optical detector pathways can be easily designed to separate and simultaneously collect both of the emitted wavelengths in separate channels. To match this need our Focus-AOD software allows to acquire and process three separate fluorescence channels independently. Thereby the data of each channel is collected, processed, and displayed simultaneously in real time.

Random-access scanning modes. The key feature for gaining measurement speed was however to implement the random-access scanning mode which allowed to fully restrict scanning to regions of interest or neurons. To improve the signal to noise ratio (SNR) of fluorescence recordings from neuronal somata it is desirable to increase the signal integration time per neuron. The scanning software allows scanning of a pre-defined, fixed, spatial pattern of a few points on each neuron. We termed this scanning mode random-access pattern scanning (RAPS) and mostly used a 5-point pattern that could be scaled to match the size of a cell soma. In our setup 5-point RAPS can sample 16,700 locations per second (83,000 single points/sec). Figure 3.5 demonstrates the working principle of the random-access scanning mode that has been finally implemented in the 'Focus-AOD' scanning software (for further descriptions and evaluations of the RAPS modes see the results section).

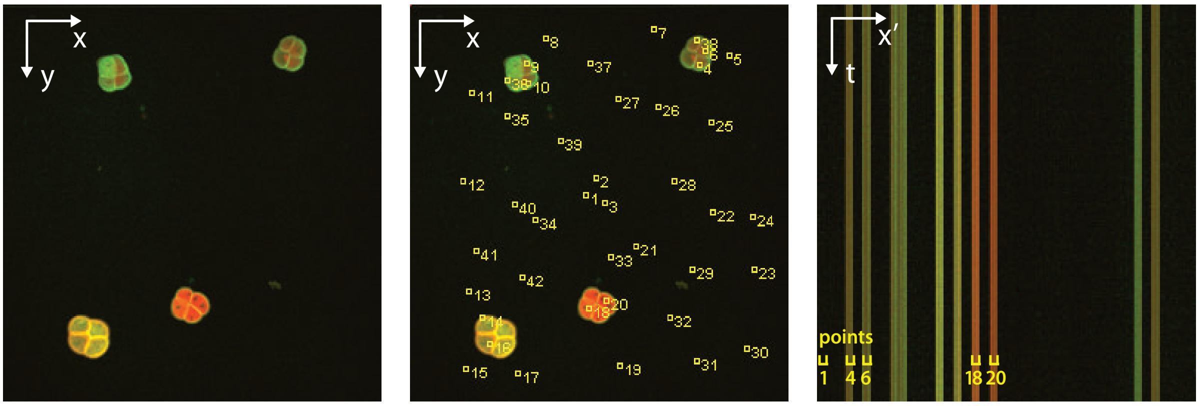

frame-scanning scan-point selection random acess scanning

Figure 3.5: *Testing of the random-access pattern scanning mode. After a single frame scan was performed (**left**, image of pollen grains) the user can manually select points within the previously acquired image (**middle**). On each preselected point a small pattern of several points is scanned within the area that is marked by yellow circles. In the random-access image (**right**) the x-lines chronologically represent all preselected scanning positions while the y-axis gives the repetition (in this case 396 times per second) corresponding to a scan rate of 396 Hz. In the random-access scan image (right) five example points are marked.*

4 Experimental methods for in vivo imaging

This chapter describes the experimental techniques that were used for *in vivo* 2-photon imaging. This includes the preparation of the animal and the staining procedure, the 2-photon imaging and the electrophysiological measurements, and the working principles of the automated data analysis algorithm that allowed to extract neuronal spiking from the obtained fluorescence data traces.

4.1 Mouse preparation and fluorescence labeling

All animal procedures were carried out according to the guidelines of the Center for Laboratory Animals of the University of Zurich and were approved by the Cantonal Veterinary Office. Wild-type mice (16-28 days old) were anesthetized with urethane (1.2-1.5 g/kg of body weight, i.p.) or isoflurane (1-2% in oxygen). A craniotomy above the cortex was prepared as described previously [Kerr et al., 2005,Nimmerjahn et al., 2004]. The dura was carefully removed and the exposed cortex was superfused with normal rat Ringer (NRR) solution (135 mM $NaCl$, 5.4 mM KCl, 5 mM $Hepes$, 1.8 mM $CaCl_2$; pH 7.2 with $NaOH$). To dampen heartbeat- and breathing-induced motion the cranial window was filled with agarose (type III-A, Sigma, Buchs, Switzerland; 1% in NRR) and covered with a glass cover slip.

Cell populations were labeled in superficial neocortical layers with the calcium indicator Oregon Green BAPTA-1 AM (Molecular Probes, Invitrogen, Basel, Switzerland) using the multi-cell bolus loading technique [Stosiek et al., 2003,Garaschuk et al., 2006b]. In brief, 50 μg of OGB-1 AM were dissolved in Dimethylsulfoxid (DMSO) plus 20% Pluronic F-127 (BASF, Ludwigshafen, Germany) and diluted in NRR to a final concentration of about 1 mM. This solution was pressure-ejected into neocortical layer 2/3 of the barrel cortex or the visual cortex using a micropipette [Stosiek et al., 2003]. Brief application (10 min) of SR101 (50 μM in NRR) to the exposed neocortical surface resulted in co-labeling of the astrocytic network [Nimmerjahn et al., 2004].

4.2 Calcium imaging and electrophysiology.

Frame scanning with 10 μs pixel-to-pixel transition time and 2-3 μs pixel dwell times was used to obtain overview images of neuronal populations in L2/3. Groups of cell somata in the focal plane were manually selected for random-access scanning, and cell positions were saved. Fluorescence signals were recorded using RAPS to maximize the SNR while minimizing bleaching effects. In this study we mainly used a cross-like 5-point pattern with point-to-point distance of 1.5 μm so that all points were contained within the somatic area. The total scan time per cell was 60 μs with an effective on-cell signal integration time of 50 μs (further details are provided within the results section). In this study we used a calcium sensitive fluorescent indicator dye (OGB-1) that indirectly reports neuronal activity via a change in its fluorescence signal. Thus somatic fluorescence signals were always expressed as relative fluorescence changes ($\Delta F/F$) after subtraction of the background which was determined from a position inside a blood vessel lumen. All fluorescence traces and electrophysiological signals were analyzed with IGOR Pro software (Wavemetrics Inc., Lake Oswego, USA).

Juxtacellular recordings were obtained from OGB-1 loaded L2/3 neurons. Cells were visually targeted in the frame scan mode of the AOD 2-photon microscope. Borosilicate glass pipettes with open tip resistances between 4-8 $M\Omega$ were filled with extracellular solution containing Alexa 594 (50 μM, Molecular Probes, Invitrogen, Basel, Switzerland) for pipette visualization. Electrical signals were recorded with an Axoclamp 2B amplifier (Axon Instruments, Foster City, USA) and digitized at 10 kHz with a PXI-6229 data acquisition card (National Instruments, Austin, USA). For electrical stimulation experiments 200 μs pulses (0.1-1 mA) were delivered through patch pipettes placed within the imaging area [Histed et al., 2009]. Sensory stimulation of the barrel cortex was performed by 30 ms air puffs to the whiskers on the contralateral side of the face. Visual stimulation was performed by presenting a 10 s natural contrast movie to the mouse's contralateral eye (movie 161 from a published database [van Hateren and Ruderman, 1998]).

4.3 The automated analysis of fluorescent data traces

For the automated analysis of the fluorescence data traces that have been recorded on neuronal somata an automated spike reconstruction algorithm was developed with the aim to extract the underlying spiking pattern from the fluorescence recordings (see Fig. 1.7 and Fig. 1.8). Because the working principle of this algorithm is to iteratively subtract ('peel off') single AP-evoked calcium transient waveforms from superimposed calcium fluorescence transients, we termed this algorithm "peeling algorithm". The automated peeling algorithm that was used for the analysis of the high-speed fluorescence recordings is computationally simple and can be effectively generated as a fast procedure by implementing the following steps (see also Fig. 5.14 and Supplementary Movie 2):

Event detection. All calcium transients (here termed 'events') were detected using a Schmitt-trigger approach with additional criteria. A Schmitt-trigger searches point-by-point through a trace for events that first pass a high threshold and then stay elevated above a second lower threshold for at least a certain minimum duration. Shorter events are discarded. In our implementation we used +2S.D. of the baseline noise (4.2%) as high threshold, -1S.D. (-2.1%) as low threshold and typically 70 ms as minimum event length. To render the algorithm less sensitive to drifts in the baseline a Schmitt-trigger in a sliding window was applied where a baseline was fit with a linear regression in a 0.4 s window before the current event time. Offset and slope of this baseline were taken into account for the Schmitt-trigger evaluation. An event detected by the Schmitt-trigger had to fulfill two additional criteria to be accepted. First the integral of the baseline-corrected fluorescence trace in the event window (from high to low threshold) was calculated and compared to the integral of a reasonable expectation of a 1AP-evoked calcium transient. The event was only accepted if the ratio of these two integrals was above 0.5 indicating a high probability that at least one AP has occurred. The rounded ratio of the integrals was also used to estimate the number of nearly-simultaneously occurring APs; a ratio between 1.5 and 2.5 indicated an AP-doublet. As second criterion a similar integral comparison was performed on a shorter time window (within 40-60 ms after high-threshold crossing) to ensure that only events with rather sharp onsets - as expected for AP-evoked calcium transients [Markram et al., 1995] - were selected. For accepted events the routine took the time point of high-threshold crossing as the initial guess of the event start.

Onset fit. Onsets of detected events were fitted within a window of ±40 ms for 300 Hz cell sampling rate (±60 ms for 200 Hz cell sampling rate) around the initial guess t_0 from the event detection routine with the following function:

$$\begin{aligned} f_{onset} &= A \quad (1 - e^{-\frac{(t-t_0)}{\tau_{on}}}) \quad e^{-\frac{(t-t_0)}{\tau_1}} && for \quad (t > t_0) \\ &= 0 && for \quad (t \le t_o) \end{aligned} \tag{4.1}$$

where A is the transient amplitude, τ_{on} is the onset time constant, t_0 is the onset time point, and τ_1 is the decay time constant. Before fitting baseline offset the linear drifts were subtracted from the trace segment. An exponentially decaying component (τ_1 set to a fixed value of 70 ms) was included because fluorescence traces typically already started to decay within the chosen time window. The free parameters were t_0, τ_0, and A. t_0 was constrained to the fitting window and τ_{on} was constrained to 2-30 ms to avoid artificially steep or shallow onsets. The major goal of onset fitting was to obtain a good estimate of t_0.

Fit and subtract the next 1AP-evoked fluorescence transient. The high-speed measurements revealed that the decay of AP-evoked somatic calcium transients in most cases could not be well described with a single-exponential curve. Several decay components may be expected as the spatiotemporal dynamics of intracellular calcium concentration in the soma is governed by multiple processes including calcium diffusion and buffering in the cytosol and in the nucleus as well as uptake and extrusion mechanisms [Berridge et al., 2003]. We therefore used a calcium transient waveform with sharp exponential onset and a slower double-exponential decay to fit the entire fluorescence trace:

$$\begin{aligned} f_{Ca}(t) &= (1 - e^{-\frac{(t-t_0)}{\tau_{on}}}) \quad (A_1 \quad e^{-\frac{(t-t_0)}{\tau_1}} + A_2 \quad e^{-\frac{(t-t_0)}{\tau_2}}) && for \quad (t > t_0) \\ &= 0 && for \quad (t \leq t_o) \end{aligned} \tag{4.2}$$

A_1, A_2, τ_1, and τ_2 were fitting variables while t_0 and τ_{on} were constrained to the values determined by the onset fitting routine. The fit range was from t_0 to t_0+1.5 s thereafter.

For the juxtacellular recordings spike times t_s were determined as the time point of the positive peak of the extracellular spike which coincides with the steepest rise in membrane potential during the AP. Since the evoked calcium influx occurs during the repolarizing AP-phase [Borst and Helmchen, 1998] which is about 1 ms after the steepest rise in neocortical pyramidal neurons [Waters and Helmchen, 2006] we calculated the time difference between optical estimate and actual spike time as $\Delta t = t_0$ - $(t_s$+1 $ms)$.

In our implementation an estimate of the 1AP-evoked calcium transient waveform from the combined electrical (juxtacellular) and optical recordings was used for subtraction (Fig. 5.10c). To accommodate slight cell-to-cell variations in calcium transient amplitude this waveform was scaled in some experiments (0.7-1.3 scale factor). To prevent subtraction of erroneous events an 'integral check' was performed: subtraction of the 1AP-evoked calcium transient was only accepted if it did not produce a negative integral in the residual trace (more than 50% of the resulting negative integral of a 1AP-evoked transient); otherwise the subtraction was undone and the procedure moved on to the next event found. For accepted events the algorithm 'jumped back' on the trace (typically 200 ms) and started the search for the next event.

To assess the amount of dye saturation during repetitive electrical stimulation (Fig. 5.16) first the maximal relative fluorescence change $\Delta F/F_{max}$ under our experimental conditions was experimentally determined. Following the usual OGB-1 staining procedure L2/3 neurons were deliberately destroyed by applying strong electrical shocks through a local micropipette while simultaneously monitoring fluorescence changes. Analysis of neurons for which cell damage was obvious because of a sudden fluorescence increase to a stable ceiling value yielded an average $\Delta F/F_{max}$ value of 93±15% (n=10 cells; mean±S.D). Together with reasonable assumptions of a 50 nM concentration for the resting intracellular $[Ca^{2+}]_i$ [Helmchen et al., 1996, Maravall et al., 2000] and of 200 nM for the dissociation constant K_d (OGB-1, [Maravall et al., 2000]) we thus could convert the average 1AP-evoked $\Delta F/F$ transient into a $[Ca^{2+}]_i$ transient using the standard single-wavelength conversion equation:

$$[Ca^{2+}]_i = \frac{[Ca^{2+}]_{rest} + (K_d \ \frac{(\Delta F/F)}{(\Delta F/F)_{max}})}{1 - \frac{(\Delta F/F)}{(\Delta F/F)_{max}}} \tag{4.3}$$

The calculated 1AP-evoked $[Ca^{2+}]_i$ transient had a peak amplitude of about 10 nM, which is consistent with previous calibrated $[Ca^{2+}]_i$ measurements from neocortical cell somata [Schiller et al., 1995]. We then calculated $[Ca^{2+}]_i$ elevations during burst stimulation at different frequencies by assuming linear superposition of the individual $[Ca^{2+}]_i$ transients (Fig. 4.1). Nevertheless the linear superimposed $[Ca^{2+}]_i$ traces seemed to show some degree of saturation; however this misleading impression was due to the combination of the finite onset time of the transient and the fast initial decay component (Fig. 4.1a). The $[Ca^{2+}]_i$ accumulations were then converted back into expected $\Delta F/F$ changes according to:

$$\frac{\Delta F}{F} = (\frac{\Delta F}{F})_{max} \quad \frac{[Ca^{2+}]_i - [Ca^{2+}]_{rest}}{([Ca^{2+}]_i + K_d)} \tag{4.4}$$

The $\Delta F/F$ traces qualitatively looked similar to the linearly summed $[Ca^{2+}]_i$ traces and an analysis of the $\Delta F/F$ change evoked by the last stimulus in a burst revealed that the elementary $\Delta F/F$ was reduced only little even for the strongest stimulus (maximal reduction 20%; Fig. 4.1b). The simulated model traces also were very similar to actual experimental data (Fig. 4.1c). From this analysis we conclude that even with 40 Hz stimulation the observed fluorescence can be well approximated by a linear summation of elementary transients (see results of the peeling algorithm in 4.1d).

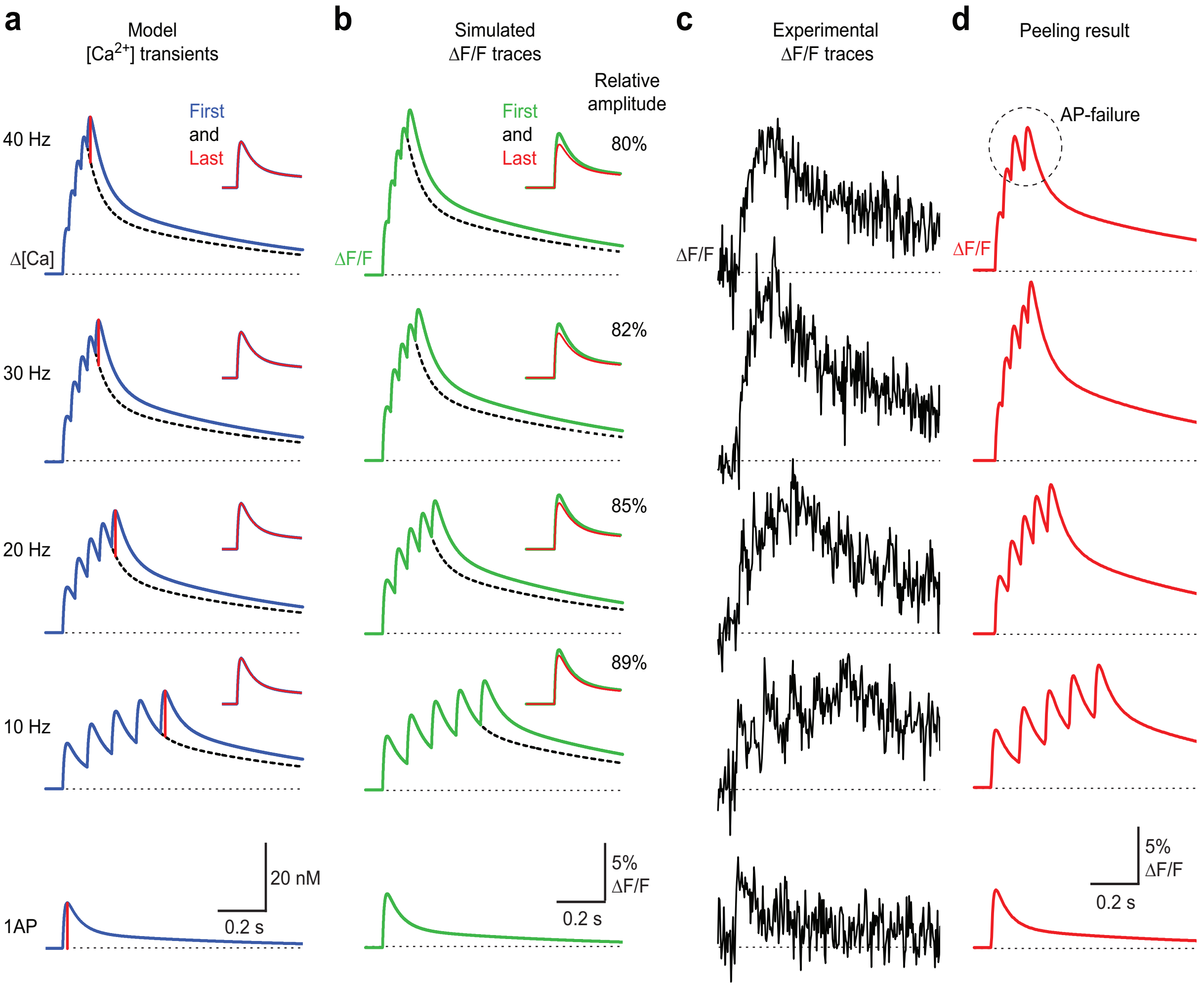

Figure 4.1: *Modeling the summation of calcium transients and fluorescence traces with burst stimulation indicates a small effect of dye saturation. Summation of simulated* $[Ca^{2+}]_i$ *transients (a) , simulated OGB-1 fluorescence transients (b), measured OGB-1 fluorescence traces (c), and model traces resulting from applying the peeling algorithm (d) to the data in (c).* ***(a)*** *1AP-evoked* $[Ca^{2+}]_i$ *transients were linearly summed at different frequencies so that the amplitude of individual transients (red lines) stayed the same independent of the* $[Ca^{2+}]_i$ *level (red vertical lines). In particular the last transient - calculated as the difference of the 5AP- minus the 4AP-transient (dashed line) - is always identical to the 1AP-evoked transient.* ***(b)*** *OGB-1 fluorescence transients were calculated from the* $[Ca^{2+}]_i$ *transients in (a) using the single-wavelength conversion equation with the parameters* $[Ca^{2+}]_{rest} = 50$ *nM,* $K_d = 200$ *nM, and* $(\Delta F/F)_{max} = 93\%$*. For each stimulus train the last* $\Delta F/F$ *transient was calculated as the difference of the 5AP- minus the 4AP-transient. Due to partial dye saturation the amplitude of the last* $(\Delta F/F)$ *transient shows a small reduction (maximally to 80%) at elevated* $[Ca^{2+}]_i$ *levels.* ***(c)*** *Examples of measured OGB-1 fluorescence transients with the same stimulation protocol for comparison.* ***(d)*** *Model traces extracted with the peeling algorithm for the traces in (c). The peeling algorithm (assuming linear summation and neglecting dye saturation in our implementation) resulted in a good reconstruction of the underlying* $[Ca^{2+}]_i$ *changes. Note: a putative failure of eliciting an AP for a certain stimulus is predicted by the peeling algorithm for the 40 Hz stimulation.*

5 Results

While the previous chapter describes the design and development of the AOD 2-photon laser scanning microscope, this chapter mainly focuses on the characterization of the microscope parameters such as the imaging resolution and the imaging speed for measuring fluorescence signals from neuronal cell populations. In detail this chapter covers the following aspects: (**1**) an elaborate description of the microscope properties, (**2**) the scanning and signal integration modes which allowed to monitor activity from numerous cells within a neuronal network, (**3**) the accuracy to reconstruct the underlying neuronal spiking activity from the optical fluorescence recordings, (**4**) the precision to detect neuronal action potential bursts, (**5**) the application of a novel automated spike extraction algorithm that enables to extract the underlying neuronal spiking patterns from fluorescence recordings. Finally this chapter includes a short demonstration of how the novel scanning technique facilitates *in vivo* measurements of neuronal network activity that has been measured in the barrel cortex and the visual cortex of living mice.

5.1 Evaluation of the spatial resolution of the AOD-microscope

Our first goal was to design an AOD-based 2-photon microscope suitable for *in vivo* application. We custom-built a microscope setup that uses a pair of crossed AODs for two-dimensional deflection of the laser beam (Fig. 5.1a). A critical issue in employing AODs for 2-photon excitation is that spatial and temporal dispersion cause laser focus deformation and pulse broadening respectively. Here, we adopted a single-prism compensation approach [Zeng et al., 2006] and modified it to improve laser beam transmission and dispersion compensation over a large FOV (Fig. 3.2a,b). Compensation with the prism abolished elliptic deformation of the laser focus as illustrated by imaging small fluorescent beads in the FOV center (Fig. 3.2b). Two $\lambda/2$-waveplates before the prism and the first AOD, respectively, optimized laser beam polarization along the pathway and maximized transmission through prism (85%) and AOD pair (55%). In total 45% of the incoming light was transmitted by the dispersion compensation unit (DCU) and the AODs (Fig. 3.2a).

We quantitatively characterized the spatial resolution by imaging 100 nm fluorescent beads (Fig. 5.2 and Table 5.1). In the FOV center lateral spatial resolution was uniform with 1.01±0.14 μm and 1.01±0.03 μm full width at half maximum (FWHM) in x- and

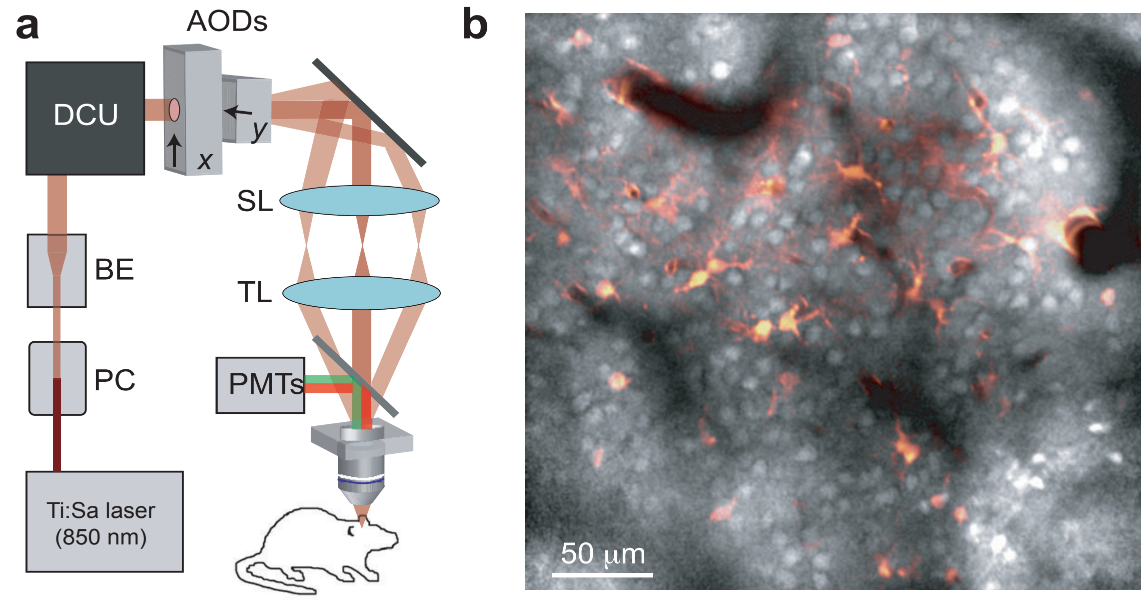

Figure 5.1: *AOD-based 2-photon imaging of neocortical L2/3 neurons in vivo. (**a**) Schematic of the 2-photon microscope setup. Laser intensity and beam size were adjusted with a Pockels cell (PC) and a variable beam expander (BE), respectively. Behind the dispersion compensation unit (DCU) two orthogonal acousto-optic deflectors (AODs) were used for x-y scanning. (**b**) 2-photon image of a cell population stained with OGB-1 in L2/3 of mouse neocortex at 200 μm depth below the pia. Astrocyte labeling with* SR101 *is overlaid in red.*

y-direction within the scanning areas respectively (ellipticity 1.0; n=4 beads, mean±S.D.; ellipticity 3.5 without compensation). With slightly underfilled AOD aperture (D = 7.9 mm) we calculate (see equation 2.19) 342 resolvable spots and - given our FOV of 305 μm x 305 μm - a theoretical focal spot size of about 0.9 micron which is in close agreement with the results from the bead measurements (Fig. 5.2). We thus conclude that the small scan angle of the AODs rather than the diffraction limit of the underfilled objective (which would yield about 0.5 μm resolution) is the major limiting factor for spatial resolution in our microscope. Because efficient *in vivo* imaging of cell bodies over a significant FOV size was our primary goal this spatial resolution was adequate for our purposes as demonstrated in Fig. 5.1b. Axial resolution was 4.13±0.14 μm FWHM (n=4). As expected [Kremer et al., 2008] the focus was elongated towards the FOV borders but ellipticity ratio remained below 2 throughout the entire FOV (lateral and axial resolution remained below 2 μm and 6.5 μm respectively; Fig. 5.2 and Table 5.1). With the prism placed about 35 cm in front of the AODs, the DCU also compensated for the group delay dispersion in the entire optical path restoring laser pulse width from 570 fs without compensation to 140 fs (130 fs original pulse width) (Fig. 3.2c).

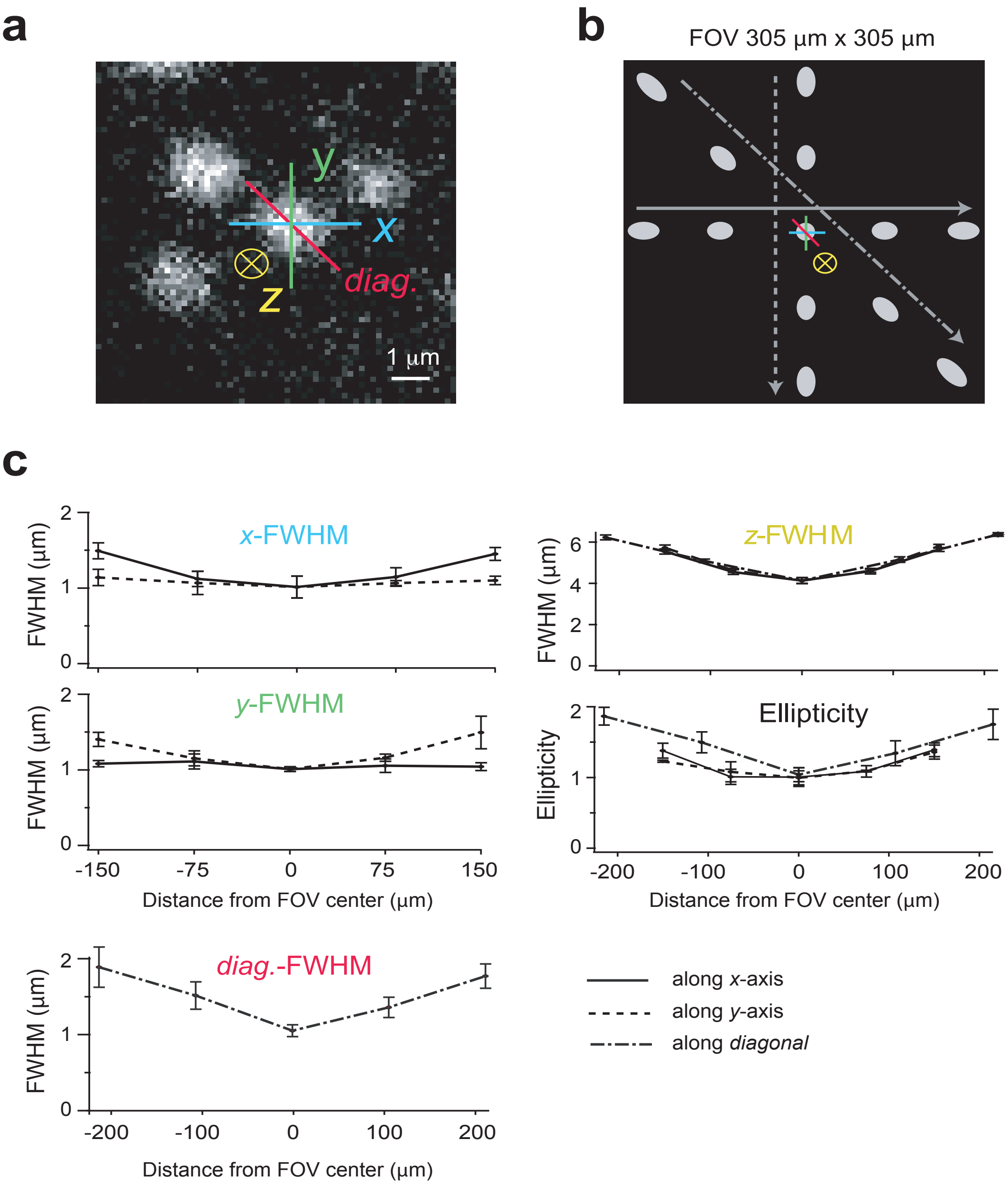

Figure 5.2: *Spatial resolution of the AOD-based 2-photon microscope with dispersion compensation. (**a**) Image of 100 nm fluorescent beads near the FOV center. Bead images are round with optimized dispersion compensation. The x-, y- and z-axes are indicated. Scale bar 1 µm (**b**) Inhomogeneity of spatial resolution over the FOV with optimized dispersion compensation. Beads appear more elliptically closer to the FOV borders. Schematic bead images are shown 20x magnified for better visualization. FWHM values and ellipticity were analyzed along the x-axis (straight arrow), the y-axis (dashed arrow) and the diagonal axis (dashed-dotted arrow). (**c**) Left: FWHM of individual beads (n=4 each) along x-axis (top), y-axis (middle) and the diagonal (bottom) as a function of distance from FOV center. The x-FWHM increases only along the x-direction (straight lines) while the y-FWHM increases only along the y-direction (dashed lines). Right: FWHM along the z-axis (top) and bead ellipticity (bottom; ratio of FWHM values along the respective long and short resolution axes) as a function of distance from FOV center.*

distance from center	x-FWHM	y-FWHM	z-FWHM	diag.-FWHM
-150 μm	1.49 μm	1.40 μm	5.54 μm	1.88 μm
-75 μm	1.12 μm	1.15 μm	4.57 μm	1.52 μm
FOV center, 0 μm	1.01 μm	1.01 μm	4.13 μm	1.05 μm
+75 μm	1.14 μm	1.16 μm	4.58 μm	1.35 μm
+150 μm	1.45 μm	1.49 μm	5.63 μm	1.77 μm

Table 5.1: *This table shows the resolution properties of the AOD 2-photon microscope for the three main resolution axis x-, y-, z- and the diagonal axis. Resolution values have been evaluated by measuring small fluorescent beads of 100 nm size along the distortion axis respectively. Resolution values are the average FWHM of n=3-4 bead measurements.*

All these optimizations rendered our system suitable for *in vivo* imaging and provided a FOV of up to 305 μm side length (40x objective). The total transmission efficiency of our microscope was 25% at 850 nm wavelength providing a maximally available laser power (up to 700 mW) below the microscope objective. Cell populations in mouse neocortical layer 2/3 (L2/3) could be readily imaged down to 300 μm depth below the pia after multi-cell bolus loading [Stosiek et al., 2003] with the fluorescent calcium indicator OGB-1 and counterstaining of astrocytes with SR101 [Nimmerjahn et al., 2004] (see Fig. 5.1b and Supplementary Movie 1).

5.2 Fast fluorescence measurements using the Random-Access Pattern Scanning (RAPS) mode

We next implemented a random-access scanning mode for fast fluorescence measurements from various regions of interest (ROIs) that are distributed over the complete FOV. As reported by another study [Otsu et al., 2008] the transition time of AODs can be significantly shortened compared to the theoretical value. The reason is that within about 66% of the nominal transition time (given by the passage time of the sound wave across the full beam diameter at the AOD aperture) more than 90% of the laser power is redirected to the new position meaning that <1% of the 2-photon excitation remains at the original position. We adopted this approach and used a 10 μs transition time between scan angles which is 82% of the nominal transition time for our 7.9 mm beam size at the AOD aperture (12.2 μs; sound velocity 650 m/s) and 66% of the nominal transition time for the fully filled AOD aperture (15.4 μs). In agreement with the previous report [Otsu et al., 2008] we did not observe any measurable effect on image quality. For frame scanning we chose an additional 2 μs pixel dwell time resulting in a frame acquisition time of 786 ms (256x256 pixel). We first investigated whether the total fluorescence signal changes during random-access scanning of symmetric point pattern compared to a single point that can be scanned on selected ROIs. During the experiments the total signal integration time was kept constant when comparing the two scanning modes, RAPS vs. non RAPS (Fig. 5.3a). The results of n=3 bead measurements demonstrate that the fluorescence signal depends only on the signal integration time and also on the locations where fluorescence signals were measured. Assuming a homogenous ROI the total fluorescence signal for the distributed point pattern was slightly increased when compared to the single point integration (Fig. 5.3b).

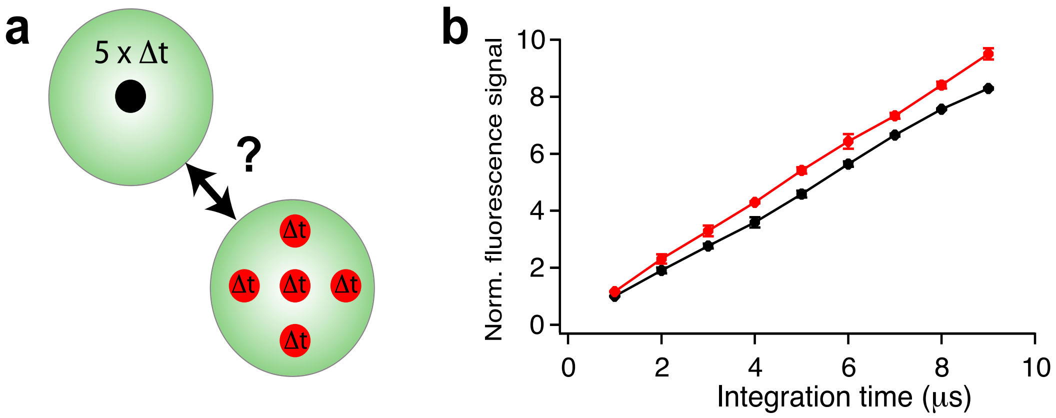

Figure 5.3: *Fluorescence signal integration during high-speed RAPS imaging. (**a**) Schematic drawing of a cell somata that can be imaged with two different scan or signal integration modes. While the total signal integration time on the cell is kept constant a single point scan or a fast sequential scan of a few scanning points (here five) can be performed. (**b**) The diagram shows the signal for increasing total cell integration times for the two cell scanning modes, single point scanning (black) and point pattern scanning (red); all values were normalized to one point scanning with a total signal integration time of 1 ms. To ensure an adequate comparison of the two scanning modes the fluorescence signals of n=3 beads were imaged sequently and averaged.*

During cell scanning of living neurons, however, it is desirable to minimize effects of photobleaching and the accompanied photo-toxicity. These effects can be minimized by distributing the total scanning and signal integration time for each neuron on the entire cell soma. In our approach we used a structured regular pattern of a few points on each target (here a fluorescent bead, see Fig. 5.4a). On the other hand shifting the laser beam from one point to another within the scanning pattern requires, due to the AOD properties, some additional 10-15 μs of time to transit the focal spot. During this shifting phase the laser beam intensity splits between the current and the next focal spot (Fig. 5.4c, lower diagram). The typical transition time was set to 10 μs (as explained above) and the size of the point pattern was adjusted to about 3 μm. To measure the fluorescence signal during the pattern scanning we continuously acquired the fluorescence signal while a pattern of nine points was sub-sequentially scanned on a fluorescent bead (Fig. 5.4b,c upper diagram). The complete integration time included the transition and an additional 2 μs pixel dwell time for each point. For all measurements the sampling rate was adjusted to 2 MHz which yielded a temporal resolution of 0.5 μs.

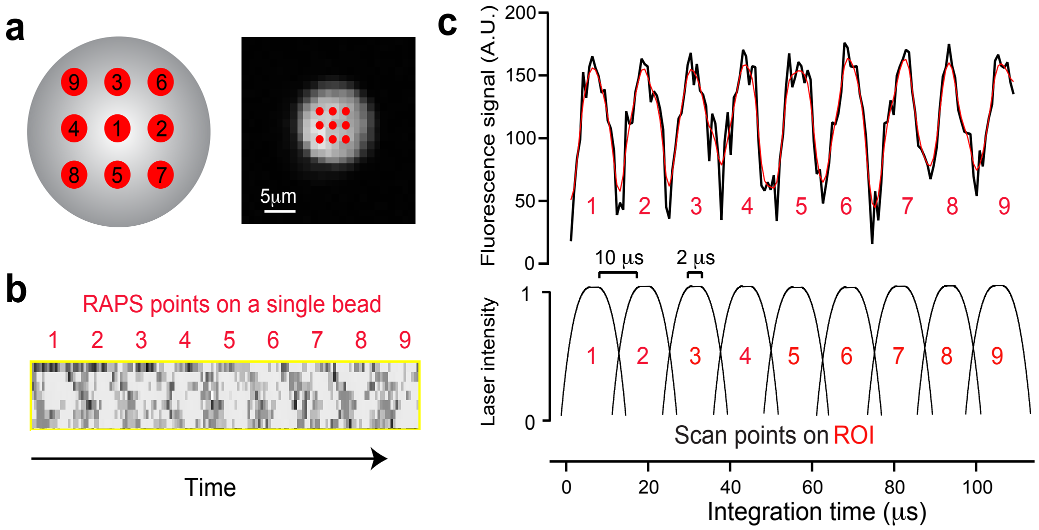

Figure 5.4: *Continuous on-target integration during RAPS imaging.* (***a***) *Schematic drawing (left) and two photon image (right) of a fluorescent bead that was scanned with the illustrated 9 point scanning pattern.* (***b***) *2-photon image of repeated random-access pattern scanning of a single beat, sampled with 2 MHz. While the fluorescence signal during the 9-point pattern scan is shown on the x-axis, the repeated measurements are shown on the y-axis which corresponds to the scanning time (108 µs for a single line or pattern; each bead was scanned 7 times).* (***c***) *The averaged fluorescence signal in arbitrary units (A.U.; n=3 beads, 5 measurements) during a 9-point random-access pattern scan on the target (upper diagram). This result is consistent with the modulation of laser beam intensity that increases until the acoustic wave has traveled through the AOD crystal (lower diagram).*

To further improve the signal acquisition of neuronal somata scanning we next implemented the on-cell integration mode (OCIM) during RAPS imaging. The OCIM continuously acquires and integrates the fluorescence signal while the laser beam is jumping within the target ROI. The signal acquisition is only blanked when the laser focus transits to the next ROI or the next neuron (Fig. 5.5a and Fig. 5.6a). This mode does not index whether the fluorescence signal comes from two points of the pattern that are both illuminated with 50% of the laser intensity or a single scan point that is illuminated with 100%. The OCIM collects the fluorescence signal from the entire target while the exact origin of the signal within the ROI is not considered. Using this extended signal integration mode we could improve the measured fluorescence signal intensity in comparison to the standard integration mode. For a typical pixel scan time of 12 µs (10 µs transition time + 2 µs pixel dwell time) we could increase the measured fluorescence signal by a factor 3.8 ± 0.2; this gain factor became smaller with increasing pixel dwell times (Fig. 5.5b). Figure 5.5c shows the exponential decrease of the fluorescence signal with increasing pixel dwell times. Please note: the total, raw fluorescence signal raises with increasing signal integration times in an almost linear manner (Fig. 5.3b). We thus conclude that the OCIM essentially gains the fluorescence signal collection. This helps to achieve a high measurement sensitivity especially when recording small fluorescence changes of neuronal spiking activity.

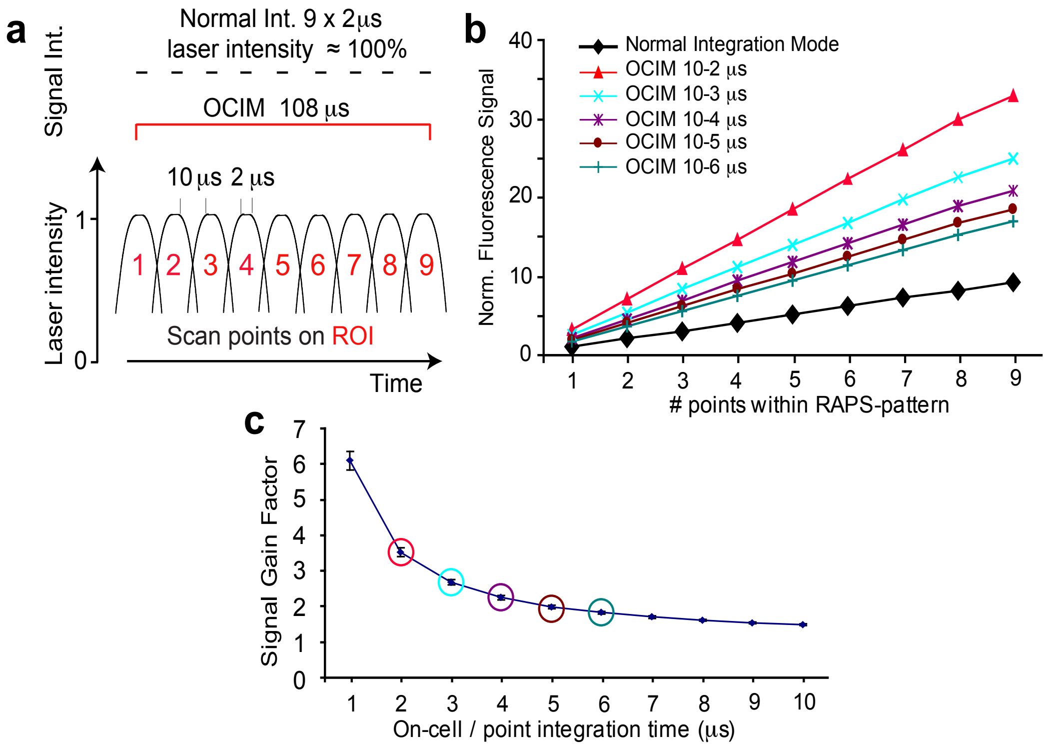

Figure 5.5: *On-cell integration signal gain factors. (**a**) Schematic illustration of the integration times of the normal cell integration and continuous on-cell integration mode (OCIM) during 9-point pattern scanning. (**b**) Comparison of the different cell integration modes depending on the number of points scanned within a pattern. Fluorescence signals were normalized to the normal integration signal for one point. (**c**) Signal gain factors were calculated as the ratio of the curves in (b) and compare the normal integration mode with the continuous on-cell signal integration mode during pattern scanning on a single target. The curve describes the gain of fluorescence signal when using the OCIMs (colored curves in b) compared to the normal cell integration mode (black curve in b). All values have been normalized to the total fluorescence signal that was acquired in the normal integration mode.*

5.3 High-speed calcium imaging of neuronal populations

For random-access scanning from neuronal cell populations *in vivo* we decided to use the OCIM to increase the fluorescence signals and to improve SNR. Furthermore we avoided stationary parking of the laser focus on each cell which may cause photo-bleaching and cell damage in living tissue [Otsu et al., 2008]. We used the RAPS mode in which a pre-defined, fixed spatial pattern of five points was scanned on each neuron. The 5-point pattern was accordingly scaled to match for the neuronal cell size (Fig. 5.6a).

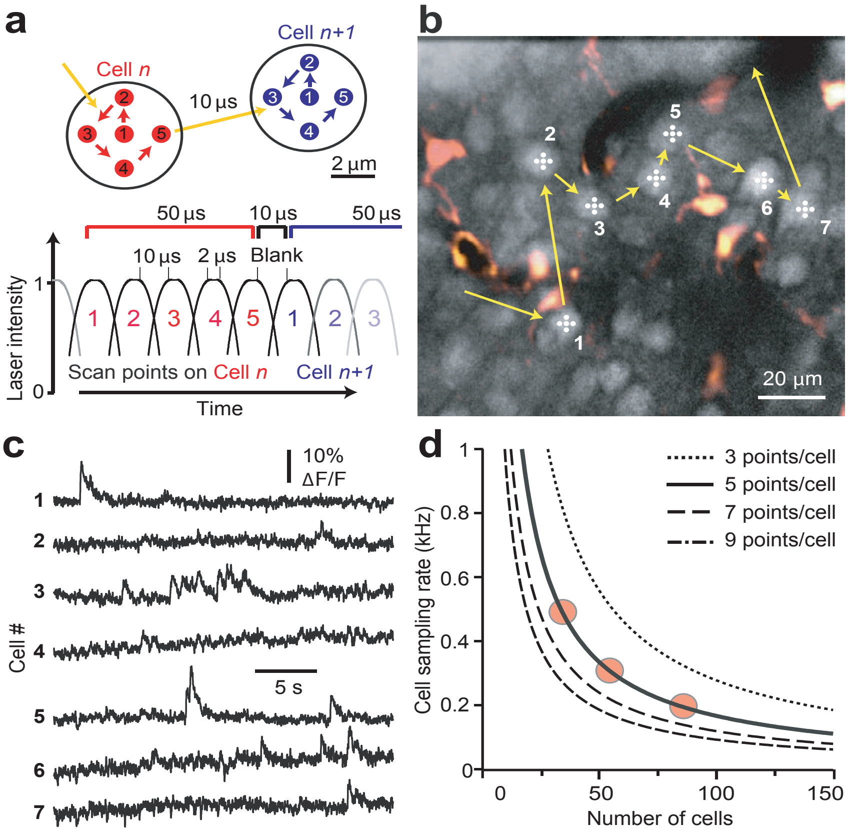

Figure 5.6: *Random-access pattern scanning from neuronal populations. (**a**) Upper panel: Principle of RAPS exemplified for a 5-point pattern that is sequentially scanned on two cell somata. Lower panel: Signal integration protocol for 5-point RAPS. Cellular fluorescence signals are integrated over the entire 5-point scan periods except for the 10 µs transition between cells. (**b**) L2/3 neuronal population labeled with OGB-1 (astrocytes overlaid in red, depth 198 µm). High-speed imaging (298 Hz sampling rate per cell) was performed using 5-point RAPS targeted to 55 cells that were manually pre-selected from a reference image. RAPS transitions for 7 example neurons are indicated. (**c**) Spontaneous fluorescence transients in the 7 example neurons depicted in (b). (**d**) Sampling rate per cell as a function of number of cells sampled and number of RAPS points per cell. The three regimes of sampling rates and cell numbers used in this study are indicated by red circles.*

After completing the pattern scan on one neuron the laser focus jumps to the next neuron where the next pattern scan is started. On each cell the fluorescence signal is continuously integrated during the pattern scan to maximize the SNR. Signal integration is only blanked during the 10 μs transition period between individual neurons resulting in a total effective dwell time of 50 μs per cell (Fig. 5.6a).

Our RAPS mode enabled high-speed calcium imaging of neuronal populations. As an example we measured spontaneous calcium transients in 55 L2/3 neurons at 298 Hz (7 cells shown in Fig. 5.6b). Spontaneous fluorescence transients with rapid onsets and amplitudes in the 5-20% range were clearly visible (Fig. 5.6c) suggesting that RAPS is well suited to resolve action potential (AP)-evoked calcium transients. In general 5-point RAPS can address 16,700 cell positions per second. Clearly the number of sampled cells trades off against the effective sampling rate per cell (Fig. 5.6d): 16 neurons can be recorded at very high rate (1 kHz), 30-40 cells at about 500 Hz, and groups of 100 cells at 167 Hz. Similar hyperbolic relationships between sampling rate and cell number hold for RAPS-patterns with different numbers of points (Fig. 5.6d and Table 5.2).

RAPS Targets	3-point RAPS	5-point RAPS	7-point RAPS	9-point RAPS
Total scan positions/s	27,600	16,700	11,900	9,300
Signal integr. time	26 μs	50 μs	74 μs	98 μs
Sampling rate for				
25 cells	1.1 kHz	660 Hz	470 Hz	370 Hz
50 cells	550 Hz	330 Hz	240 Hz	185 Hz
75 cells	370 Hz	220 Hz	160 Hz	120 Hz
100 cells	270 Hz	170 Hz	120 Hz	90 Hz
150 cells	185 Hz	110 Hz	80 Hz	60 Hz

Table 5.2: *This table shows the AOD-RAPS sampling rates in Hz for different scan pattern (3- to 9-point RAPS) and cell populations of various sizes. For all calculations we assumed a total pixel scanning time of 12 μs*

Using 5-point RAPS no signs of photo-damage such as locally increased fluorescence [Koester et al., 1999, Otsu et al., 2008] were apparent. The stability of fluorescence levels during 5-point RAPS was evaluated by measuring the baseline fluorescence from neurons that were imaged in 21 imaging sessions of 20 s duration (7 min cumulative scanning time). On average the fluorescence intensities of cells slightly decreased to 94.1± 0.1% (mean±S.D.) indicating some photobleaching (n=80 cells from three measurements; Fig. 5.7). Neighbouring control neurons which were not included in the RAPS recording (control neurons were only rarely imaged with frame scans every 30 s) showed stable fluorescence intensity (97.4±2.5%, n=10 cells, mean±S.D.). The observed fluorescence decrease was not special to 5-point RAPS as a similar decrease was seen for neurons that were imaged using galvanometric frame-scanning with a standard 2-photon microscope at similar laser power and similar total dwell time per cell (decrease to 91.3±0.9%; mean±S.D.; n=25 cells from three measurements; Fig. 5.7).

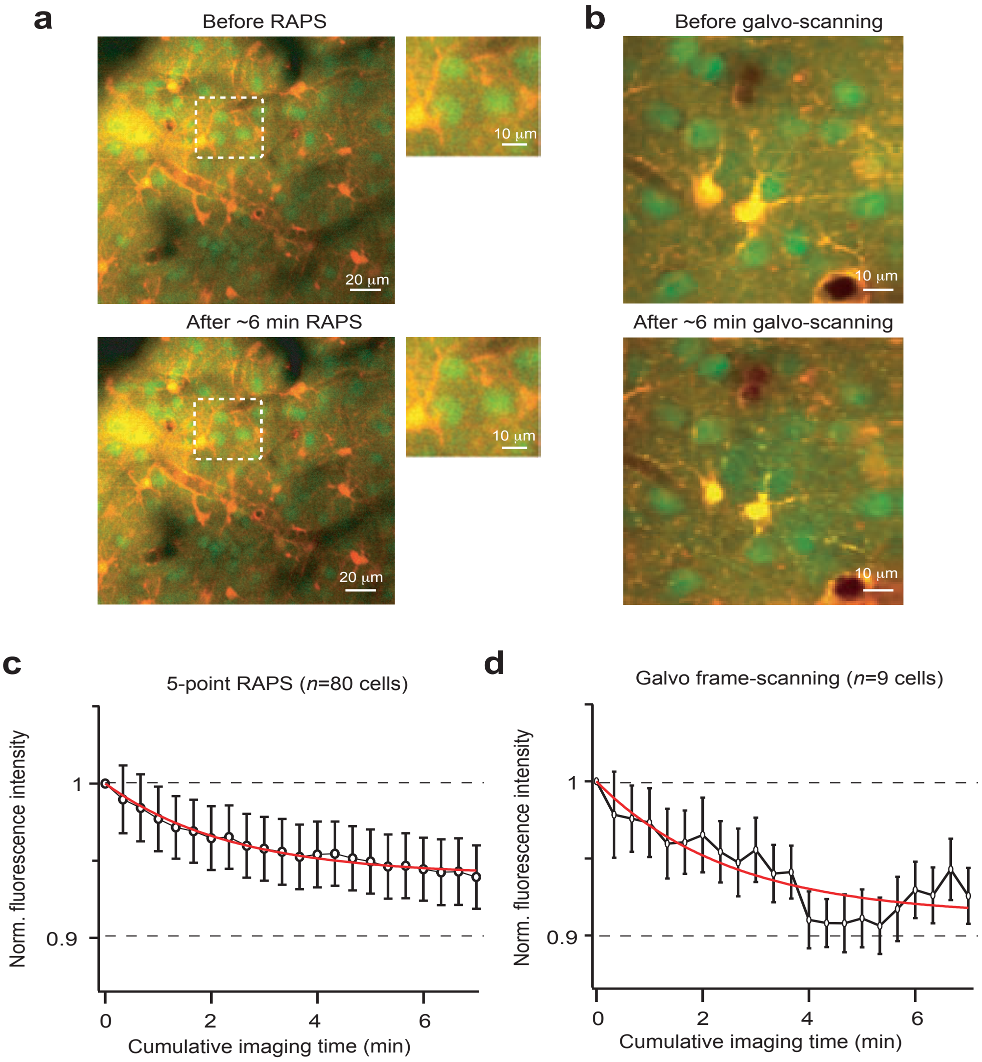

Figure 5.7: *Photobleaching during prolonged imaging is similar for RAPS and galvanometric scanning. (**a**) Image of an OGB-1 labeled L2/3 neuronal population in mouse barrel cortex before and after 6 minutes of cumulative 5-point RAPS recording at constant average laser beam power (51 cells sampled; 327 Hz sampling rate). Zoom images: Magnification of three selected cells before and after 6 min of 5-point RAPS demonstrating the absence of any morphological changes. (**b**) OGB-1 labeled L2/3 neuronal population in mouse barrel cortex imaged with a standard galvanometric 2-photon microscope before and after 6 minutes of cumulative imaging with comparable laser power as in (a) (10 cells sampled; 10 Hz sampling rate). The total dwell time per cell was adjusted to be comparable to 5-point RAPS. (**c**) Baseline fluorescence intensity values of cell somata decreased only slightly during seven minutes of 5-point RAPS recordings or galvanometric frame scanning. (**d**) Cell illumination times of the galvanometric frame scanning were adapted to match the AOD-scanning. Fluorescence intensities were normalized for each cell to the initial value of the first recording sessions. Between all 21 repetitions of 20 s long imaging sessions short breaks of at least 20 s duration were made. Fitting exponential curves to the data yielded similar fluorescence decreases by 5.9±0.1% (RAPS) and 8.7±0.9% (galvo) over seven minutes imaging time; mean±S.D.*

5.4 Electrical recordings reveal reliable optical detection of neuronal spikes with near-millisecond precision

To directly examine whether single APs can be detected, and how precisely their timing can be inferred from the fluorescence traces we combined RAPS with juxtacellular electrical recordings from individual neurons (Fig. 5.8a). We obtained simultaneous optical and electrical recordings from 10 L2/3 neurons in mouse barrel cortex using three different cell sampling conditions (n=3 at 181-228 Hz, groups of 72-91 cells sampled; n=4 at 321-327 Hz, 51-55 cells sampled; n=3 at 490 Hz, 34 cells sampled). In all cases single AP-evoked (1AP-evoked) calcium transients could be clearly resolved (Fig. 5.8b and Fig. 5.10a).

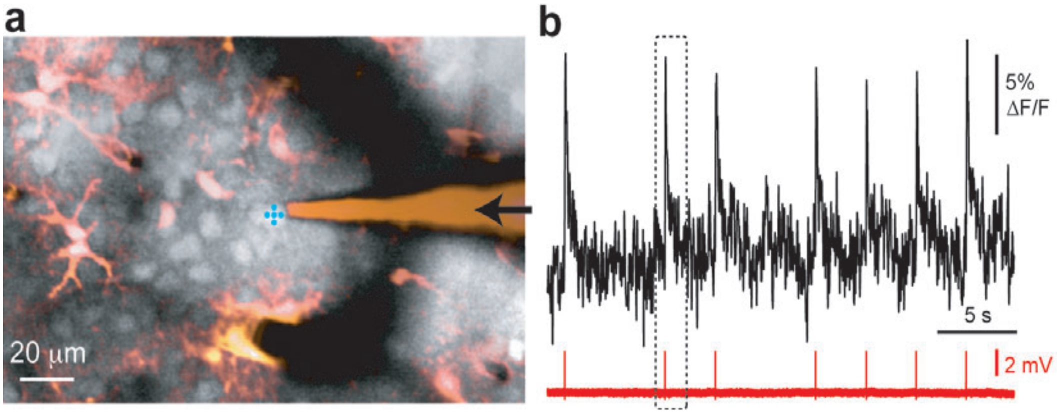

Figure 5.8: *The combination of optical RAPS imaging and cell attached electrical recordings allows to infer spike times from AOD-based optical recordings. (**a**) L2/3 neuronal population labeled with OGB-1 (astrocytes overlaid in red). A juxtacellular recording was obtained with a patch pipette (arrow) from the neuron marked with the 5-point RAPS pattern. (**b**) Simultaneous fluorescence measurement and electrical recording of the neuron marked in (a). This neuron was one out of 51 neurons sampled at 327 Hz using 5-point RAPS. Calcium transients evoked by spontaneously occurring APs were clearly resolved. The fluorescence trace was smoothed with a 5-point box filter.*

Examples of 1-AP evoked calcium transients of all evaluated cells are shown in Figure 5.9. While the coarse shape of the 1-AP evoked calcium transient seems to be conserved for all cells (steep exponential onset, followed by a slower exponential decay) each cell showed small variations in the transient peak amplitude, in the onset steepness and for the decay time. For a quantitative analysis of the reliability of spike detection we developed an automated event detection algorithm based on a Schmitt-trigger approach. From 293 total events, that were mainly single APs but also a few AP doublets, 280 (95.5%) were correctly detected and 13 missed (4.5% false negatives; 23 *min* cumulative recording time). Five events were incorrectly assigned (1.7% false positives). All AP-doublets (2-10 *ms* inter-spike interval) were detected and 77% of them (17 out of 22) were correctly identified as doublets by the algorithm based on the expected integral of a 1AP-evoked calcium transient. The reliability of event detection was independent of whether spikes occurred spontaneously (1.5% false positives; 1/67 events), or whether they were evoked by whisker-stimulation (1.8%; 4/221). Each fluorescence transient detected was fitted in a two-step procedure with a model function comprised of a single-exponential rise and a double-exponential decay. Two decay components were chosen because a rapid initial decay phase was apparent in the large majority of transients (Fig. 5.9 and Fig. 5.10a).

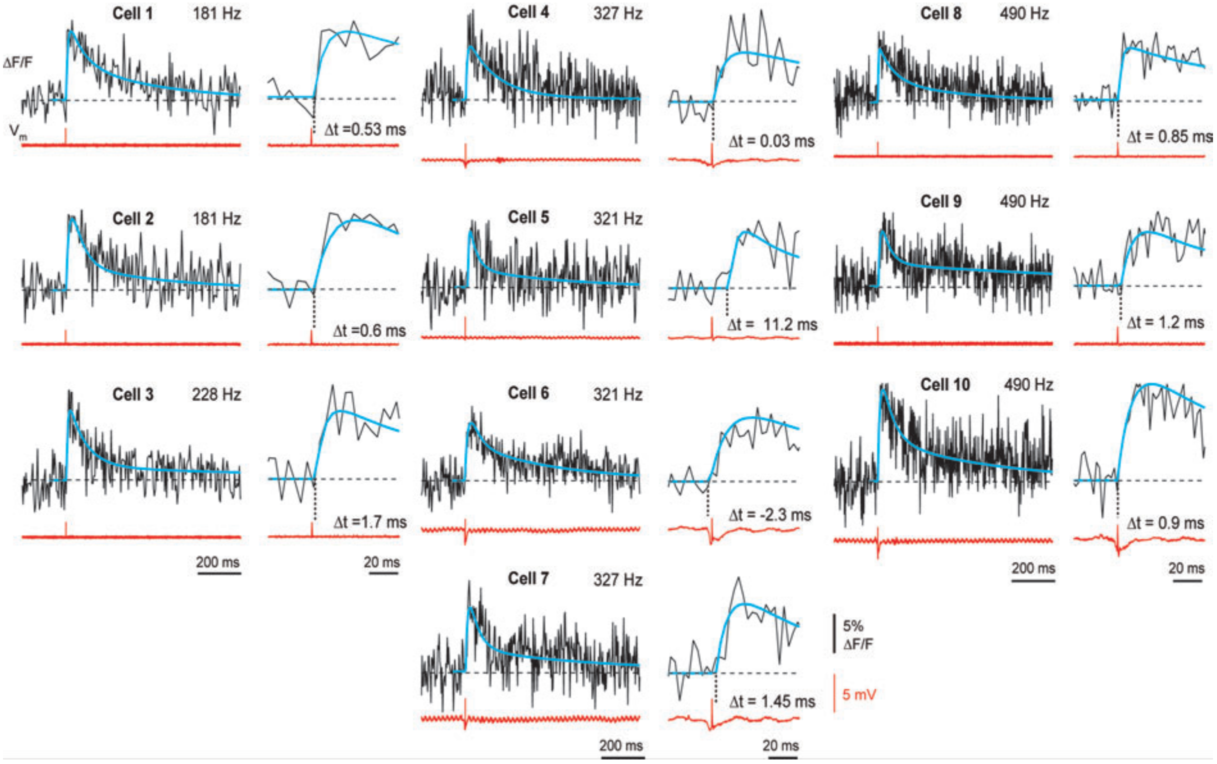

Figure 5.9: *Examples of 1AP-evoked fluorescence transients for all cells with combined electrical and optical recording. Unfiltered single-trial examples of 1AP-evoked calcium transients for each neuron from which a combined optical and electrical recording was made. Examples are grouped according to the cell sampling rate (left column: ≈ 200 Hz; middle: ≈ 325 Hz; right: 490 Hz). Juxtacellular voltage recordings (mV) are shown in red below the $\Delta F/F$ traces. Action potentials occurred spontaneously or were evoked by a brief air puff (Cells 4, 6, 7, 10). For each example a zoom-in on the calcium transient onset is shown on expanded time scale. Blue traces are the final curve fits to the calcium transients. Note that onset start and onset time constant were determined in a first separate fitting-step (not shown here) and held constant afterwards, while the final amplitude was determined from fitting the long decay. Time differences Δt between optical spike time estimates and the actual spike times are indicated.*

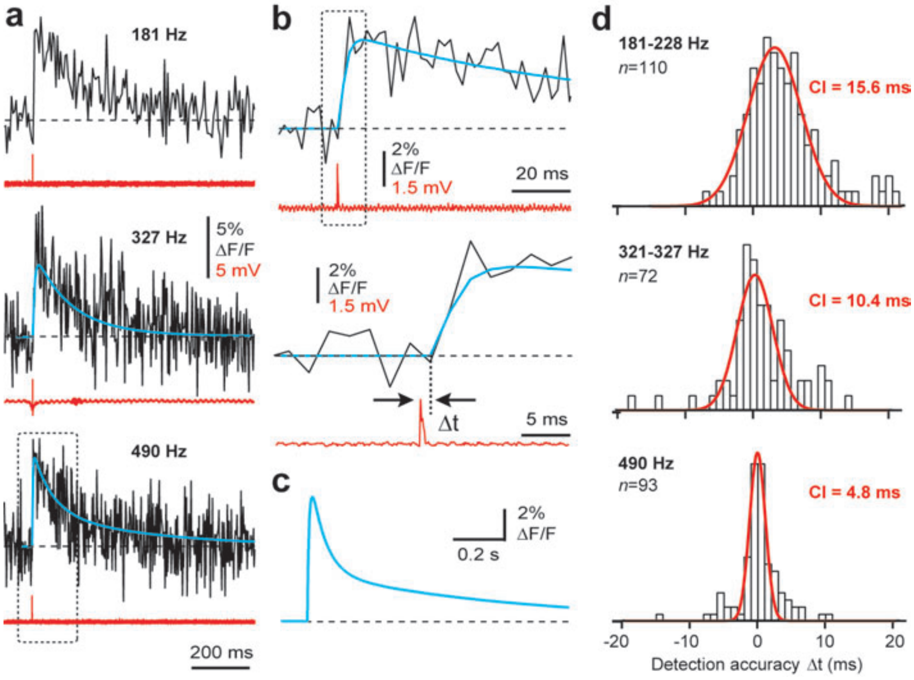

Figure 5.10: *Determining spike times from AOD-based optical recordings. (**a**) Examples of combined recordings of 1AP-evoked calcium transients for three different cells measured under three different conditions (top: 91 neurons sampled at 181 Hz; middle: 51 neurons at 327 Hz; bottom: 34 neurons at 490 Hz). Blue traces show curve fits to the calcium transients. Fluorescence traces are unfiltered raw data. (**b**) Upper panel: Close-up of the initial phase of the calcium transient measured at 490 Hz marked in (a) and the corresponding juxtacellular voltage recording. The onset of the unfiltered raw fluorescence trace was fit with a rising exponential and an exponential decay (blue trace). Lower panel: Zoom-in of the same calcium transient onset showing the time difference Δt between the spike time predicted from the onset fit and the actual spike time (0.85 ms in this case). (**c**) Average 1AP-evoked calcium transient fit pooled over all confirmed single AP-events independent of cell sampling rate (n=250). (**d**) Summary histograms of the distribution of time differences Δt measured using 5-point RAPS under the three different sampling conditions. CI values refer to 95%-confidence intervals obtained from Gaussian fits (red). n-values refer to the number of total events analyzed in each group.*

In the first step the onset was fitted to determine the start of the event and the onset time constant (Fig. 5.10b). Then the entire calcium transient was fitted to obtain estimates of amplitudes and time constants for the two decay components. Results were independent of cell sampling rate and thus pooled. Onset time constant was on average 8.1±0.5 *ms* (constrained to 2-30 *ms*, n=250 1AP-events; mean ± S.E.M.). Amplitudes (decay time constants) were 7.7±0.2% (56±3 *ms*) and 3.1±0.1% (777±80 *ms*) for the fast and slow component respectively. The average peak amplitude of the fitted calcium transients was 7.2±0.2%. Hence our analysis revealed a stereotypical 1AP-evoked calcium transient (Fig. 5.10c) that was used for subsequent analysis of spike trains.

Using the spike time estimate provided by the onset fit (Fig. 5.10b) we quantified how accurately spike times can be determined using RAPS. The time difference Δt between the estimated and the actual spike time on average was 4.7±0.6 ms, 1.1±0.6 ms, and 0.27±0.35 ms for 200 Hz, 325 Hz, and 490 Hz cell sampling rate respectively (mean±S.E.M; n=110, 72, and 93). The mean of the Δt distribution thus reports spike time with an accuracy on the order of the sampling interval or better. To quantify the uncertainty in this spike time estimate we constructed histograms of Δt for all sampling conditions and determined the width of these distributions from Gaussian fits. 95%-confidence intervals (± 2 S.D.) were 15.6, 10.4, and 4.8 ms for approx. 200 Hz, approx. 325 Hz, and 490 Hz cell sampling rate, respectively (Fig. 5.10d). The SNR for our recordings was defined as peak amplitude of the 1AP-evoked calcium transient divided by baseline noise. Baseline noise was low (S.D. 2.1±0.34%, see also Fig. 5.11) yielding SNR values between 2 to 5 (mean 3.5±0.06%).

We thus conclude that AOD-RAPS allows reliable detection of 1AP-evoked calcium transients. and reveals spike times with near-millisecond precision and confidence intervals of 5-15 ms.

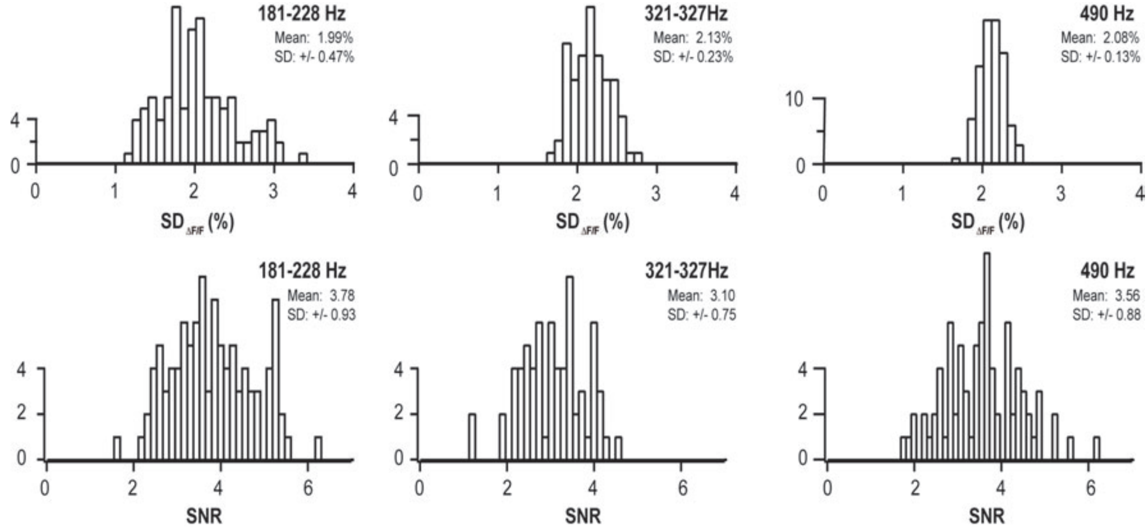

Figure 5.11: *Baseline noise of RAPS recordings.* ***Upper row****: histograms of* $\Delta F/F$ *noise levels (defined as S.D. of baseline) for the three cell sampling conditions. Note that the means of the histograms are very similar because effective dwell times per cell were identical.* ***Lower row****: histograms of SNR for the three cell sampling conditions. SNR was defined as the peak amplitude of the* $\Delta F/F$ *transient (derived from the model fit) divided by the baseline noise. Total n-numbers for both rows were 101, 67, and 82 from left to right.*

To evaluate the potential contamination of somatic fluorescence transients by neuropil signals [Göbel and Helmchen, 2007a] we performed 5-point RAPS recordings of air puff-evoked fluorescence transients from cell somata and simultaneously from the surrounding neuropil (Fig. 5.12).

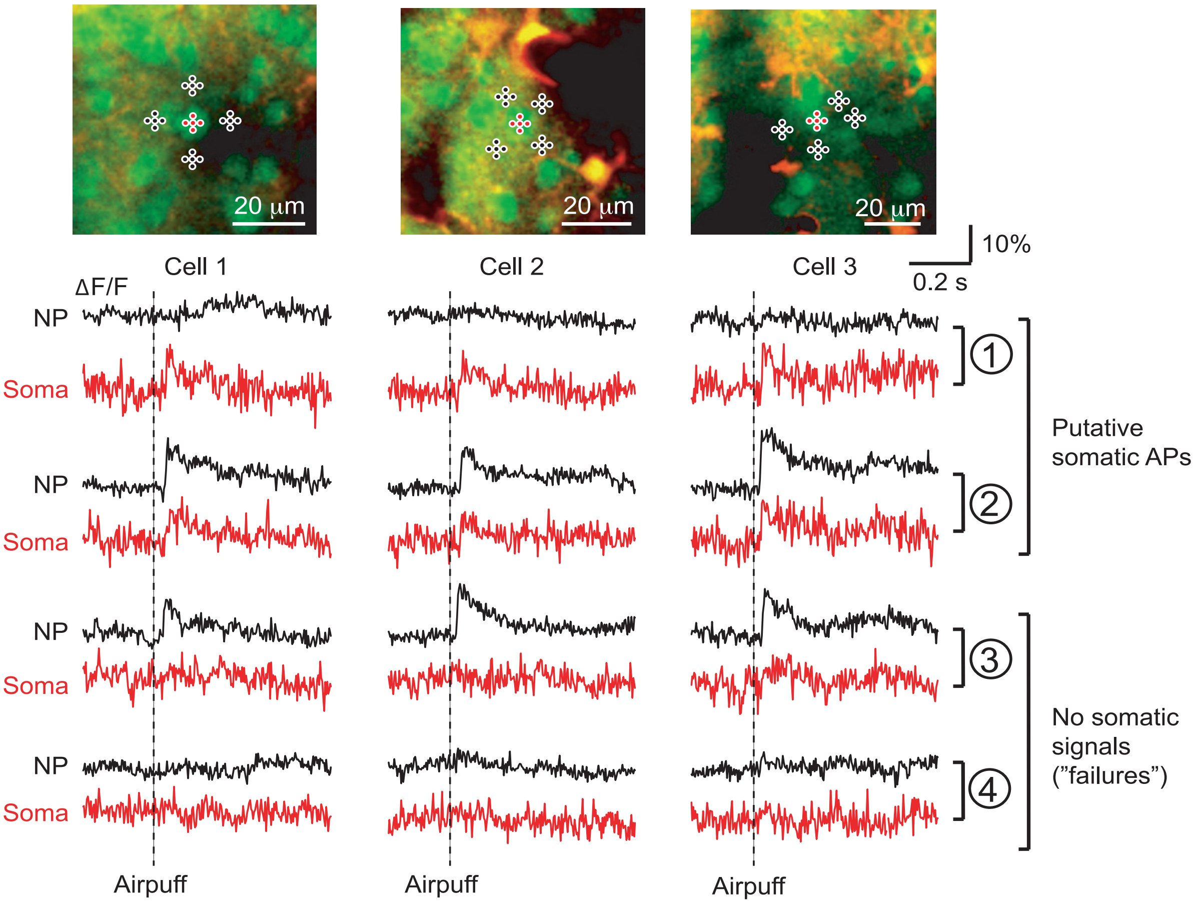

Figure 5.12: *Negligible neuropil (NP) contamination of sensory-evoked somatic fluorescence signals.* ***Top****: Three examples of 5-point RAPS recordings from cell somata and surrounding neuropil in mouse barrel cortex (depth ≈ 200 μm).* ***Bottom****: Example fluorescence traces from somata (red) and neuropil (black; averaged over four regions) upon stimulation with an air puff. All four possible cases of differential soma/neuropil activation were observed: (1) soma response/little neuropil signal, (2) soma response/strong neuropil signal, (3) apparent soma failure/strong neuropil signal, (4) apparent failures in both soma and neuropil.*

Somatic and neuropil signals occurred independent from each other showing all possible combinations of evoked signals and apparent failures. Notably somatic failures were apparent in cases of large activation of the surrounding neuropil indicating a rather small contamination by neuropil. This conclusion was further supported by analyzing failure events (AP failure, neuropil signal was evoked with air puff stimulation) that could be identified in our combined electrical and optical recording dataset. Averaging fluorescence traces for these failures revealed signals with 1.2±0.3% (mean±S.D.) amplitude that might represent small contamination by neuropil (Fig. 5.13). Because these events are typically buried within our noise levels and since their integral of the expected integral of a 1AP-evoked transient is far below 50% they will not be recognized or discarded by the peeling algorithm (see experimental methods section).

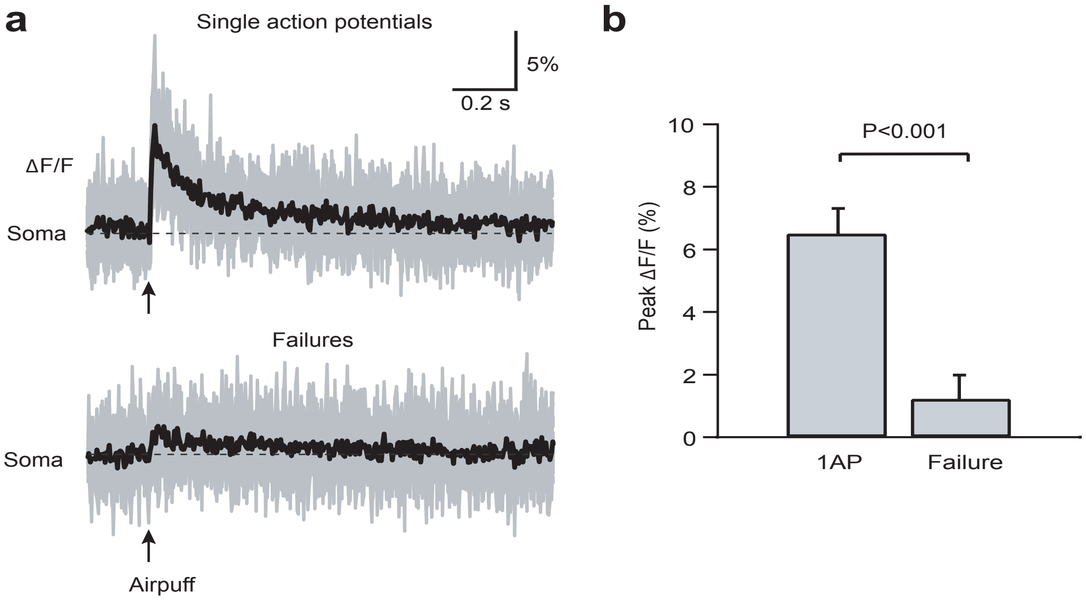

Figure 5.13: *Minor neuropil contamination of sensory-evoked somatic fluorescence signals. (**a**) Analysis of somatic fluorescence signals for failures identified in the juxtacellular recordings. Average somatic $\Delta F/F$ transients (black traces; individual trials are overlaid in grey) for 1AP events (top) and identified failures (bottom) for a recording at 228 Hz cell sampling rate ($n = 14$ traces; mean amplitudes 7.4% and 1.7% respectively). (**b**) Mean peak amplitudes of averaged somatic $\Delta F/F$ transients for 1AP events and failures for eight cells (6.5±0.3% vs. 1.2±0.3%; mean ± S.E.M.).*

5.5 Automated spike train reconstruction from fluorescence recordings.

Fluorescence calcium transients summate during higher-frequency spike trains (>1 Hz) because they last longer than APs. Reconstruction of spike trains from noisy fluorescence traces thus is a chief goal of *in vivo* calcium imaging experiments [Göbel and Helmchen, 2007a, Grewe and Helmchen, 2009]. In order to reconstruct complex spike trains we developed a generalized approach for automatically extracting spike times from arbitrary fluorescence traces. We assumed that each fluorescence trace represents the linear summation of 1AP-evoked calcium transients with a stereotypical waveform. This assumption is justified because the largest transients under our conditions (25-30% $\Delta F/F$) were little affected by dye saturation (see experimental methods section).

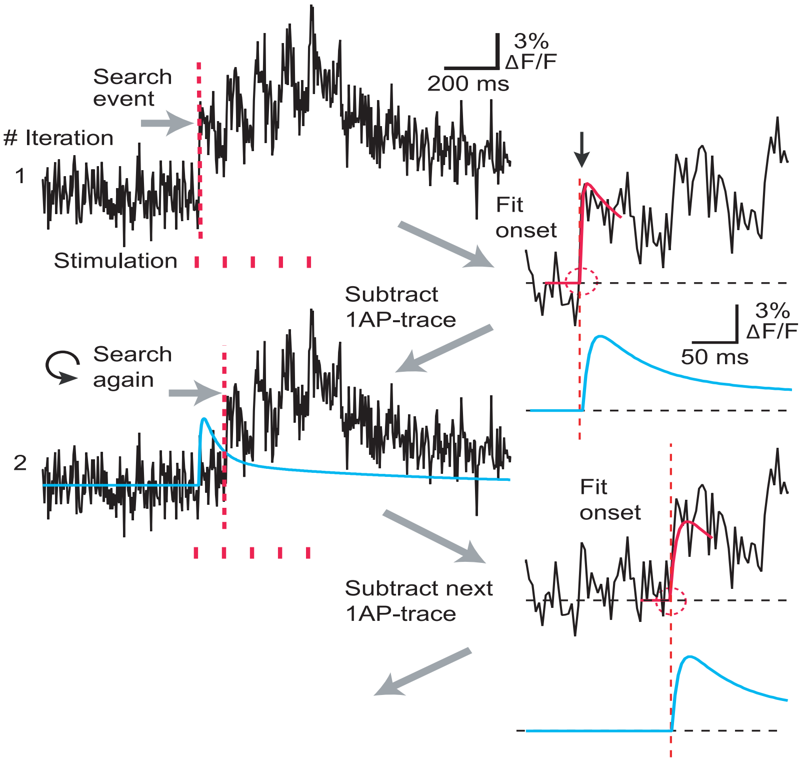

Figure 5.14: *Peeling algorithm for extracting spike trains from fluorescence transients. Step-by-step illustration of the automated peeling procedure. In the initial step a first "event" is detected using a customized Schmitt-trigger threshold routine. The onset of the detected calcium transient is fit within a short time window (red curve) in order to obtain a good estimate of the starting point of the event (red circle). Subsequently a stereotypical 1AP-evoked calcium transient is placed with its start at this time point and is subtracted from the original fluorescence trace. Then the algorithm starts the next iteration on the resulting difference trace.*

The principle of the algorithm is to iteratively subtract ('peel off') a 1AP-evoked calcium transient waveform at the detected event times from the fluorescence trace until a model trace of the superimposed calcium transients is reconstructed and a noisy residual trace remains (Fig. 5.14; Supplementary Movie 2). The main steps of this automated algorithm were (1) the event detection - to find the first event using the event detection algorithm, (2) the onset fit - to fit the onset in order to derive the timing of the first spike, and (3) to subtract the stereotypical 1AP-evoked calcium transient placed at this time point from the fluorescence trace (Fig. 5.14). These three steps are repeated until no further events are found in the residual fluorescence trace (Fig. 5.15; Supplementary Movie 2).

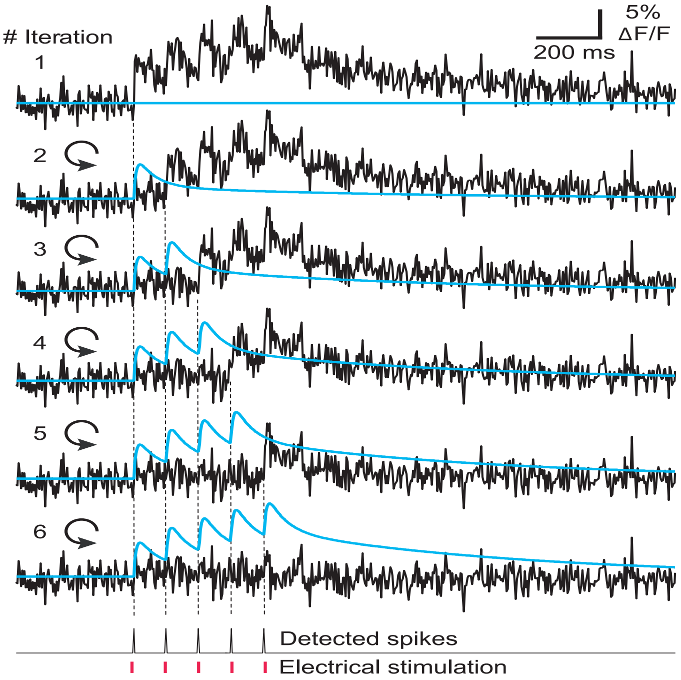

Figure 5.15: *Iterative extraction of spike trains from fluorescence transients. Example of the extraction of a train of five APs evoked by electrical stimulation at 10 Hz. For each iteration the residual fluorescence trace as well as the accumulated trace of all 1AP-evoked calcium transients so far extracted (blue trace) are depicted. After five iterations no further event is found in the residual fluorescence trace. At the bottom detected spike times are shown together with the stimulus times.*

Next we applied the peeling algorithm to investigate how well bursts of APs can be reconstructed from optical recordings using RAPS. To systematically induce spike trains in the 5-40 Hz frequency range we directly stimulated neuronal populations with short electrical pulses [Histed et al., 2009] through a patch-pipette positioned in L2/3 (Fig. 5.16a). Stimulus intensity was increased stepwise until a subpopulation of neurons reliably responded. At low frequencies individual calcium transients were clearly discernible while they became increasingly harder to discriminate at higher frequencies (Fig. 5.16b).

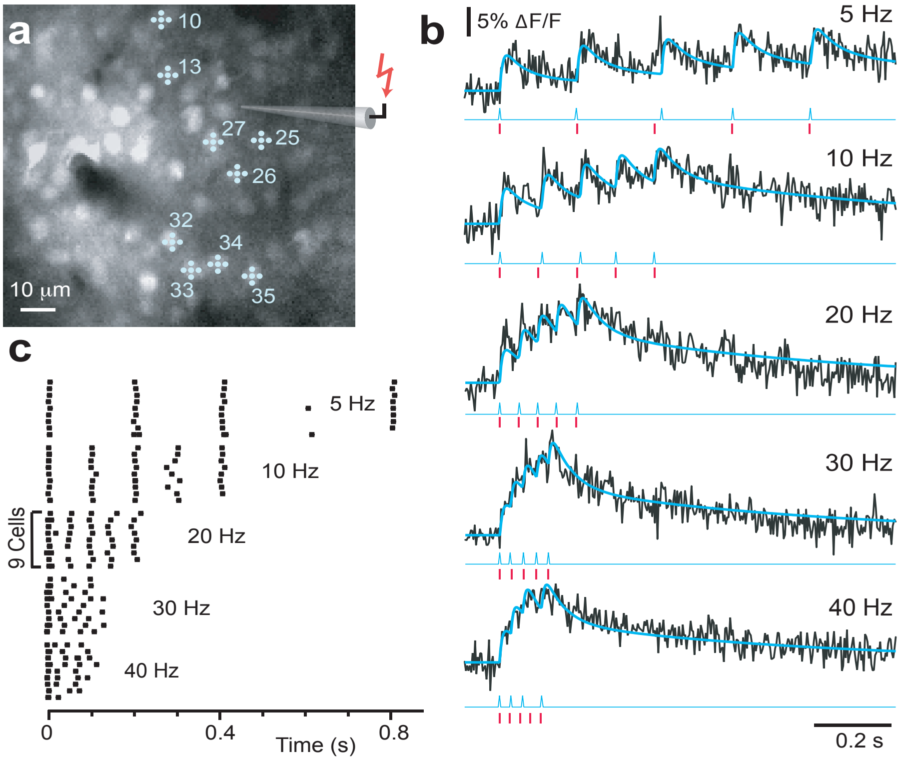

Figure 5.16: *Spike train reconstruction of lower frequent AP-bursts with different AP frequency. (**a**) Image of a L2/3 neuronal population in mouse barrel cortex labeled with OGB-1. Trains of five electrical stimuli at variable frequency were applied through a patch pipette placed in the extracellular space. In this example 9 out of 40 neurons sampled at 416 Hz with 5-point RAPS responded reliably to the electrical stimulation. (**b**) Example fluorescence transients for five stimulus frequencies between 5-40 Hz from a neuron in another experiment. Blue traces are the model traces reconstructed with the peeling algorithm. Extracted spike times (blue) are shown together with the stimulus times (red) below the traces. (**c**) Raster-plots of the spiking responses to stimulation at different frequencies for the nine neurons highlighted in (a). Raster plots were extracted using the peeling algorithm. The length of individual ticks reflects the confidence interval of spike detection from 1AP-evoked calcium transients.*

The largest fluorescence changes with 40 Hz stimulation were about 25-30% which was still much lower than saturating fluorescence changes under our conditions ($\Delta F/F_{max} = 93\%$; [Maravall et al., 2000]). For each trace we used the peeling algorithm to reconstruct a model trace of accumulated calcium transients and to extract a raster plot of the detected spike times. A summary raster plot for one experiment (Fig. 5.16c) as well as cumulative spike time histograms for five experiments (Fig. 5.17a, n=29 cells) indicate that the imposed burst frequency is well extracted up to 20 Hz while it cannot be clearly resolved at higher frequencies.

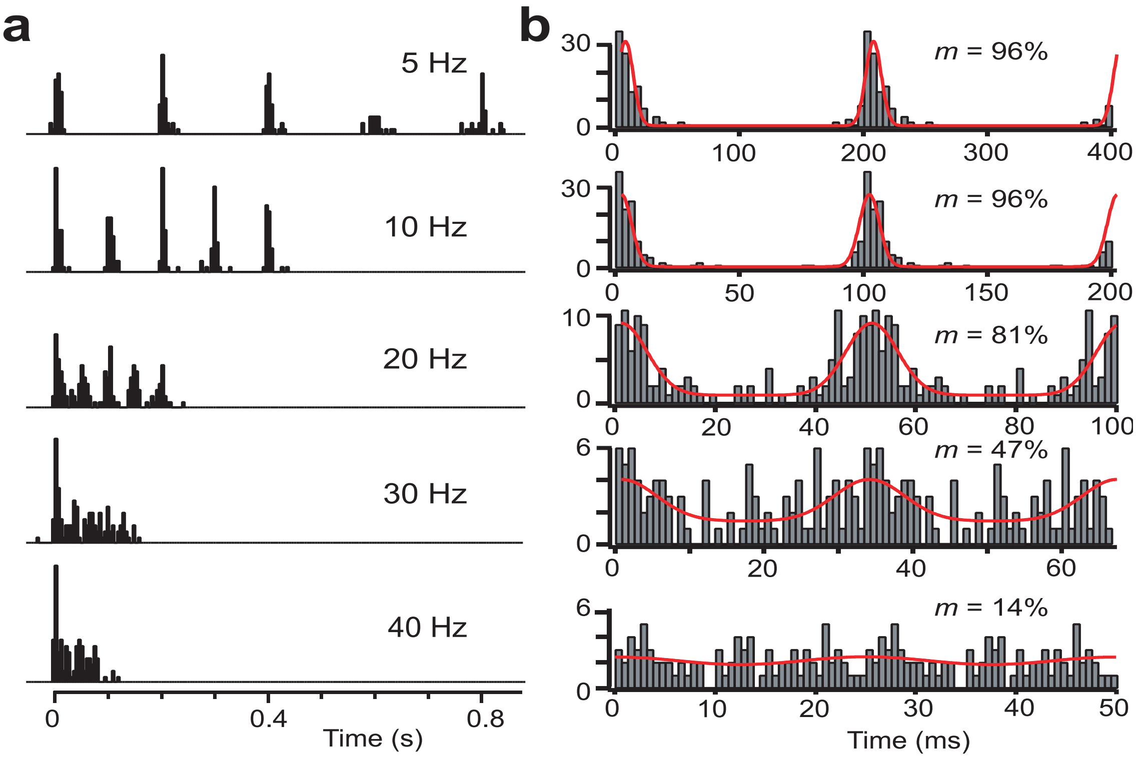

Figure 5.17: *Evaluation of spike train reconstruction of AP-bursts with different AP frequency. (**a**) Summary histograms of reconstructed spiking responses to stimulation at different frequencies (n=29 cells from three experiments, RAPS-rates 278-416 Hz). Note that the stimulus frequency is still apparent in the 20 Hz histogram. (**b**) Phase analysis of spiking responses to the burst stimulation. Spike times were recalculated modulo the duration of one stimulus cycle, and histograms were accumulated revealing the phase-relationship of detected spikes relative to the stimulus interval. For better visibility two cycles containing the same data sets are shown side by side. Red traces are curve fits with a Gaussian function revealing the peak amplitude* A_{max} *and the basal offset* A_{min}*. Values for the modulation calculated as* $m = (A_{max} - A_{min})/(A_{max} + A_{min})$ *are indicated.*

This finding was corroborated by an additional phase analysis in which histograms of the spiking phase within the stimulus cycles were generated for all spikes in the train (Fig. 5.17b). The widths of Gaussian fits to these phase histograms were on the order of 5 ms S.D., and the modulation was high (>80%) up to 20 Hz stimulus frequency, still 47% at 30 Hz, but lost at 40 Hz (Fig. 5.17b). We conclude that AOD-RAPS permits reconstruction of spike times for bursts of APs with frequencies up to 20 Hz and with confidence intervals on the order of 20 ms.

5.6 Spatiotemporal dynamics of sensory-evoked spiking activity

The combination of AOD-RAPS and peeling analysis should facilitate *in vivo* studies of various aspects of neural coding on a fast time scale. To directly demonstrate such potential applications we measured population spiking dynamics in primary sensory areas of the neocortex. First we recorded population response in mouse barrel cortex while repetitively stimulating the contralateral whiskers with a 5 Hz train of 5 air-puffs. The results of the recorded and reconstructed neuronal population activity are shown in Figure 5.18a.

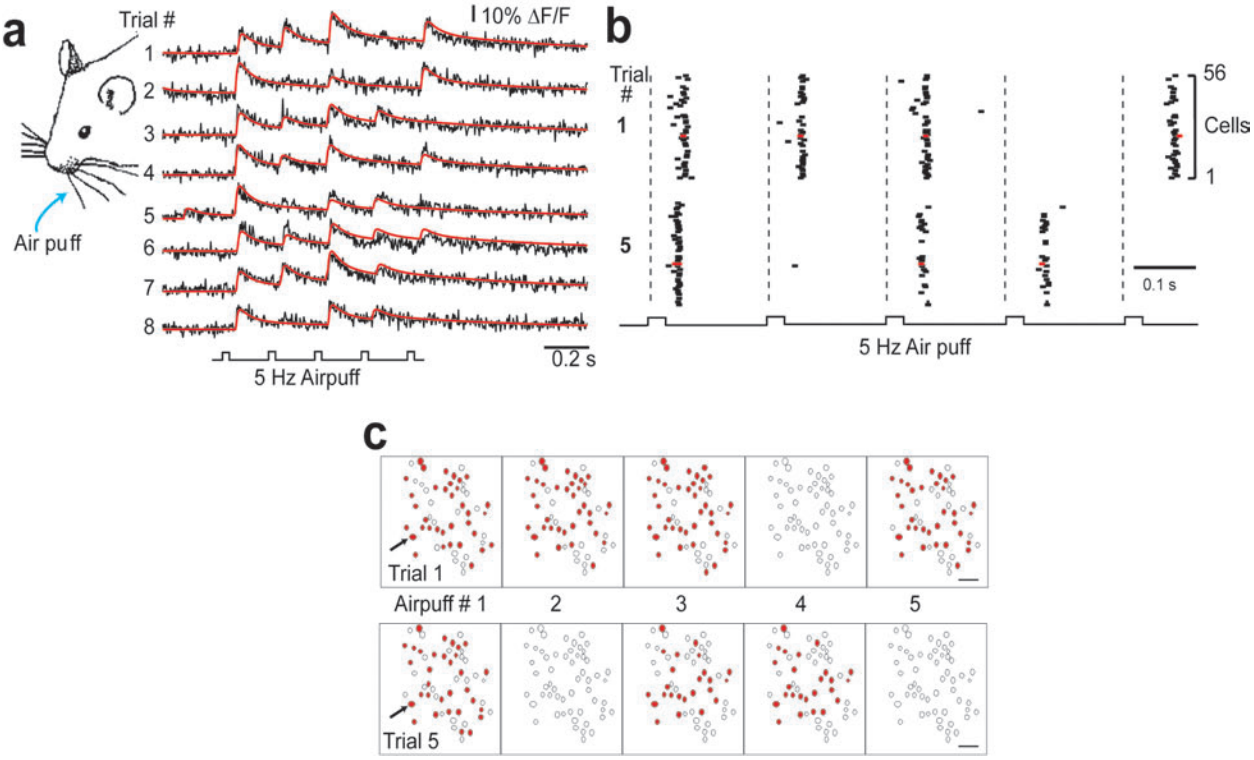

Figure 5.18: *Sub-second trial-to-trial variability of sensory-evoked responses in barrel cortex of mice. (**a**) Illustration of air-puff stimulation and example calcium transients in response to eight consecutive trials of 5 Hz trains of air-puffs in a L2/3 neuron of mouse barrel cortex (5-point RAPS at 298 Hz, 56 neurons sampled). Red traces are the model traces reconstructed by the peeling algorithm. Note that the peeling algorithm detected putative evoked doublets and triplets. (**b**) Raster-plots of the entire population (56 cells) for two selected trials. Vertical dashed lines indicate the onsets of the stimuli triggering the air puffs. Tick length reflects the confidence interval for spike reconstruction. Red ticks indicate spike times extracted for the neuron shown in (a). See also Figure 5.19 for all trial responses. (**c**) Snapshots of the sub-populations activated by the train of air-puffs for trial 1 and 5. All cells are outlined and activated cells are marked in red. Cells were considered active if they elicited at least one spike within a 50 ms time window following the end of the stimulus pulse. Arrows indicate the cell for which example traces are shown in (a).*

During these experiments our sampling rate for the complete population (56 neurons) was 298 *Hz* (5-point RAPS). After applying the peeling algorithm we could reconstruct the underlying spiking pattern as visualized in a spiking raster plot over time. (Fig. 5.18a red traces and Fig. 5.18b). This example demonstrates that acousto-optic 2-photon RAPS-imaging is able to record population activity of neuronal cell population at very high rates. Furthermore it enables to monitor the activity of each cell as well as it's position within the neuronal network organization. Combining these two informations allows to spatially visualize the cell population activity as shown in Figure 5.18c (see also supplementary movie 3).

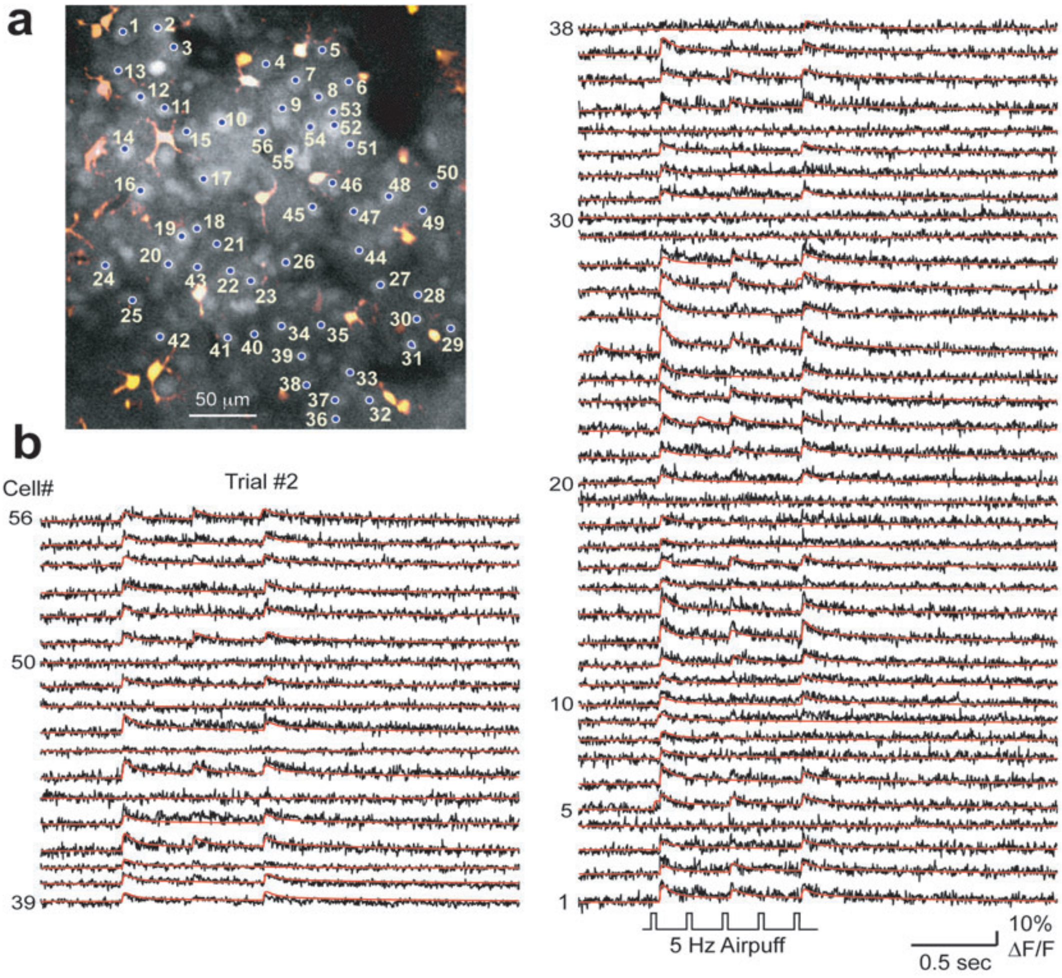

Figure 5.19: *Full dataset of whisker-evoked neuronal population response. (**a**) Image of an OGB-1 labeled population of 56 neurons in L2/3 of mouse barrel cortex measured at 298 Hz cell sampling rate with 5-point RAPS. Scale bar 50 μm. (**b**) Raw data of fluorescence transients in response to a single trial of 5 Hz whisker stimulation for all 56 L2/3 neurons (trial number 2). The model traces of calcium transients reconstructed with the peeling algorithm are overlaid in red.*

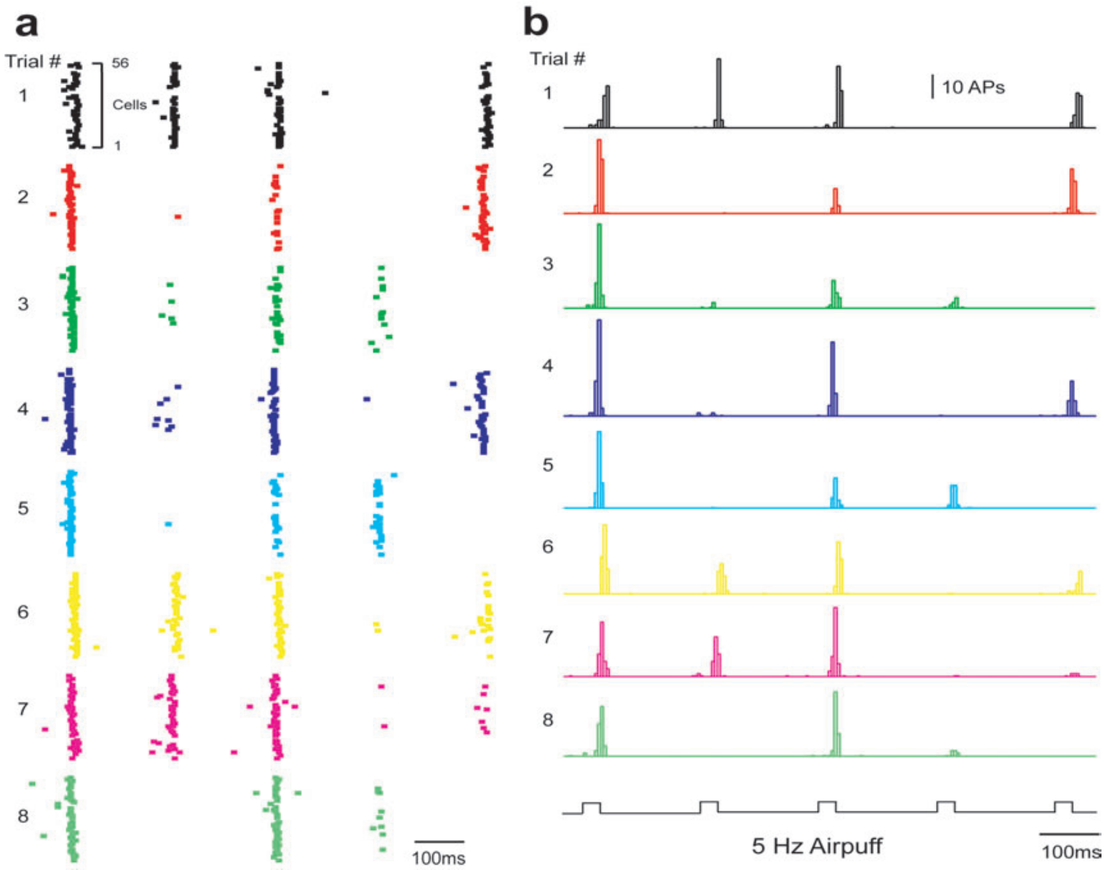

Figure 5.20: *Analysis of whisker-evoked neuronal population response. (**a**) Raster plot of the population spiking activity in response to eight subsequent trials of 5-Hz whisker stimulation. For each trial the onset times of the automatically detected calcium transients in all 56 cells are shown in a different color. Note failures of the entire population to respond. Tick lengths reflect the confidence interval of spike time reconstruction for the sampling condition (10.4 ms). (**b**) Peri-stimulus time histograms derived from the population response evaluated for the eight repeated whisker stimulation trials. Analysis of the latency distributions for the first stimulus revealed significant differences in the mean population latency between trials for temporal differences on the order of 10 ms (e.g. for Trial 1 and Trial 6 vs. all other trials the mean population latencies were 8.3 ± 2.3 ms and 9.5 ± 2.3 ms, respectively; $p<0.01$).*

Analyzing the neuronal spiking responses of eight subsequent trials of repeated whisker stimulation revealed that sensory-evoked responses in individual neurons as well as in the sampled population showed trial-to-trial variability with apparent failures to respond to particular stimuli during the air-puff trains (Fig. 5.18b and 5.20a). The cell sampling rate (298 Hz, CI 10.4 ms) was sufficient to resolve differences in global latency of population responses which were in the range of 10-20 ms. These differences in population response latency may have originated from distinct states of ongoing activity at the time of stimulation (Fig. 5.18b). As an example the population response to the first stimulus was significantly delayed in trial 1 compared to trial 5 (mean onset difference 9.1 ms; $p<0.001$). Notably the spatial dynamics of population activity within a few tens of milliseconds following individual air-puffs could be visualized in movies based on the automatically detected spike times and taking into account the confidence interval of spike time reconstruction (Fig. 5.18c and Supplementary Movie 3). As an example of a single trial response the complete population response of trial number 2 is shown Figure 5.19. In this example 56 neurons were measured with a sampling rate of 298 Hz. Sub sequentially their spiking activity was reconstructed offline (Fig. 5.19, red traces). Note: while some neurons do not responded during repeated whisker stimulation other neurons clearly showed 1, 2 or even more calcium transient responses with respect to the repeated air-puff stimulation.

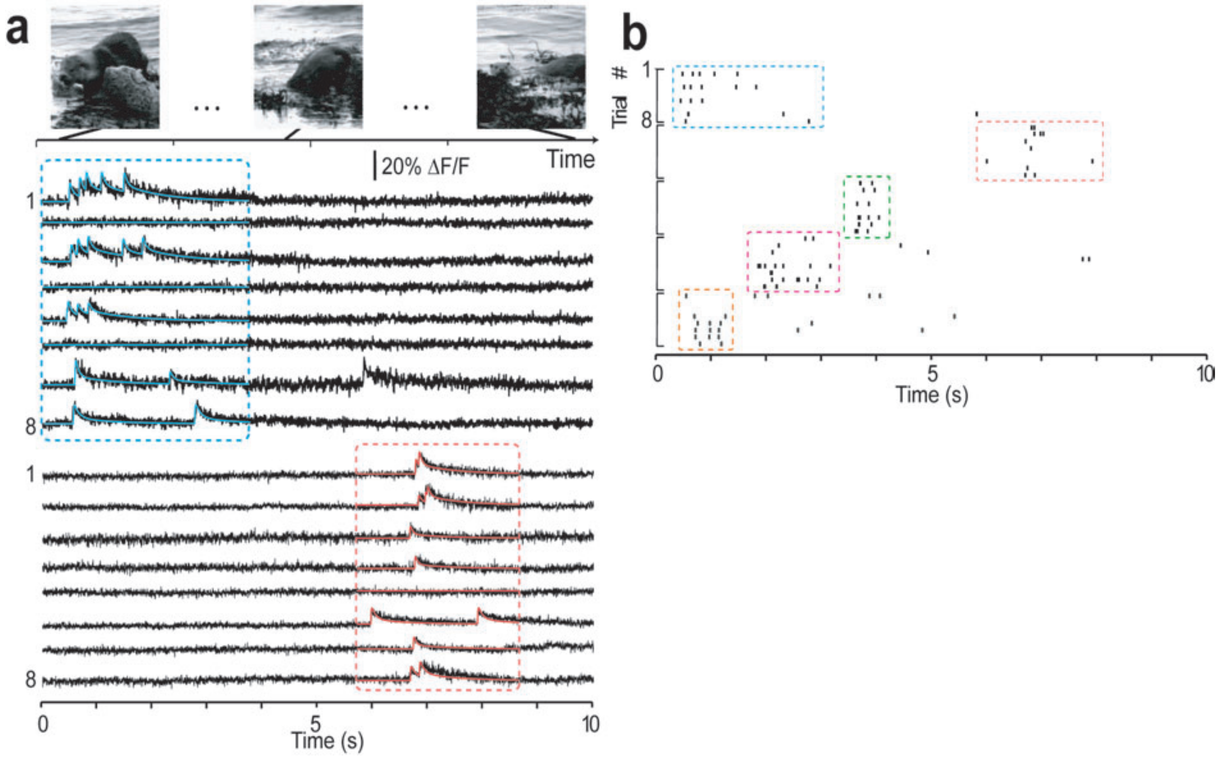

Figure 5.21: *Sub-second trial-to-trial variability of sensory-evoked responses in the visual cortex of mice. (**a**) Examples of visually-evoked calcium transients in mouse visual cortex. Upper row: Three chronological scenes from a 10 s natural movie that was repeatedly presented to the contra-lateral eye. Traces below are examples of fluorescence transients in two neurons evoked by eight consecutive presentations of the movie. Note the different movie periods during which the two cells respond. Cells are from two different experiments (5-point RAPS with cell sampling rate 278* Hz *and 309* Hz*). Response epochs for the two cells are indicated by a blue and red box respectively. Within the boxes overlaid colored traces are the model traces reconstructed by the peeling algorithm. (**b**) Raster-plots of reconstructed spiking responses to eight repeats of movie presentation for five neurons that showed reliable activation during specific epochs of the movie (indicated by boxes).*

In addition to the barrel cortex imaging experiments we measured spiking activity in mouse primary visual cortex in response to the presentation of a movie of 10 s duration. The movie was selected to be close to natural scenes that feature a natural contrast ratio and smooth movement of contrast borders. Presenting this natural movie during three imaging experiments to the mouse's contralateral eye we found several neurons in V1 that responded consistently during brief epochs (around 1-2 s duration) at particular time periods during the movie (Fig. 5.21a). In this case again the peeling algorithm allowed to extract spike raster plots that finally revealed within-epoch variability of spike numbers and spike timing (Fig. 5.21b). These results are in close agreement with electrophysiological findings that report similar neuronal activity within specific epochs of a presented movie [Goard and Dan, 2009].

In summary the new technique should facilitate investigations of basic neuronal network operation modes with respect to the visual cortical areas of rodents. This example together with the imaging experiments in the barrel cortex demonstrate that AOD-RAPS resolves spatiotemporal dynamics of sensory-evoked spiking activity in neocortical neural networks on the sub-second time scale.

5.7 Summary of results

In summary we could successfully demonstrate a novel, improved version of a 2-photon laser scanning microscope that employs acousto-optic scanners and allows high-speed measurements of neuronal network activity. Using an effective dispersion compensation unit we managed to balance out the dispersive effects that were caused by the AOD-scanners and succeeded to reshape the laser beam profile and the laser pulse length. Further microscope optimizations for maximum laser beam transmission resulted in a total transmission efficiency of about 25% (700 mW) below the objective. These optimizations together rendered our system suitable for *in vivo* imaging down to a depth of approximately 300 μm. The microscope resolution of 1-1.6 μm over the complete FOV thereby allowed a clear identification of cell somata. The maximum total scanning field of 305 μm x 305 μm contained up to 200 neurons, a subset of this population could be measured with sampling rates ranging from 100 Hz up to 1 kHz.

Employing random-access scanning with acousto-optic deflectors we were able to perform *in vivo* imaging of mouse neocortex with greatly improved temporal resolution and obtained fluorescence measurements from 34-91 layer 2/3 neurons at 180-490 Hz sampling rates. Most important the new scanning mode enabled us to detect single action potential-evoked fluorescence calcium transients with signal-to-noise ratios of 2-5. In addition high-speed RAPS imaging of neuronal somata allowed to determine neuronal spike times with a precision of a few milliseconds (5-15 ms). For analyzing bursts of action potentials we developed a new automated 'peeling' algorithm that made it possible to reconstruct more complex spike trains from fluorescence traces up to an AP-frequency of 20-30 Hz.

Demonstrating the potential of the new AOD-scanning technique we could resolve spatiotemporal trial-to-trial variability of sensory evoked neuronal spiking responses for cell populations in mouse barrel and visual cortex. By revealing spike sequences in neuronal populations on a fast time scale high-speed calcium imaging will facilitate optical studies of information processing in microcircuits of the brain.

6 Discussion

In summary we have overcome a major limitation of optical *in vivo* recordings from neuronal populations by demonstrating 2-photon imaging of neural networks in the intact brain with unprecedented temporal resolution. Compared to previous *in vivo* experiments employing galvanometer-based frame scanning at 1-30 Hz [Kerr et al., 2005, Ohki et al., 2005, Sato et al., 2007, Rochefort et al., 2009] our AOD-RAPS mode achieves cell sampling rates up to 1 kHz gaining a factor of 10-100 in temporal resolution. Previous AOD-based 2-photon microscopes have achieved similar scanning speed but they were mainly used for calcium imaging of neuronal dendrites in brain slices [Iyer et al., 2006, Otsu et al., 2008, Reddy et al., 2008]. In this project our aim was to design a relatively simple microscope that efficiently delivers short laser pulses to the intact brain and thus enables *in vivo* application. All main components are readily available, and beam path alignment is straightforward with the DCU-prism and the AODs as key adjustable components.

Alternatively fast cell sampling might be achievable by using fast resonant scanning mirrors that enable frame scan rates up to 30 Hz [Rochefort et al., 2009] or by using special galvanometric line scan techniques that allow recordings from a few neurons at Kilohertz rate. In this case the strategy to increase acquisition speed is again to restrict fluorescence excitation to the structures of interest and minimize background scanning. For instance standard laser scanning with galvanometric mirrors has been adapted to scan arbitrary free line scans on pre-selected subpopulations of cells [Göbel and Helmchen, 2007b, Nikolenko et al., 2007, Lillis et al., 2008]. In the extreme case galvanometers can be driven hard near their maximum acceleration to rapidly move the laser focus from one area to another remote area where it is slowed down again to scan a few cells [Lillis et al., 2008]. This approach, used in vitro so far, should be easily adaptable for *in vivo* measurements. However these techniques still waste too much scan time on background areas and lack the flexibility to scan arbitrary patterns; it is currently unclear whether they can provide sufficient SNR for measuring population activity *in vivo*.

Our AOD-RAPS mode extends previous random-access scanning modes [Iyer et al., 2006, Otsu et al., 2008]. By scanning a small point pattern on each individual neuron we achieved a high SNR while minimizing photobleaching and photodamage. In this context we could demonstrate that the acquired fluorescence signal even increased when distributing the scanning time to a point pattern that was scanned on cell somata (the total signal integration time was kept constant). Furthermore the OCIM gained the acquired signal (compared to normal point integration), depending on the cell integration time by a factor from 2-6. Applying this new scanning mode resulted in an SNR of about 3.5 for 1AP-evoked

AOD-imaging study	random-access imaging	3D-imaging	laser pulse length	application for *in vivo* imaging
[Goldstein et al., 1990]	x	x	1 photon	x
[Bullen et al., 1997]	x	x	1 photon	x
[Lechleiter et al., 2002]	x	x	200 fs	x
[Salome et al., 2005]	✓	x	110 fs	*not shown*
[Iyer et al., 2006]	✓	x	500-700 fs	x
[Vucinic and Sejnowski, 2007]	∼	✓	310 fs	*not shown*
[Kremer et al., 2008]	*not shown*	x	90-200 fs	*not shown*
[Reddy et al., 2008]	✓	✓	1800 fs	x
[Kirkby et al., 2010]	✓	✓	115 fs	*not shown*
[Grewe et al., 2010]	✓	x	140 fs	✓

Table 6.1: *Summary table of previous and recently published AOD-imaging studies that used customized AOD-imaging systems for fast imaging*

calcium transients which enabled us to detect spikes with high reliability (>95%) and with near-millisecond precision. Our ability to simultaneously attain high SNR and high cell sampling rates is explained by the fact that the effective dwell times per cell are similar to those of slower frame scanning systems [Sato et al., 2007, Rochefort et al., 2009, Kerr et al., 2007, Kerr et al., 2005, Greenberg et al., 2008]. The high temporal resolution was particularly beneficial for characterizing 1AP-evoked calcium transients in detail. We confirmed peak amplitudes of 7-8% for 1AP-evoked somatic calcium transients [Rochefort et al., 2009, Kerr et al., 2005] but also found that their decay typically consisted of a fast and a slow component. The initial fast component (<100 ms) might be undersampled with low-speed systems which could partially explain difficulties to detect single APs.

Various methods have been explored for inferring spike trains from calcium indicator fluorescence measurements including deconvolution techniques [Yaksi and Friedrich, 2006], template matching [Sato et al., 2007, Kerr et al., 2007], model based fitting [Greenberg et al., 2008], and sequential Monte Carlo methods [Vogelstein et al., 2009]. Here we introduced an iterative peeling algorithm which we successfully employed to extract spike trains under various conditions. The analysis of AP-bursts indicates that the peeling algorithm is capable of resolving spike times for spikes spaced as close as 40-50 ms apart. The peeling algorithm is generally applicable and computationally simple. In its simplest version described here the algorithm assumes a stereotype calcium transient and neglects dye saturation which indeed had little effect on the observed fluorescence transients (Fig. 4.1). Various extensions are possible; for example different 1AP-transient waveforms are likely to apply for different cell types, and for large calcium changes the reduction in $\Delta F/F$ amplitude with increasing dye saturation could be incorporated. While the *in vivo* measurements presented here were restricted to 2D our approach should be extendable to 3D using either mechanical z-scanning [Göbel and Helmchen, 2007a] or chirped acoustic waves in a series of AODs [Vucinic and Sejnowski, 2007, Reddy et al., 2008].

6.1 Technical and methodological discussion

During the past decade most studies made use of metal, glass or silicon electrodes to electrically record neuronal signals which allows a direct measurement of neuronal activity with a very good signal-to-noise ratio. The main strength of the method is that direct electrical measurements do not need a signal 'reporter' that transforms electrical activity into an optical fluorescent signal; the main weakness of electrophysiology is however that electrical access to the nervous system necessitates physical contact with the tissue. Other difficulties especially when investigating neuronal network population activity with electrodes is their lack to sample inactive or silent neurons and the difficulty to distinguish individual neuronal units by using simple spike sorting algorithms.

On the other hand improved optical techniques to measure neuronal network function offer numerous additional and crucial advantages such as an outstanding spatial resolution which allows to resolve signals even in the smallest neuronal structures [Ji et al., 2008, Hell, 2007]. Furthermore optical techniques allow simultaneous measurements from a wide range of spatially distributed locations or neurons within a neuronal network [Ji et al., 2008, Winship and Murphy, 2008], and with the recently introduced genetically encoded probes they enable simultaneous excitation of specific cellular subtypes and neuronal network domains [Zhang et al., 2007]. To investigate neuronal modes of operation via 2-photon imaging a functional dye is required that indirectly reports neuronal activity by changing its quantum efficiency. In combination with new microscopy tools these functional dyes have been used for a wide range of discoveries about the neuronal network function. These discoveries include the spatial organization of cortical maps on the level of individual neighbouring neurons [Kerr et al., 2007] and the functional map topography in the visual [Kara and Boyd, 2009, Rochefort et al., 2009, Greenberg et al., 2008] and the auditory system [Rothschild et al., 2010]. However in contrast to the advantages of the 2-photon imaging method there are still some challenges which will need further methodological improvements.

The future challenges are:

1. Imaging deeper cortical layers. While it has been shown that in principle imaging depths of about 1 mm can be realized by using a special 2-photon laser in combination with a bright staining [Theer and Denk, 2006] this imaging-depth decreases to several hundreds of microns (typically 300-400 μm) when functional dyes are used [Stosiek et al., 2003]. This depth limitation was also consistent with maximum imaging depth in this study (≈ 300 μm, see Fig. 6.1). Because layer 4 (the main input layer of the cortex) and layer 5 (the main output layer) play a substantial role regarding to the integration of incoming signals and the signal output processing, it would be of further interest to extend imaging to this deeper regions of the neocortex. The maximum imaging depth could be increased when using longer wavelengths for the excitation of fluorescent dyes.

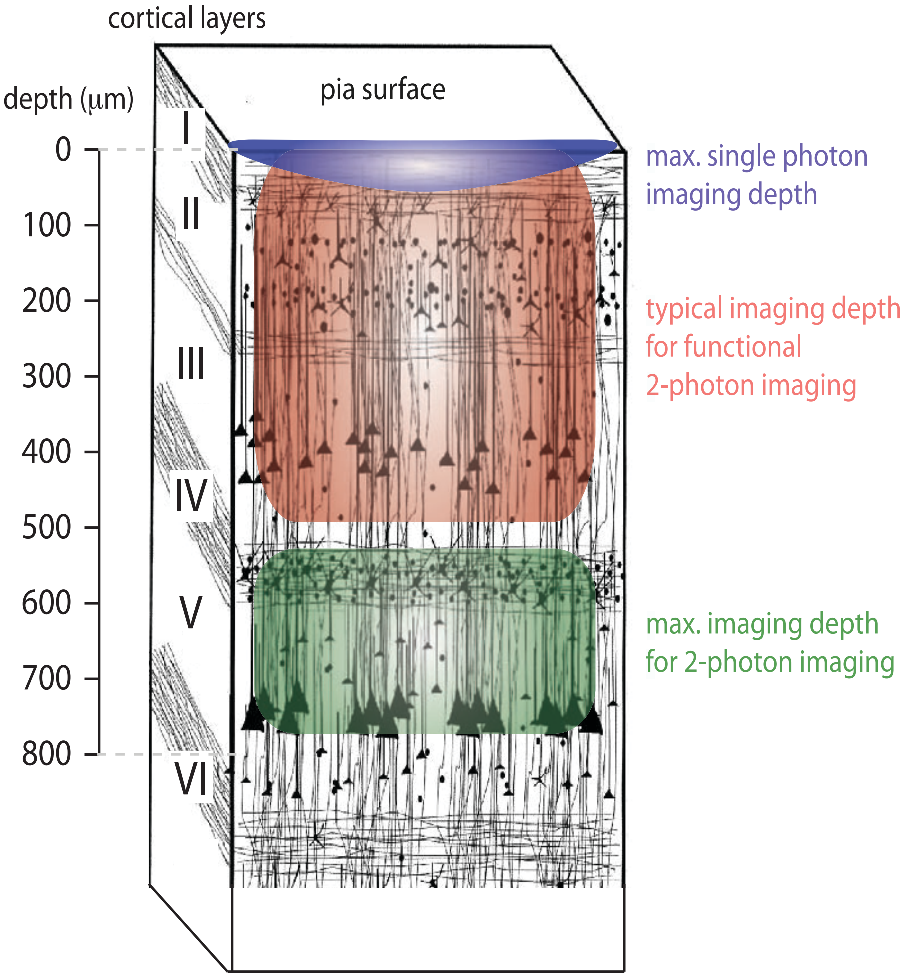

Figure 6.1: *Schematic drawings showing normal cortex with regularly distributed layers and related cells and fibers schematized for a mouse brain. The maximal available imaging depths are accordingly marked for single photon imaging (blue) 2-photon imaging (green) that uses bright genetical dyes such as GFP (green fluorescent protein) to visualize neuronal cell morphologies. Modified from [Bentivoglio* et al.*, 2003]*

Because standard 2-photon imaging studies in mice and rats are normally restricted to the cortical layers 1 and 2/3, an alternative approach to image deeper cortical layers is to insert a 90° reflective prism into the cortex to image the cortical layers from the side (Fig. 6.2). Although this approach is rather invasive it allows 2-photon imaging of neurons that are located in the deeper cortical layers 4 & 5, it would be compatible with the new high-speed AOD-imaging technique. Another possibility to measure deeper cortical layers would be to change to a smaller species of interest (e.g. etruscan shrew, personal communication M. Brecht, Humbold University, Berlin).

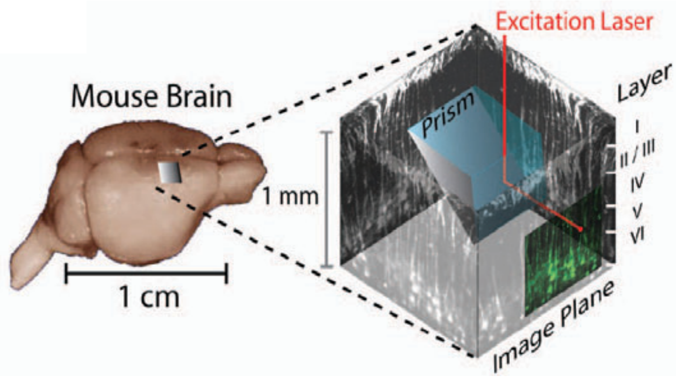

Figure 6.2: *A micro-prism for deep in vivo imaging. Illustration depicting the placement of the micro-prism into the neocortex of a mouse and the resulting translation of the excitation laser for so called side-on imaging. Modified from [Chia and Levene, 2009]*

.

2. Imaging of large neuronal ensembles in three dimensions. For specific investigations fast comprehensive measurements in 3D are be required to obtain a complete picture of local network interaction dynamics on a single-trial basis. Therefore another goal is to expand high-speed neuronal population sampling to three dimensions. Using reproducible stimuli relatively slow signals can be reconstructed throughout a volume from sequential recordings at different focal depths [Yaksi et al., 2007, Yaksi et al., 2009, Ohki et al., 2006, Kirkby et al., 2010]. On the other hand adding a third scan dimension exacerbates the difficulties of imaging large populations with high temporal resolution. Recently a novel mechanical 3D scanning approach that combines x/y-scan mirrors with a piezoelectric z-focusing device was introduced [Gobel et al., 2007]. Custom 3D line scan modes enabled *in vivo* calcium measurements from several hundred neurons at 10 Hz sampling rate within a cubic volume of about 250 μm side length (Fig. 6.3a). Even though mechanical scanning is limited by the inertia of the movable components video-rate recordings seem possible for small volumes. Addition of an extra imaging stage, leaving the front objective stationary and shifting z-scanning to a small lightweight mirror in the intermediate optical path [Botcherby et al., 2008], might facilitate even faster volume scanning (Fig. 6.3b). However we suggest that an improved and efficient dispersion compensation that balances out spatial and temporal pulse broadening and a sufficient laser beam transmission throughout the scan optics in combination with a piezoelectric z-scanner should make 3D (2D+1D) AOD imaging suitable for *in vivo* applications in the near future (Fig. 6.3a).

Another promising alternative are special arrangements of multiple AODs that allow high-speed inertia-free 3D scanning [Reddy et al., 2008, Vucinic and Sejnowski, 2007] (Fig. 6.3c). The basic idea is to apply chirped acoustic waves to the AODs to control beam divergence in addition to deflection angle which results in a movement of the excitation spot along the z-axis. This approach enables random-access scanning in a circumscribed volume but is limited to octahedron-shaped volumes [Reddy et al., 2008].

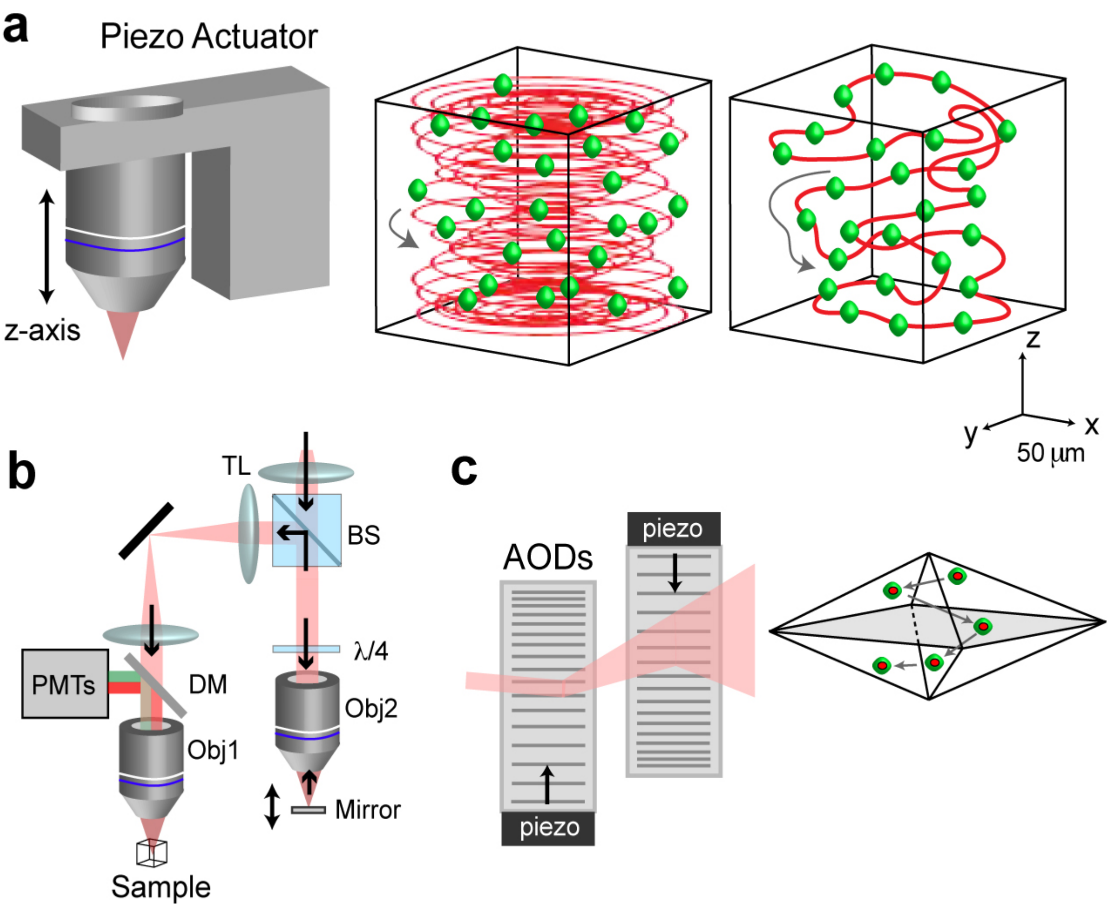

Figure 6.3: *3D laser scanning approaches. (**a**) Mechanical 3D scanning. A piezoelectric focusing element allows sinusoidal movements of the objective along the optical axis (z-axis) with a travel range of up to 400 µm at 10 Hz rate or higher. Right panels show two options for 3D line scanning of the laser focus, one based on opening and closing spiral patterns in the x-/y-plane (middle), the other realizing a user-defined 3D trajectory through pre-selected cells within a volume [Göbel* et al.*, 2007]. (**b**) New method of remote focusing according to [Botcherby* et al.*, 2008]. An extra aberration-free imaging stage is added to achieve z-focusing by displacement of a small mirror below objective 2. This arrangement should allow for higher z-scanning rates while mechanical interference between the objective 1 and the specimen is avoided because this objective remains stationary. With 2-photon excitation fluorescence photons can be collected with photomultipliers (PMTs) positioned close to objective 1. The quarter-waveplate is used to turn the beam polarization on return by 90°. BS, polarizing beam splitter; DM, dichroic mirror; TL, tube lens. (**c**) 3D random-access scanning with AODs. Counter-propagating chirped acoustic waves in a pair of AODs control angular deflection and laser beam divergence which translates to an axial shift of the focus (one-dimensional case shown). With two such pairs of AODs oriented orthogonally 3D random-access scanning is possible within an octahedron-shaped volume (right).*

3. Imaging in awake, behaving animals. Because neuronal ensemble activity can be substantially suppressed in anesthetized animals, it is desirable for future experiments to perform population calcium imaging in awake, behaving animals. A strategy that employs a standard 2-photon microscope setup and its advantages is to immobilize the animal or at least its head and keep the microscope stationary. Utilizing this head fixation approach behavior-related calcium signals in neurons and glial cells could be imaged in awake behaving mice [Dombeck et al., 2007, Nimmerjahn et al., 2009] (Figure 6.4). The major advantage of the head-fixed approach is that the microscope can be optimized for *in vivo* imaging (adjusted for best resolution and fluorescence signal detection). On the other hand extracting spike patterns from calcium measurements is particularly challenging for awake recordings because motion artifacts can distort cellular signals. Especially laser scanning leads to complicated artifacts because pixel values are separated in space and time so that image distortions can not be reversed off-line by simple geometric transformations. The chief goal therefore is to mechanically stabilize the tissue using agarorse or transparent rubber pieces, at least minimizing focal plane changes [Dombeck et al., 2007]. Remaining lateral movements then can be corrected offline using for example a Hidden-Markov model [Dombeck et al., 2007] or a Lucas-Kanade image registration algorithm [Greenberg and Kerr, 2009]. Because random-access AOD-imaging at multiple selected sites would not allow a post hoc motion correction, we additionally aim to develop a fully automated online adjustment of scan signals within a closed loop to counteract the motion induced artifacts and thus stabilize the optical recordings. Despite the difficulties such as motion artifacts, time-consuming habituation of animals, and reduced behavioral repertoires the head fixed approach (Fig. 6.4) has the potential to become a widespread method in the near future.

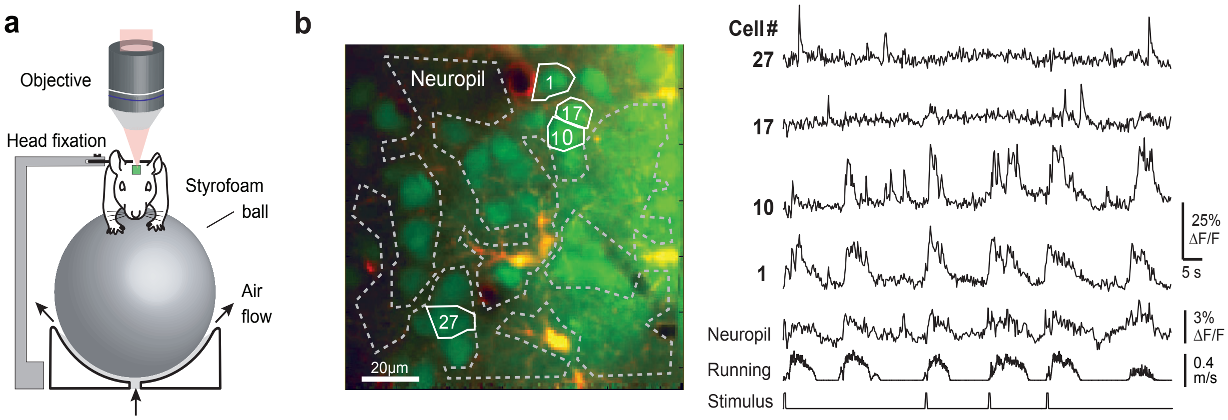

Figure 6.4: *2-photon calcium imaging with cellular resolution in awake animals.* ***(a)*** *Schematic setup for imaging in a head-restraint mouse which moves on an air-supported styrofoam ball.* ***(b)*** *Cell population in sensory cortex labeled with Calcium Green-1 (left). Adapted from [Dombeck* et al.*, 2007]. Neurons (green) were negative for the astrocytic marker SR101 (yellow). Fluorescence traces for the neuropil and 4 out of 34 neurons after off-line motion correction (right). Running speed and air puff stimuli are also shown.*

4. Fully automated spike reconstruction. Whereas fast measurement techniques rapidly emerge, tools to fully analyze network dynamics of calcium imaging data still necessitate further development. The reconstruction of spike trains from fluorescence recordings is basically a deconvolution of the noisy imaging data, thereby presuming elementary calcium transients. Although individual spikes in principle are detectable [Kerr et al., 2005, Kerr et al., 2007, Greenberg et al., 2008, Sato et al., 2007, Wallace et al., 2008, Sasaki et al., 2008], noise levels vary considerably depending on indicator dye, imaging speed, pixel dwell time, and other factors. Therefore the ability to detect single-spikes has to be verified for each experimental setup. Any improvements in SNR for example through enhanced fluorescence collection [Engelbrecht et al., 2009] will facilitate more reliable spike detection. In this context another remaining issue will be a detailed evaluation of spike reconstruction algorithms that have been reported by different studies [Dombeck et al., 2007, Greenberg et al., 2008]. Here we introduced a sufficient spike peeling algorithm that allows an accurate and reliable reconstruction of underlying spiking activity from the optical fluorescence recordings [Grewe et al., 2010]. Because for this study all measurements have been performed using the RAPS imaging mode at very high sampling rates it will be particularly interesting to evaluate the spike detection reliability and accuracy for lower sampling rates and different SNRs, e.g. during conventional frame scanning.

5. Imaging of neuronal ensembles that express a genetically encoded calcium reporter. A major advantage of genetically encoded calcium dyes is the possibility to perform repeated imaging experiments of the same neuronal cell population over days, weeks or even months [Hendel et al., 2008, Ashworth and Brennan, 2005, Heim et al., 2007]. Employing these dyes could be especially interesting for studies that investigate in neuronal network plasticity or pathological developments on a long term base. The common basis of all genetically encoded dyes is a calcium sensitive protein that, after translating the cell membrane, is expressed into the cell cytosol (Fig. 6.5 and Fig. 6.6a).

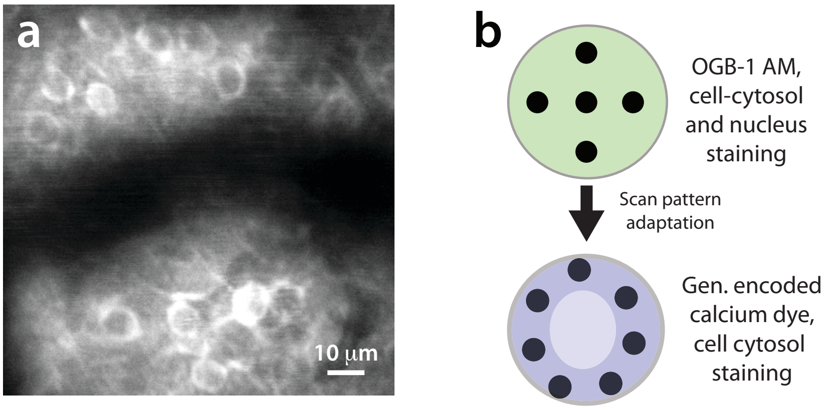

Figure 6.5: *(**a**) 2-photon in vivo image of a neuronal cell population that expresses the genetically encoded calcium dye Yellow Chameleon in the cell's cytosol. (**b**) Possible adaptation of the standard 5-point RAPS pattern to fit the fluorescent structure of interest; this adaptation may help to increase the quality of the acquired fluorescence signal.*

Similar to synthetic calcium dyes also genetically encoded dyes change their fluorescence signal intensity (increase or decrease or both) during the calcium-bound state (see Fig. 6.6b). Nevertheless all synthetic and also the genetically encoded calcium dyes feature individual signaling kinetics and offer different signal intensities as well as SNRs which necessitates a proper evaluation. In this case a further adaptation of the random-access scanning pattern to the structure of interest can help to improve the SNR (Fig. 6.5b). In particular this adaptation may help when recording from neurons that express a genetic encoded calcium reporter only within the cytosol excluding the cell nucleus.

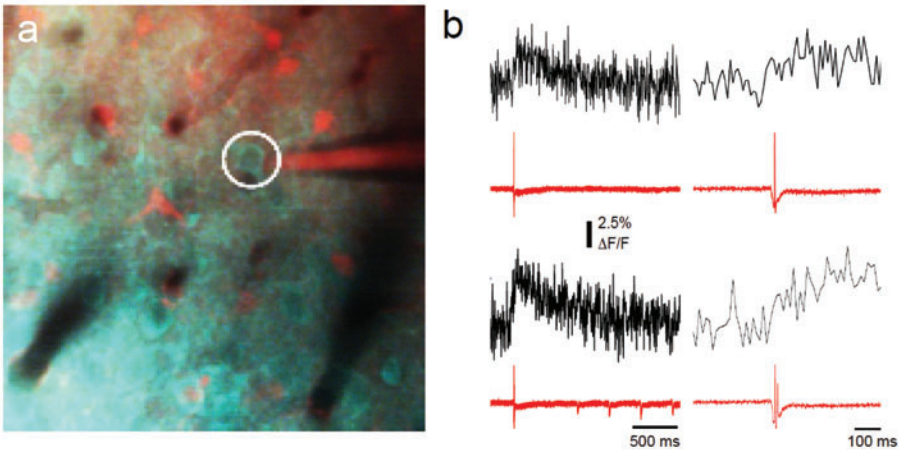

Figure 6.6: *RAPS imaging of neuronal cell populations that express genetically encoded calcium dyes.(**a**) 2-photon in vivo image of a neuronal cell population in mouse barrel cortex that expresses the genetically encoded calcium dye Yellow Chameleon with patch pipette (red) for simultaneous cell attached electric recordings. (**b**) Simultaneous fluorescence measurement and electrical recording of the neuron marked in (a). This neuron was one out of 31 neurons sampled at 386 Hz using 9-point RAPS. Calcium transients were evoked stimulating the contralateral whiskers by short air-puffs.*

6.2 Outlook

High-speed measurements could be especially beneficial for analyzing spike sequences in specific neuronal subsets following slower screening of large populations for relevant subensembles. Retrograde labeling techniques and transgenic mice with fluorescent protein expression could be particularly helpful for guiding measurements to specific cell types. Moreover the combination of genetically-encoded calcium indicators [Wallace et al., 2008, Tian et al., 2009, Mank et al., 2008, Lütcke et al., 2010] with high-speed calcium imaging opens new opportunities for repeated long-term functional interrogation of neuronal networks.

The advances of acousto-optic 2-photon microscopy create new opportunities for the investigation of neuronal ensembles *in vivo*. Experience-dependent reconfiguration of neural networks is thought to be a central mechanism of learning and plasticity. With the novel, fast scanning method now one can dissect functional changes in neuronal circuits during development or following plasticity-inducing protocols. For example in mouse visual cortex the fraction of neurons contributing to spontaneous activity was found to decrease during postnatal development [Rochefort et al., 2009]; in ferrets early training with moving stimuli directly after eye opening accelerated the emergence of direction-selective cells in the visual cortex [Li et al., 2008], and monocular deprivations in mice caused changes of eye-specific responsiveness in neuronal populations [Mrsic-Flogel et al., 2007]. Microscopes with improved imaging speed will enable studies of plasticity effects that depend on millisecond-precise relative timing of neural spikes. Optical studies of network reconfiguration are likely to expand as soon as repeated functional imaging of the same network becomes routinely possible and may be achieved by long-term expression of genetically expressed calcium indicators (GECIs) using transgenic approaches [Hendel et al., 2008, Ashworth and Brennan, 2005, Heim et al., 2007], viral delivery [Wallace et al., 2008, Lütcke et al., 2010], or by in utero electroporation [Mank et al., 2008]. A first study demonstrated chronic imaging of the same neurons in mouse cortex over days and weeks ([Mank et al., 2008, Andermann et al., 2010, Lütcke et al., 2010] and personal communication Henry H. Lütcke and David Margolis, Brain Research Institute, Zürich, Switzerland).

In addition a number of studies have started to use *in vivo* population calcium imaging for investigating network dysfunctions in mouse models of brain diseases. In a special example that followed an ischemic damage in somatosensory cortex the limb selectivity of calcium signals in individual neurons was reduced in the beginning while at later stages responses became more selective for a preferred limb [Winship and Murphy, 2008]. A 2-photon calcium imaging study on Alzheimer's mice reported a redistribution of spontaneous neuronal activity which found that hyperactive neurons were appearing exclusively in the vicinity of amyloid plaques [Busche et al., 2008]. Similarly pathological effects on glial cells have been investigated in disease models [Takano et al., 2007, Kuchibhotla et al., 2009]. Especially studies that are based on the analysis of fast neuronal network activity patterns will be facilitated by the use of novel high-speed imaging techniques such as the AOD-scanning method. We think that s detailed analysis of such neuronal activity patterns will at the end also help to provide novel insights into the alterations of neural network dynamics that are prevalent in various brain diseases.

In detail the combination of fast optical recording and automated spike train reconstruction will facilitate studies of various important aspects of neural coding. First, a better characterization of bursting behavior of cortical neurons which appears to be enhanced in awake animals [de Kock and Sakmann, 2009, Greenberg et al., 2008] should be possible. With respect to future investigation in neuronal bursting behavior the novel AOD-microscope should allow to resolve the number of APs within a burst very reliably while accurately determing inter-spike frequencies of up to 20-30 Hz. Second, phase-relationship studies of AP firing with respect to global neuronal oscillations such as hippocampal 4-10 Hz theta-oscillations [Hartwich et al., 2009] should be feasible. By reconstruction the AP-output of individual neurons of the population while simultaneously recording the electric field potential it should be feasible to analyze and correlate the individual neuronal firing patterns to these oscillation cycles. Third, high-speed imaging should enable detailed analysis of the variability of absolute (within a cell) and relative (between cells) spike timing thereby addressing the question of temporal versus rate coding [Kostal et al., 2007]. By analyzing the activity pattern of extended neuronal populations ($n_{cell} = 50 - 100$) high-speed imaging allows to investigate temporal correlations of population spiking activity to find out if information processing is rather 'temporal' or 'rate' encoded. Finally, recording a few neurons at highest speed (0.5-1 kHz) may allow optical investigation of network plasticity that is likely to be ruled by relative spike timing differences on the order of a few tens of milliseconds [Kampa et al., 2007, Caporale and Dan, 2008]. In this case fast RAPS imaging should help resolving short latencies of some milliseconds between spiking activity of individual neurons to analyze their temporal correlation and to reveal the underlying connection scheme between these cells.

Further adaptations of the AOD microscope that allow to directly correct online for motion induced artifacts will render high-speed RAPS-imaging suitable to be applied in awake, behaving animals. We thus think that AOD-RAPS *in vivo* imaging is likely to become a versatile technique for studying fundamental principles of fast neural information processing in microcircuits of the brain.

6.3 Final conclusions

In summary we think that emerging optical techniques are revolutionizing the study of neural dynamics on the mesoscopic scale, bridging the gap between the cellular level and the level of communicating brain areas. Although this dissertation extensively reports a new and innovative high-speed 2-photon scanning technique it can cover only a few aspects of current developments focusing on the rapidly advancing field of *in vivo* calcium imaging of neuronal populations. In parallel the complementary field of optical control of neural circuits using light-activated ion channels is developing at similarly rapid pace [Zhang et al., 2007]. Moreover novel techniques for high resolution anatomical reconstructions of large tissue volumes promise to reveal detailed wiring diagrams of neural microcircuits [Helmstaedter et al., 2008, Lichtman and Sanes, 2008]. With these developments coming together it no longer seems unrealistic to directly observe (and manipulate) neuronal ensemble dynamics in behaving animals and to relate it to the underlying wiring scheme. This powerful convergence of matching methods no doubt will help to uncover fundamental principles of network dynamics in the brain.

Bibliography

[Andermann et al., 2010] Andermann, M., Kerlin, A. and Reid, R. (2010). Chronic cellular imaging of mouse visual cortex during operant behavior and passive viewing. Front of Cellular Neuroscience *12*, 3.

[Ashworth and Brennan, 2005] Ashworth, R. and Brennan, C. (2005). Use of transgenic zebrafish reporter lines to study calcium signaling in development. Brief Funct Genomic Proteomic *4*, 186–193.

[Bentivoglio et al., 2003] Bentivoglio, M., Tassi, L., Pech, E., Costa, C., Fabene, P. and Spreafico, R. (2003). Cortical development and focal cortical dysplasia. Eleptic Diorders *5*, 27–34.

[Berger et al., 2007] Berger, T., Borgdorff, A., Crochet, S., Neubauer, F., Lefort, S., Fauvet, B., Ferezou, I., Carleton, A., Luescher, H. and Petersen, C. (2007). Combined voltage and calcium epifluorescence imaging in vitro and in vivo reveals subthreshold and suprathreshold dynamics of mouse barrel cortex. J Neurophysiol *97*, 3751–62.

[Berridge et al., 2003] Berridge, M., Bootman, M. and Roderick, H. (2003). Calcium signalling: dynamics, homeostasis and remodelling. Nat Rev Mol Cell Biol *4*, 517–529.

[Bollmann and Engert, 2009] Bollmann, J. and Engert, F. (2009). Subcellular topography of visually driven dendritic activity in the vertebrate visual system. Neuron *61*, 895–905.

[Borst and Helmchen, 1998] Borst, J. and Helmchen, F. (1998). Calcium influx during an action potential. Methods Enzymol *293*, 352–371.

[Botcherby et al., 2008] Botcherby, E., Juskaitis, R., Booth, M. and Wilson, T. (2008). An optical technique for remote focusing in microscopy. Opt Comm *281*, 880–887.

[Broca, 1861] Broca, M. (1861). Remarques sur le siege de la faculte du langage articule, suivies d'une observation d'aphemie (Perte de la Parole). Bulletins et Memoires de la Societe Anatomique de Paris *36*, 330–357.

[Brodmann, 1909] Brodmann, K. (1909). Vergleichende Lokalisationslehre der Grosshirnrinde in ihren Principien dargestellt auf Grund des Zellenbaues., vol. 2,. Johann Ambrosius Barth Verlag, Heidelberg.

[Bullen et al., 1997] Bullen, A., Patel, S. and Saggau, P. (1997). High-speed, random-access fluorescence microscopy. I. High-resolution optical recording with voltage-sensitive dyes and ion indicators. Biophys J *73*, 477–491.

[Buonomano and Maass, 2009] Buonomano, D. and Maass, W. (2009). State-dependent computations: spatiotemporal processing in cortical networks. Nat Rev Neurosci *10*, 113–125.

[Busche et al., 2008] Busche, M., Eichhoff, G., Adelsberger, H., Abramowski, D., Wiederhold, K., Haass, C., Staufenbiel, M., Konnerth, A. and Garaschuk, O. (2008). Clusters of hyperactive neurons near amyloid plaques in a mouse model of Alzheimer's disease. Science *321*, 1686–1689.

[Caporale and Dan, 2008] Caporale, N. and Dan, Y. (2008). Spike timing-dependent plasticity: a Hebbian learning rule. Annu Rev Neurosci *31*, 25–46.

[Chia and Levene, 2009] Chia, T. and Levene, M. (2009). Microprisms for In Vivo Multilayer Cortical Imaging. J of Neurophys *102*, 1310–1314.

[Churchland et al., 2007] Churchland, M., Yu, B., Sahani, M. and Shenoy, K. (2007). Techniques for extracting single-trial activity patterns from large-scale neural recordings. Curr Opin Neurobiol *17*, 609–618.

[Churchland and Sejnowski, 1992] Churchland, P. and Sejnowski, T. (1992). The Computational Brain. MIT Press, Cambridge.

[de Kock and Sakmann, 2009] de Kock, C. and Sakmann, B. (2009). Spiking in primary somatosensory cortex during natural whisking in awake head-restrained rats is cell-type specific. Proc Natl Acad Sci USA *106*, 16446–16450.

[Denk et al., 1990] Denk, W., Strickler, J. and Webb, W. (1990). Two-photon laser scanning fluorescence microscopy. Science *248*, 73–6.

[Diels et al., 1985] Diels, J., Fontaine, J., McMichael, I. and Simoni, F. (1985). Control and measurement of ultrashort pulse shapes (in amplitude and phase) with femtosecond accuracy. App Opt *24*, 1270–1282.

[Dombeck et al., 2007] Dombeck, D., Khabbaz, A., Collman, F. and Tank, D. (2007). Imaging large scale neural activity with cellular resolution in awake mobile mice. Neuron *56*, 43–57.

[Douglas et al., 1995] Douglas, R., Koch, C., Mahowald, M., Martin, K. and Suarez, H. (1995). Recurrent excitation in neocortical circuits. Science *269*, 981–5.

[Douglas and Martin, 2004] Douglas, R. and Martin, K. (2004). Neuronal circuits of the neocortex. Annu Rev Neurosci *27*, 419–51.

[Engelbrecht et al., 2009] Engelbrecht, C., Göbel, W. and Helmchen, F. (2009). Enhanced fluorescence signal in nonlinear microscopy through supplementary fiber-optic light collection. Opt Express *17*, 6421–6435.

[Engelbrecht et al., 2008] Engelbrecht, C., Johnston, R., Seibel, E. and Helmchen, F. (2008). Ultra-compact fiber-optic two-photon microscope for functional fluorescence imaging in vivo. Opt Express *16*, 5556–5564.

[Flusberg et al., 2008] Flusberg, B., Nimmerjahn, A., Cocker, E., Mukamel, E., Barretto, R., Ko, T., Burns, L., Jung, J. and Schnitzer, M. (2008). High-speed, miniaturized fluorescence microscopy in freely moving mice. Nat Methods *5*, 935–938.

[Fork et al., 1984] Fork, R., Martinez, O. and Gordon, J. (1984). Negative dispersion using pairs of prisms. Optics Letters *9*, 150–152.

[Garaschuk et al., 2006a] Garaschuk, O., Milos, R., Grienberger, C., Marandi, N., Adelsberger, H. and Konnerth, A. (2006a). Optical monitoring of brain function in vivo: from neurons to networks. Pfluegers Arch *453*, 385–396.

[Garaschuk et al., 2006b] Garaschuk, O., Milos, R. and Konnerth, A. (2006b). Targeted bulk-loading of fluorescent indicators for two-photon brain imaging in vivo. Nat Protoc *1*, 380–386.

[Goard and Dan, 2009] Goard, M. and Dan, Y. (2009). Basal forebrain activation enhances cortical coding of natural scenes. Nat Neurosci *12*, 1444–1449.

[Göbel and Helmchen, 2007a] Göbel, W. and Helmchen, F. (2007a). In vivo calcium imaging of neural network function. Physiology (Bethesda) *22*, 358–365.

[Göbel and Helmchen, 2007b] Göbel, W. and Helmchen, F. (2007b). New angles on neuronal dendrites in vivo. J Neurophysiol *98*, 3770–3779.

[Göbel et al., 2007] Göbel, W., Kampa, B. and Helmchen, F. (2007). Imaging cellular network dynamics in three dimensions using fast 3D laser scanning. Nat Methods *4*, 73–79.

[Goldstein et al., 1990] Goldstein, S., Hubin, T., Rosenthal, S. and Washburn, C. (1990). A confocal video-rate laser-beam scanning reflected-light microscope with no moving parts. J Microsc *157*, 29–38.

[Göppert-Mayer, 1931] Göppert-Mayer, M. (1931). Über Elementarakte mit zwei Quantensprüngen. Annalen der Physik *PhD-thesis, University of Göttingen.*

[Goutzoulis and Pape, 1994] Goutzoulis, A. and Pape, D., eds (1994). Design and Fabrication of Acousto-optic Devices. Marcel Decker Inc., New York, 270 Madison Avenue, New York.

[Greenberg et al., 2008] Greenberg, D., Houweling, A. and Kerr, J. (2008). Population imaging of ongoing neuronal activity in the visual cortex of awake rats. Nat Neurosci *11*, 749–751.

[Greenberg and Kerr, 2009] Greenberg, D. and Kerr, J. (2009). Automated correction of fast motion artifacts for two-photon imaging of awake animals. J Neurosci Methods *176*, 1–15.

[Grewe et al., 2010] Grewe, B., Bonan, A. and Frick, A. (2010). Back-propagation of physiological action potential output in dendrites of slender-tufted L5A pyramidal neurons. Front of Cellular Neuroscience *4*, doi:10.3389/fncel.2010.00013.

[Grewe and Helmchen, 2009] Grewe, B. and Helmchen, F. (2009). Optical probing of neuronal ensemble activity. Curr. Opin. Neurobiol *19*, 520–529.

[Grewe et al., 2010] Grewe, B., Langer, D., Kasper, H., Kampa, B. and Helmchen, F. (2010). High-speed in vivo calcium imaging reveals spike trains in neuronal networks with near-millisecond precision. Nat Methods *7*, 399–405.

[Grillner et al., 2005] Grillner, S., Markram, H., Schutter, E. D., Silberberg, G. and LeBeau, F. (2005). Microcircuits in action - from CPGs to neocortex. Trends Neurosci *28*, 525–33.

[Hartwich et al., 2009] Hartwich, K., Pollak, T. and Klausberger, T. (2009). Distinct firing patterns of identified basket and dendrite-targeting interneurons in the prefrontal cortex during hippocampal theta and local spindle oscillations. J Neurosci *29*, 9563–9574.

[Hausser et al., 2000] Hausser, M., Spruston, N. and Stuart, G. (2000). Diversity and dynamics of dendritic signaling. Science *290*, 739–744.

[Heim et al., 2007] Heim, N., Garaschuk, O., Friedrich, M., Mank, M., Milos, R., Kovalchuk, Y., Konnerth, A. and Griesbeck, O. (2007). Improved calcium imaging in transgenic mice expressing a troponin C-based biosensor. Nat Methods *4*, 127–129.

[Hell, 2007] Hell, S. (2007). Far-field optical nanoscopy. Science *316*, 1153–1158.

[Helmchen and Denk, 2005] Helmchen, F. and Denk, W. (2005). Deep tissue two-photon microscopy. Nat Methods *2*, 932–940.

[Helmchen et al., 1996] Helmchen, F., Imoto, K. and Sakmann, B. (1996). Ca^{2+} buffering and action potential-evoked Ca^{2+} signaling in dendrites of pyramidal neurons. Biophys J *70*, 1069–1081.

[Helmstaedter et al., 2008] Helmstaedter, M., Briggman, K. and Denk, W. (2008). 3D structural imaging of the brain with photons and electrons. Curr Opin Neurobiol *18*, 633–641.

[Hendel et al., 2008] Hendel, T., Mank, M., Schnell, B., Griesbeck, O., Borst, A. and Reiff, D. (2008). Fluorescence changes of genetic calcium indicators and OGB-1 correlated with neural activity and calcium in vivo and in vitro. J Neurosci *28*, 7399–7411.

[Histed et al., 2009] Histed, M., Bonin, V. and Reid, R. (2009). Direct activation of sparse, distributed populations of cortical neurons by electrical microstimulation. Neuron *63*, 508–522.

[Holekamp et al., 2008] Holekamp, T., Turaga, D. and Holy, T. (2008). Fast three-dimensional fluorescence imaging of activity in neural populations by objective-coupled planar illumination microscopy. Neuron *57*, 661–672.

[Iyer et al., 2006] Iyer, V., Hoogland, T. and Saggau, P. (2006). Fast functional imaging of single neurons using random-access multiphoton (RAMP) microscopy. J Neurophysiol *95*, 535–545.

[Ji et al., 2008] Ji, N., Shroff, H., Zhong, H. and Betzig, E. (2008). Advances in the speed and resolution of light microscopy. Curr Opin Neurobiol *18*, 605–616.

[Jia et al., 2010] Jia, H., Rochefort, N., X, X. C. and Konnerth, A. (2010). Dendritic organization of sensory input to cortical neurons in vivo. Nature *464*, 1307–12.

[Kaiser and Garret, 1961] Kaiser, W. and Garret, C. (1961). Two-photon excitation in $CaF_2:Eu^{2+}$. Physical Review Letters *7*, 229.

[Kampa et al., 2007] Kampa, B., Letzkus, J. and Stuart, G. (2007). Dendritic mechanisms controlling spike-timing-dependent synaptic plasticity. Trends Neurosci *30*, 456–463.

[Kandel et al., 2000] Kandel, E., Schwartz, J. and Jessel, T. (2000). Principles of Neural Science. McGraw-Hill Professional, New York.

[Kantevari et al., 2010] Kantevari, S., Matsuzaki, M., Kanemoto, Y., Kasai, H. and Ellis-Davies, G. (2010). Two-color, two-photon uncaging of glutamate and GABA. Nat Methods *7*, 123–5.

[Kara and Boyd, 2009] Kara, P. and Boyd, J. (2009). A micro-architecture for binocular disparity and ocular dominance in visual cortex. Nature *458*, 627–631.

[Kerr et al., 2007] Kerr, J., de Kock, C., Greenberg, D., Bruno, R., Sakmann, B. and Helmchen, F. (2007). Spatial organization of neuronal population responses in layer 2/3 of rat barrel cortex. J Neurosci *27*, 13316–13328.

[Kerr and Denk, 2008] Kerr, J. and Denk, W. (2008). Imaging in vivo: watching the brain in action. Nat Rev Neurosci *9*, 195–205.

[Kerr et al., 2005] Kerr, J., Greenberg, D. and Helmchen, F. (2005). Imaging input and output of neocortical networks in vivo. Proc Natl Acad Sci USA *102*, 14063–14068.

[Kirkby et al., 2010] Kirkby, P., Naga-Srinivas-Nadella, K. and Silver, R. (2010). A compact acousto-optic lens for 2D and 3D femtosecond based 2-photon microscopy. Opt Express *18*, 13720–13744.

[Koester et al., 1999] Koester, H., Baur, D., Uhl, R. and Hell, S. (1999). Ca^{2+} fluorescence imaging with pico- and femtosecond two-photon excitation: signal and photodamage. Biophys J *77*, 2226–2236.

[Kostal et al., 2007] Kostal, L., Lansky, P. and Rospars, J. (2007). Neuronal coding and spiking randomness. Eur J Neurosci *26*, 2693–2701.

[Kremer et al., 2008] Kremer, Y., Leger, J., Lapole, R., Honnorat, N., Candela, Y., Dieudonne, S. and Bourdieu, L. (2008). A spatio-temporally compensated acousto-optic scanner for two-photon microscopy providing large field of view. Opt Express *16*, 10066–10076.

[Kuchibhotla et al., 2009] Kuchibhotla, K., Lattarulo, C., Hyman, B. and Bacskai, B. (2009). Synchronous hyperactivity and intercellular calcium waves in astrocytes in Alzheimer mice. Science *323*, 1211–1215.

[Kurtz et al., 2006] Kurtz, R., Fricke, M., Kalb, J., Tinnefeld, P. and Sauer, M. (2006). Application of multiline two-photon microscopy to functional in vivo imaging. J Neurosci Methods *151*, 276–286.

[Larson et al., 2003] Larson, D., Zipfel, W., Williams, R., Clark, S., Bruchez, M., Wise, F. and Webb, W. (2003). Water-soluble quantum dots for multiphoton fluorescence imaging in vivo. Science *300*, 1434–6.

[Lechleiter et al., 2002] Lechleiter, J., Lin, D. and Sieneart, I. (2002). Multi-photon laser scanning microscopy using an acoustic optical deflector. Biophys J *83*, 2292–2299.

[Lefort et al., 2009] Lefort, S., Tomm, C., Sarria, J. F. and Petersen, C. (2009). The excitatory neuronal network of the C2 barrel column in mouse primary somatosensory cortex. Neuron *29*, 301–316.

[Li et al., 2008] Li, Y., Hooser, S. V., Mazurek, M., White, L. and Fitzpatrick, D. (2008). Experience with moving visual stimuli drives the early development of cortical direction selectivity. Nature *456*, 952–956.

[Lichtman and Sanes, 2008] Lichtman, J. and Sanes, J. (2008). Ome sweet ome: what can the genome tell us about the connectome. Curr Opin Neurobiol *18*, 346–353.

[Lillis et al., 2008] Lillis, K., Eng, A., White, J. and Mertz, J. (2008). Two-photon imaging of spatially extended neuronal network dynamics with high temporal resolution. J Neurosci Methods *172*, 178–184.

[Llinas and Jahnsen, 1982] Llinas, R. and Jahnsen, H. (1982). Electrophysiology of mammalian thalamic neurones in vitro. Nature *297*, 406–8.

[Luebke and Feldmeyer, 2007] Luebke, J. and Feldmeyer, D. (2007). Excitatory signal flow and connectivity in a cortical column: focus on barrel cortex. Brain Struct Funct *212*, 3–17.

[Lütcke et al., 2010] Lütcke, H., Murayama, M., Hahn, T., Margolis, D., Astori, S., zum Alten Borgloh, S. M., Göbel, W., Yang, Y., Tang, W., Kügler, S., Sprengel, R., Nagai, T., Miyawaki, A., Larkum, M., Helmchen, F. and Hasan, M. (2010). Optical recording of neuronal activity with a genetically-encoded calcium indicator in anesthetized and freely moving mice. Front in Neural Circuits *29*, 4–9.

[Mank et al., 2008] Mank, M., Santos, A., Direnberger, S., Mrsic-Flogel, T., Hofer, S., Stein, V., Hendel, T., Reiff, D., Levelt, C., Borst, A., Bonhoeffer, T., Hübener, M. and Griesbeck, O. (2008). A genetically encoded calcium indicator for chronic in vivo two-photon imaging. Nat Methods *5*, 805–811.

[Maravall et al., 2000] Maravall, M., Mainen, Z., Sabatini, B. and Svoboda, K. (2000). Estimating intracellular calcium concentrations and buffering without wavelength ratioing. Biophys J *78*, 2655–2667.

[Markram et al., 1995] Markram, H., Helm, P. and Sakmann, B. (1995). Dendritic calcium transients evoked by single back-propagating action potentials in rat neocortical pyramidal neurons. J Physiol *485*, 1–20.

[Mrsic-Flogel et al., 2007] Mrsic-Flogel, T., Hofer, S., Ohki, K., Reid, R., Bonhoeffer, T. and Huebenerbener, M. (2007). Homeostatic regulation of eye-specific responses in visual cortex during ocular dominance plasticity. Neuron *54*, 961–972.

[Nakazawa et al., 1988] Nakazawa, M., Nakashima, T. and Kubota, H. (1988). Optical pulse compression using a TeO_2 acousto-optical light deflector. Optics Letters *13*, 120–122.

[Niesner et al., 2007] Niesner, R., Andresen, V., Neumann, J., Spiecker, H. and Gunzer, M. (2007). The power of single and multibeam two-photon microscopy for high-resolution and high-speed deep tissue and intravital imaging. Biophys J *93*, 2519–2529.

[Nikolenko et al., 2007] Nikolenko, V., Poskanzer, K. and Yuste, R. (2007). Two-photon photostimulation and imaging of neural circuits. Nat Methods *4*, 943–950.

[Nikolenko et al., 2008] Nikolenko, V., Watson, B., Araya, R., Woodruff, A., Peterka, D. and Yuste, R. (2008). SLM Microscopy: Scanless two-photon imaging and photostimulation with spatial light modulators. Front Neural Circuits *2*, 5.

[Nimmerjahn et al., 2004] Nimmerjahn, A., Kirchhoff, F., Kerr, J. and Helmchen, F. (2004). Sulforhodamine 101 as a specific marker of astroglia in the neocortex in vivo. Nat Methods *1*, 31–37.

[Nimmerjahn et al., 2009] Nimmerjahn, A., Mukamel, E. and Schnitzer, M. (2009). Motor behavior activates Bergmann glial networks. Neuron *62*, 400–412.

[Ogawa et al., 1992] Ogawa, S., Tank, D., Menon, R., Ellermann, J., Kim, S., Merkle, H. and Ugurbil, K. (1992). Intrinsic signal changes accompanying sensory stimulation: functional brain mapping with magnetic resonance imaging. Proc Natl Acad Sci USA *89*, 5951–5955.

[Ohki et al., 2005] Ohki, K., Chung, S., Ching, Y., Kara, P. and Reid, R. (2005). Functional imaging with cellular resolution reveals precise micro-architecture in visual cortex. Nature *433*, 597–603.

[Ohki et al., 2006] Ohki, K., Chung, S., Kara, P., Huebener, M., Bonhoeffer, T. and Reid, R. (2006). Highly ordered arrangement of single neurons in orientation pinwheels. Nature *442*, 925–928.

[Otsu et al., 2008] Otsu, Y., Bormuth, V., Wong, J., Mathieu, B., Dugue, G., Feltz, A. and Dieudonne, S. (2008). Optical monitoring of neuronal activity at high frame rate with a digital random-access multiphoton (RAMP) microscope. J Neurosci Methods *173*, 259–270.

[Otzenberger et al., 2005] Otzenberger, H., Gounot, D., Marrer, C., Namer, I. and Metz-Lutz, M. (2005). Reliability of individual functional MRI brain mapping of language. Neuropsychology *19*, 484–93.

[Ozden et al., 2008] Ozden, I., Lee, H., Sullivan, M. and Wang, S. (2008). Identification and clustering of event patterns from in vivo multiphoton optical recordings of neuronal ensembles. J Neurophysiol *100*, 495–503.

[Pologruto et al., 2003] Pologruto, T., Sabatini, B. and Svoboda, K. (2003). ScanImage: flexible software for operating laser scanning microscopes. Biomed Eng Online *2*, 13.

[Ramdya and Engert, 2008] Ramdya, P. and Engert, F. (2008). Emergence of binocular functional properties in a monocular neural circuit. Nat Neurosci *11*, 1083–1090.

[Reddy et al., 2008] Reddy, G., Kelleher, K., Fink, R. and Saggau, P. (2008). Three-dimensional random access multiphoton microscopy for functional imaging of neuronal activity. Nat Neurosci *11*, 713–20.

[Rickgauer and Tank, 2009] Rickgauer, J. and Tank, D. (2009). Two-photon excitation of channelrhodopsin-2 at saturation. Proc Natl Acad Sci U S A *106*, 15025–30.

[Rochefort et al., 2009] Rochefort, N., Garaschuk, O., Milos, R., Narushima, M., Marandi, N., Pichler, B., Kovalchuk, Y. and Konnerth, A. (2009). Sparsification of neuronal activity in the visual cortex at eye-opening. Proc. Natl. Acad. Sci. USA *106*, 15049–15054.

[Rothschild et al., 2010] Rothschild, G., Nelken, I. and Mizrahi, A. (2010). Functional organization and population dynamics in the mouse primary auditory cortex. Nat Neurosci *13*, 271–3.

[Rudin et al., 2003] Rudin, M., Mueggler, T., Allegrini, P., Baumann, D. and Rausch, M. (2003). Characterization of CNS disorders and evaluation of therapy using structural and functional MRI. Anal Bioanal Chem *377*, 973–81.

[Sabatini and Svoboda, 2000] Sabatini, B. and Svoboda, K. (2000). Analysis of calcium channels in single spines using optical fluctuation analysis. Nature *408*, 589–593.

[Saggau, 2006] Saggau, P. (2006). New methods and uses for fast optical scanning. Curr Opin Neurobiol *16*, 543–550.

[Sakmann, 2006] Sakmann, B. (2006). Patch pipettes are more useful than initially thought: simultaneous pre- and postsynaptic recording from mammalian CNS synapses in vitro and in vivo. Pfluegers Arch *453*, 249–59.

[Salome et al., 2005] Salome, R., Kremer, Y., Dieudonne, S., Leger, J., Krichevsky, O., Wyart, C., Chatenay, D. and Bourdieu, L. (2005). Ultrafast random-access scanning in two-photon microscopy using acousto-optic deflectors. J Neurosci Methods *154*, 161–74.

[Sasaki et al., 2008] Sasaki, T., Takahashi, N., Matsuki, N. and Ikegaya, Y. (2008). Fast and accurate detection of action potentials from somatic calcium fluctuations. J Neurophysiol *100*, 1668–1676.

[Sato et al., 2007] Sato, T., Gray, N., Mainen, Z. and Svoboda, K. (2007). The functional microarchitecture of the mouse barrel cortex. PLoS Biol *5*, e189.

[Scanziani and Hausser, 2009] Scanziani, M. and Hausser, M. (2009). Electrophysiology in the age of light. Nature *461*, 930–9.

[Schiller et al., 1995] Schiller, J., Helmchen, F. and Sakmann, B. (1995). Spatial profile of dendritic calcium transients evoked by action potentials in rat neocortical pyramidal neurones. J Physiol *487*, 583–600.

[Silberberg et al., 2005] Silberberg, G., Grillner, S., LeBeau, F., Maex, R. and Markram, H. (2005). Synaptic pathways in neural microcircuits. Trends Neurosci *28*, 541–51.

[Silberberg et al., 2002] Silberberg, G., Gupta, A. and Markram, H. (2002). Stereotypy in neocortical microcircuits. Trends Neurosci *25*, 227–30.

[Smetters et al., 1999] Smetters, D., Majewska, A. and Yuste, R. (1999). Detecting action potentials in neuronal populations with calcium imaging. Methods *18*, 215–21.

[Squirrell et al., 1999] Squirrell, J., Wokosin, D., White, J. and Bavister, B. (1999). Long-term two-photon fluorescence imaging of mammalian embryos without compromising viability. Nat Biotechnol *17*, 763–767.

[Stosiek et al., 2003] Stosiek, C., Garaschuk, O., Holthoff, K. and Konnerth, A. (2003). In vivo two-photon calcium imaging of neuronal networks. Proc Natl Acad Sci USA *100*, 7319–7324.

[Sumbre et al., 2008] Sumbre, G., Muto, A., Baier, H. and Poo, M. (2008). Entrained rhythmic activities of neuronal ensembles as perceptual memory of time interval. Nature *456*, 102–106.

[Svoboda et al., 1997] Svoboda, K., Denk, W., Kleinfeld, D. and Tank, D. (1997). In vivo dendritic calcium dynamics in neocortical pyramidal neurons. Nature *385*, 161–5.

[Svoboda and Yasuda, 2006] Svoboda, K. and Yasuda, R. (2006). Principles of two-photon excitation microscopy and its applications to neuroscience. Neuron *50*, 823–39.

[Tabor et al., 2008] Tabor, R., Yaksi, E. and Friedrich, R. (2008). Multiple functions of GABA A and GABA B receptors during pattern processing in the zebrafish olfactory bulb. Eur J Neurosci *28*, 117–127.

[Takahashi et al., 2007] Takahashi, N., Sasaki, T., Usami, A., Matsuki, N. and Ikegaya, Y. (2007). Watching neuronal circuit dynamics through functional multineuron calcium imaging (fMCI). Neurosci Res *58*, 219–225.

[Takano et al., 2007] Takano, T., Tian, G., Peng, W., Lou, N., Lovatt, D., Hansen, A., Kasischke, K. and Nedergaard, M. (2007). Cortical spreading depression causes and coincides with tissue hypoxia. Nat Neurosci *10*, 754–762.

[Theer and Denk, 2006] Theer, P. and Denk, W. (2006). On the fundamental imaging-depth limit in two-photon microscopy. J Opt Soc Am A *23*, 3139–49.

[Tian et al., 2009] Tian, L., Hires, S., Mao, T., Huber, D., Chiappe, M., Chalasani, S., Petreanu, L., Akerboom, J., McKinney, S., Schreiter, E., Bermann, C., Jayaraman, V., Svoboda, K. and Looger, L. (2009). Imaging neural activity in worms, flies and mice with improved GCaMP calcium indicators. Nat Methods *6*, 875–881.

[Treacy, 1969] Treacy, E. (1969). Optical pulse compression with diffraction gratings. IEEE J Quantum Electron *5*, 454–458.

[van Hateren and Ruderman, 1998] van Hateren, J. and Ruderman, D. (1998). Independent component analysis of natural image sequences yields spatio-temporal filters similar to simple cells in primary visual cortex. Proc Biol Sci *265*, 2315–2320.

[Vogelstein et al., 2009] Vogelstein, J., Watson, B., Packer, A., Yuste, R., Jedynak, B. and Paninski, L. (2009). Spike inference from calcium imaging using sequential Monte Carlo methods. Biophys J *97*, 636–655.

[Vucinic and Sejnowski, 2007] Vucinic, D. and Sejnowski, T. (2007). A compact multiphoton 3D imaging system for recording fast neuronal activity. PLoS ONE *2*, e699.

[Wallace et al., 2008] Wallace, D., zum Alten Borgloh, S. M., Astori, S., Yang, Y., Bausen, M., Kügler, S., Palmer, A., Tsien, R., Sprengel, R., Kerr, J., W, W. D. and Hasan, M. (2008). Single-spike detection in vitro and in vivo with a genetic Ca^{2+} sensor. Nature Methods *5*, 797–804.

[Waters and Helmchen, 2006] Waters, J. and Helmchen, F. (2006). Background synaptic activity is sparse in neocortex. J Neurosci *26*, 8267–8277.

[Welker and Woolsey, 1974] Welker, C. and Woolsey, T. (1974). Structure of layer IV in the somatosensory neocortex of the rat: Description and comparison with the mouse. J Comp Neurol *158*, 437–454.

[Wilt et al., 2009] Wilt, B., Burns, L., Wei, H. E., Ghosh, K., Mukamel, E. and Schnitzer, M. (2009). Advances in light microscopy for neuroscience. Annu Rev Neurosci *32*, 435–506.

[Winship and Murphy, 2008] Winship, I. and Murphy, T. (2008). In vivo calcium imaging reveals functional rewiring of single somatosensory neurons after stroke. J Neurosci *28*, 6592–6606.

[Xu and Stroud, 1992] Xu, J. and Stroud, R. (1992). Acousto-Optic Devices. John Wiley and Sons Inc. , New York.

[Yaksi and Friedrich, 2006] Yaksi, E. and Friedrich, R. (2006). Reconstruction of firing rate changes across neuronal populations by temporally deconvolved Ca^{2+} imaging. Nat Methods *3*, 377–383.

[Yaksi et al., 2007] Yaksi, E., Judkewitz, B. and Friedrich, R. (2007). Topological reorganization of odor representations in the olfactory bulb. PLoS Biol *5*, e178.

[Yaksi et al., 2009] Yaksi, E., von Saint Paul, F., Niessing, J., Bundschuh, S. and Friedrich, R. (2009). Transformation of odor representations in target areas of the olfactory bulb. Nat Neurosci *12*, 474–482.

[Yu et al., 2005] Yu, X., Wadghiri, Y., Sanes, D. and Turnbull, D. (2005). In vivo auditory brain mapping in mice with Mn-enhanced MRI. Nat Neurosci *8*, 961–968.

[Yuste and Tank, 1996] Yuste, R. and Tank, D. (1996). Dendritic integration in mammalian neurons, a century after Cajal. Neuron *16*, 701–716.

[Zeng et al., 2007] Zeng, S., Lv, X., Bi, K., Zhan, C., Li, D., Chen, W., Xiong, W., Jacques, S. and Luo, Q. (2007). Analysis of the dispersion compensation of acousto-optic deflectors used for multiphoton imaging. J Biomed Opt *12*, 024015.

[Zeng et al., 2006] Zeng, S., Lv, X., Zhan, C., Chen, W., Xiong, W., Jacques, S. and Luo, Q. (2006). Simultaneous compensation for spatial and temporal dispersion of acousto-optical deflectors for two-dimensional scanning with a single prism. Optics Letters *31*, 1091–1093.

[Zhang et al., 2007] Zhang, F., Aravanis, A., Adamantidis, A., de Lecea, L. and Deisseroth, K. (2007). Circuit-breakers: optical technologies for probing neural signals and systems. Nat Rev Neurosci *8*, 577–581.

[Zipfel et al., 2003] Zipfel, W., Williams, R. and Webb, W. (2003). Nonlinear magic: multiphoton microscopy in the biosciences. Nat Biotechnol *21*, 1369–77.

List of Figures

List of Tables

List of Abbreviations

ΔF_Θ: acoustic frequency bandwidth
$\Delta F/F$: relative calcium fluorescence signal
ν_D: total diffraction efficiency
Θ: half AOD scan angle
λ: optical wavelength
d: laser beam diameter
D: active aperture
f_c: AOD center frequency
T_{access}: access time
TB: time-bandwidth product
f_{TL} or f_{SL}: focal length of scan or tube lens

A/D: analog to digital
AM: acetoxymethyl ester
AOD: acousto-optic deflector
AOM : acousto-optic modulator
AP: action potential
A.U: arbitrary units
BD: binocular disparity
BE: beam expander
BOLD: blood oxygen concentration
BS: polarizing beam splitter
CBF: cerebral blood flow
CBV: cerebral blood volume
CLT: cylindrical lens telescope
CNS: central nervous system
DAQ: data acquisition
DC: dichroic beam splitter
DDS: Direct Digital Synthesis
DM: dichroic mirror
DMSO: dimethylsulfoxid
DCU: dispersion compensation unit
EEG: electroencephalography
EPSP: excitatory postsynaptic potential
fMRI: functional magnetic resonance imaging
FOV: field of view
FPGA: Free Programmable Gate Array
FROG: Frequency Resolved Optical Gating
FSI: fluorescence signal intensity
FWHM: full width half maximum
GABA: gamma-aminobutyric acid
GDD: group-delay dispersion
GECI: genetically expressed Ca^{2+} indicator
GFP: green fluorescent protein
IPSP: inhibitory postsynaptic potential
IR: infrared
Lys: lysine
M0, M1: broadband mirrors
NA: numerical aperture
NIR: near infrared
NRR: Normal Rat Ringer
OCIM: On-cell integration mode
OD: ocular dominance
OGB: Oregon Green BAPTA
P: radio frequency input power
PC: Pockels cell
PMT: photomultiplier
RAPS: random access pattern scanning
RF: radio frequency
ROI: region of interest
S.D.: standard deviation
S.E.M.: standard error of the mean
SL: scan lens
SNR: signal-to-noise ratio
SR 101: sulforhodamine 101
TEM: Transverse Electromagnetic Mode
TeO_2: Tellurium Dioxide
Ti:Sa: Titanium Sapphire
TL: tube lens
TPS: targeted path scanning
2PLSM: 2-Photon Laser Scanning Microscopy
VAL: valine

A Supplementary Movies and Materials

1. Supplementary Movies

Supplementary Movie 1:
Image stack from mouse barrel cortex. 2-photon image stack acquired with the AOD scanning system, showing neocortical cell populations stained with OGB-1 (green) and SR101 (red). Images were taken at 4-μm z-steps and are shown from the pial surface down to about 300 μm depth.

Supplementary Movie 2:
Peeling algorithm for spike train extraction. Schematic illustration of the peeling algorithm for automated spike train reconstruction from calcium indicator fluorescence traces. The algorithm is exemplified on a $\Delta F/F$ trace, for which six iterations of the algorithm were necessary to resolve five superimposed calcium transients at 10 Hz.

Supplementary Movie 3:
Sensory-evoked population spiking dynamics in mouse barrel cortex. Spatiotemporal spiking activity of the 56 neurons shown in Fig. 5.19 evoked by the first air-puff in each of the eight trials. Responses to all trials are shown in parallel for the time window of 60 ms surrounding each first whisker stimulation. The movie frame duration was artificially set to 1 ms. Spike times for all neuron were reconstructed with the peeling algorithm. The occurrence of a spike is color-coded in red, whereby the color saturation (from light to dark and again to light) follows a Gaussian time course with the appropriate 95%-confidence interval (10.4 ms) to indicate the uncertainty in spike detection.

Supplementary Movie 4:
Schematic illustration of random-access scanning. This illustration shows how random-access imaging can substantially improve scanning speed, by reducing the scanning regions or regions of interest to simple point-pattern that were scanned on cell somata. For a more realistic illustration real images from L2/3 neurons in mouse neocortex (imaging depth about 200 μm) were used.

2. Scan-Software design in LabView - Flowcharts This appendix section provides a short overview of the main software components that were developed during this thesis in the LabView programming environment. The flow-charts show the coarse and fine organization of the main software components as follows:

- 1. Illustration of the complete LabView scanning software
- 2. Schematic of the main LabView program that is runned on a PC
- 3. Schematic of the FPGA Software that is compiled and runned with the FPGA with a loop repetition rate of 20 MHz

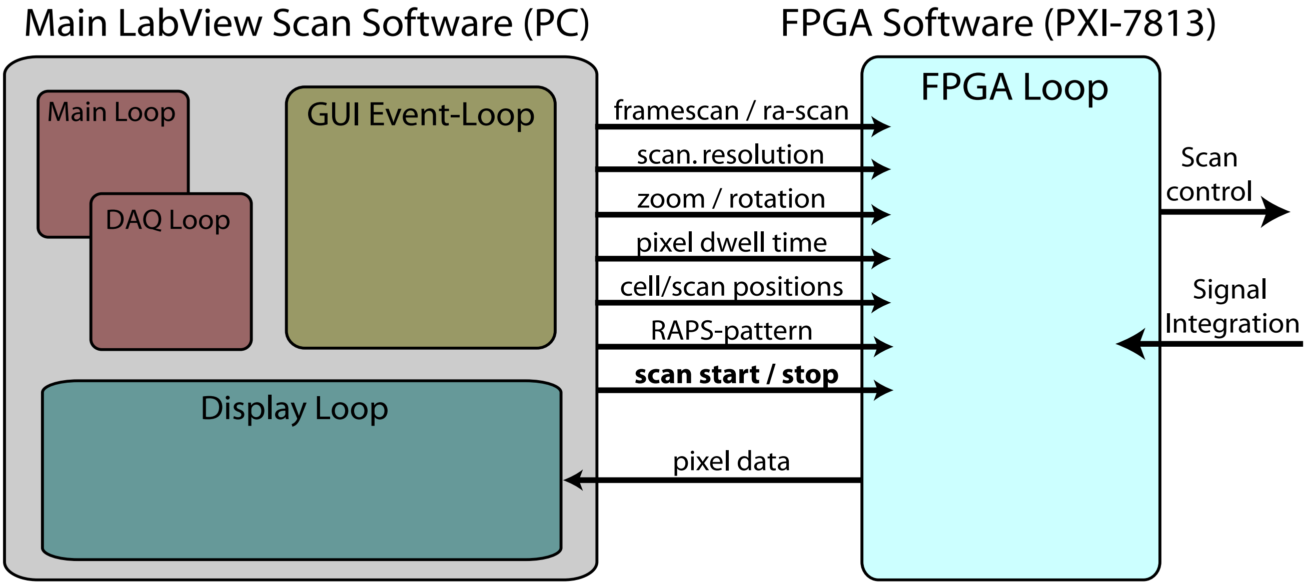

Figure .1: *Flowchart of the complete LabView program*

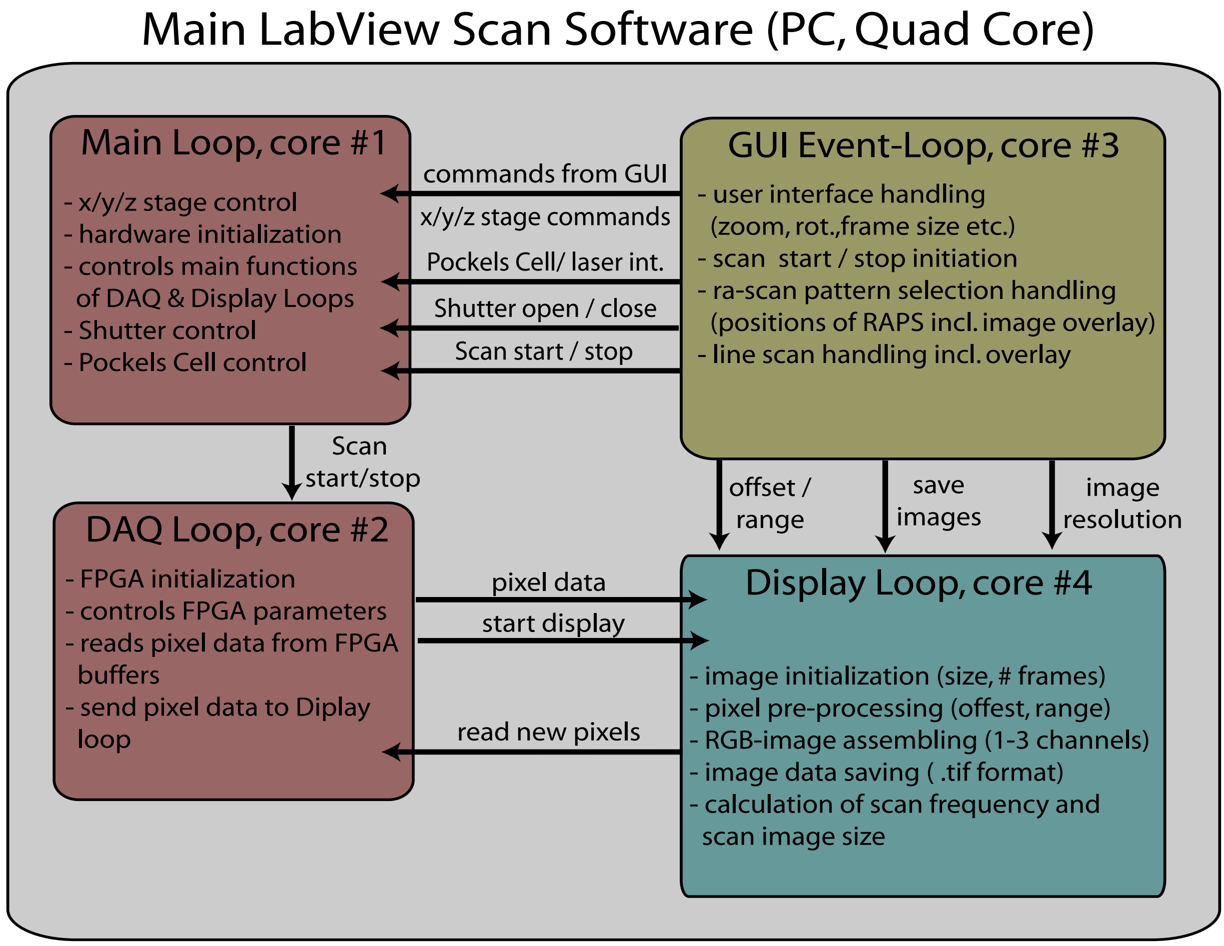

Figure .2: *Flowchart main LabView program*

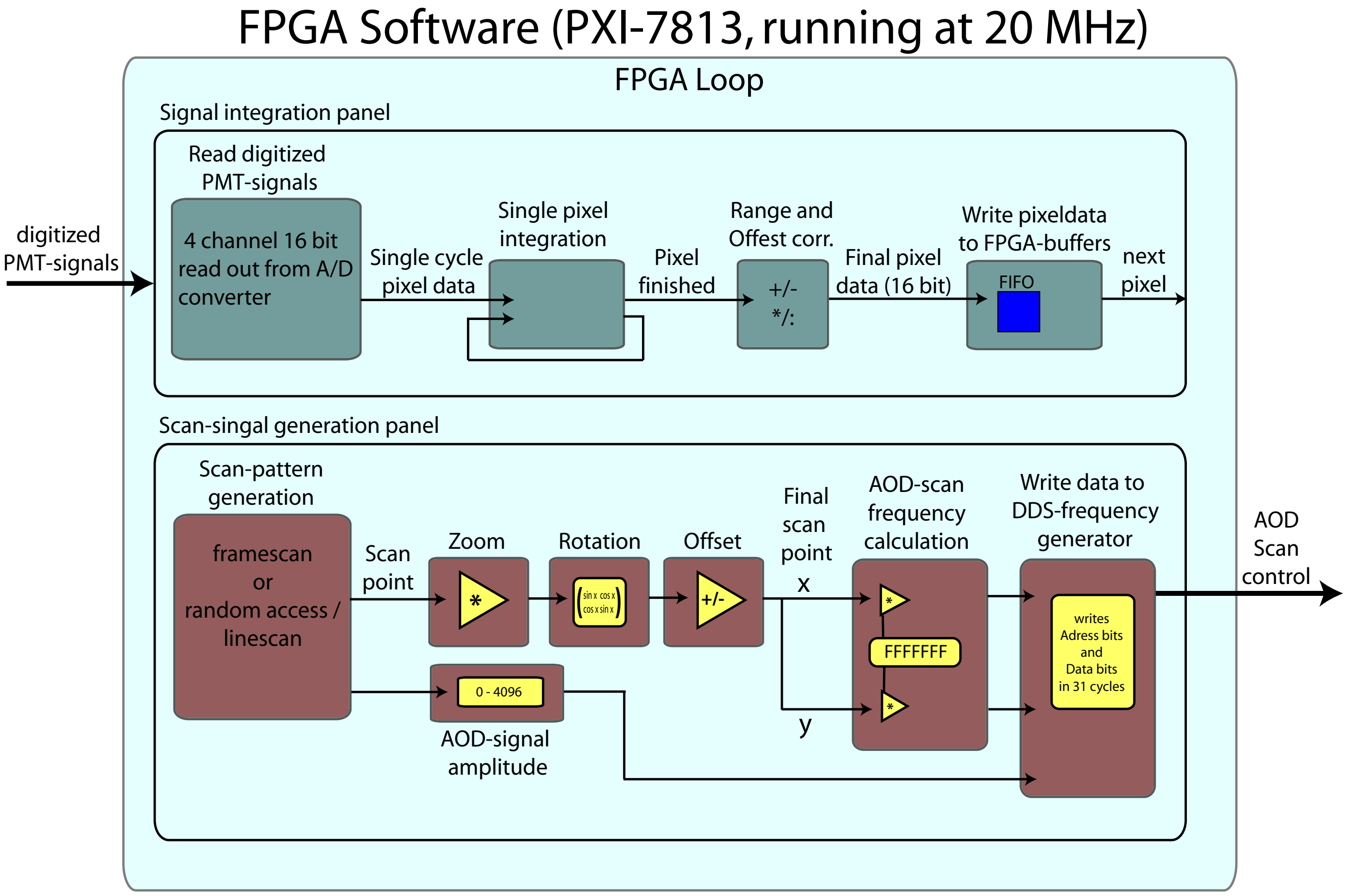

Figure .3: *Flowchart of the FPGA program*

3. The construction of an Acousto-optic-Deflector in MATLAB

Derived from [Xu and Stroud, 1992, Goutzoulis and Pape, 1994] this MATLAB core routine calculates the dimensions and the diffraction efficiency of an acousto-optic device for preset parameters. Before running the program the following parameters have to be assigned accordingly: the acousto-optic bandwidth (BW), the AOD access time (TAU), the refractive index of the acousto-optic material (INDEXI, INDEXD), the sound velocity of the acousto-optic crystal (VEL), a geometrical factor for the shape of the acousto-optic crystal (M2), the RF-frequency input power (p) and the AOD-center frequency (FCENTER). The outputs of the program are: (1) the length of the transducer that is attached to the acousto-optic crystal, (2) the transducer center-to-center spacing, (3) the number of transducers on the acousto-optic element, (4) the transducer high, (5) the AOD incident angle of the laser beam. When the size of the transducer is known, the acousto-optic crystal can be designed to adequately match the minimal requested size given by the piezoelectric transducer.

```
% XY-AOD-Design for two-photon applications
% by B.Grewe
%**************************************************************************
%**************************************************************************
clear all
tic

%Variable Declaration

PI = 3.14159;
LAM = 8.5E-07;
KI = 2*PI/LAM;
BW = 36000000;      % acousto-optic bandwith
TAU = 0.000015;     %acess time in sec
INDEXI = 2.26;      %refractive index TeO2
INDEXD = 2.26;
VEL = 650;          %sound velocity in crystal
M2 = 7.3E-13;       %geometric value of the AODs
ALPHA0 = 12.9;
ALPHAL=ALPHA0*log(10)/10;
B=-26.4;
P=0.03;             %Input Power in Watts /100
C=0.33;
FCENTER=9.4E+07;    %center Frequency

%AOD-calculations
XC=(LAM*FCENTER/(VEL*INDEXI));
BRAGGC = atan((XC)/sqrt(1-XC^2));
TRANL = C*8*INDEXI*VEL^2/(BW^2*LAM);
D = LAM*(INDEXI-(LAM*C/TRANL))/(((INDEXI-(LAM*C/TRANL))^2)+((LAM*FCENTER/VEL)^2)-↙
INDEXD^2);
W=0.742*D;
if ((TRANL/D)/2 - ((TRANL/D)/2) >=0.5)
    N=INT(TRANL/D)+1;
else
    N=(TRANL/D);
end;
TRANL=D*N;
TRANH=VEL*sqrt((TAU*abs(1-2*B))/FCENTER);
fprintf ('TRANSDUCER LENGTH =%f \n ', TRANL);
fprintf ('TRANSDUCER ELEMENT LENGTH = %f \n ',W);
fprintf ('TRANSDUCER CENTER-TO-CENTER SPACING IS= %f \n ',D);
fprintf ('NUMBER OF TRANSDUCER ELEMENT IS = %f \n ',N);
fprintf ('TRANSDUCER HEIGHT IS = %f \n ',TRANH);
fprintf ('ILLUMINATION ANGLE IS = %f \n ', BRAGGC);
BRAGGC=0.0516;
FSTART=FCENTER-(0.5*BW);
FSTOP=FCENTER+(0.5*BW);
RESPOINTS=300;
FRES=BW/RESPOINTS;
idx = 1:RESPOINTS;
DIFF = zeros(idx,1);
```

```
FrequX = zeros(RESPOINTS,1);
frun=1;

for F = FSTART:FRES:FSTOP

    FrequX(frun,1)= FSTART+(frun*FRES*1.5);
    XF=LAM*F/(2*VEL*INDEXI);
    BRAGGF=atan((XF)/sqrt(1-XF^2));
    GAM=BRAGGF-BRAGGC;

    if (GAM==0)
        GAM=1E-32;
     end;

        K=2*PI*F/VEL;
        BETA=(K*W/2)*sin(GAM);
        ALPHA=(K*D/2)*(sin(GAM)-sin(PI/(K*D)));

    if (ALPHA==0)
        ALPHA=1E-32;
    end;

        ETAAO=((KI^2*P*M2*TRANL)/(8*TRANH*(cos(BRAGGC))^2))*(1/N^2)*((2/PI)^2)*((sin(BETA) ↙
/BETA)^2)*((sin(N*ALPHA)/sin(ALPHA))^2);
        ETAALPH=(1-exp(-ALPHAL*((((F)/1E+09))^2)*TAU*1000000))/(ALPHAL*((((F)/1E+09))^2) ↙
*TAU*1000000);
        ETA=ETAAO*ETAALPH;
        ITEN=sin(sqrt(ETA))^2*10000;
        DIFF(frun,1) = ITEN;

  frun = frun+1;
end;

%Plotting the diffraction effciency
figure('name', 'Diffraction Efficinecy');
hold on;
plot(FrequX,DIFF);
title('Diffraction Efficinecy');
grid on;
xlabel('acoustiv frequency (MHz)');
ylabel('Diffraction Efficinecy % / 2.5 Watt');

axis([FrequX(1) 11.3E+07 0 100] );

tic
toc
```

Acknowledgements

Among many other people I would like to especially thank:

- Prof. Dr. Fritjof Helmchen for sharing a lot of his fascinating ideas with me and for his continuous outstanding support, his personal commitment and his great help during my Ph.D. project.
- Prof. Dr. Richard Hahnloser and Prof. Dr. Markus Rudin for joining my steering committee and for lively and helpful discussions about the progress of this project.
- Dr. Bjoern Kampa for his great support and help to perform the first in vivo experiments and for helpful comments on the manuscripts.
- Hans-jörg Kasper for his great electronic and hardware support during this project.
- Dominik Langer for providing the basic concept of the AOD-Scan-Software in LabView
- Stefan Giger for building and designing special holders, detectors and other things in the mechanical workshop.
- Helge Johannssen for fruitful discussions about novel biological applications.
- Dr. Henry Lütcke for the great help with MATLAB programing.
- Martin Wieckhorst for his excellent support in all issues of mechanics, electronics.
- Dr. Helmut Grewe and David Margolis for proof reading of the manuscript.
- Roland Schoeb for his great IT-support and the continuous coffee supply.

Curriculum vitae

Grewe, Benjamin Friedrich

Birth place: Ahlen, Germany
Birth date: December 14, 1980
Parents: Dr. rer. nat. Helmut Grewe, Rosmarie Grewe
Nationality: German
Phone: +41-4463-53328
Fax: +41-4463-53303
Email: grewe@hifo.uzh.ch

Education

2007-2010	University of Zürich, Brain Research Institute, Zurich, Switzerland, PhD, Neurosciences
2003-2006	Ruperto-Carola University of Heidelberg, Heidelberg, Germany Diploma, physics
2001-2003	Christian-Albrecht University, Kiel, Germany Intermediate diploma, physics
1991-2000	Max-Planck Gymnasium, Kiel, Germany Abitur (A-level courses: physics and mathematics)

Research and Professional Experience

2007-2010	ETH, Zurich, Switzerland, PhD-student (Advisors: F. Helmchen, R. Hahnloser & M. Rudin)
2005-2007	Max-Planck-Institute for Medical Research, Heidelberg, Germany, diploma student (Advisor: Bert Sakmann), Research into neuronal backpropagation of dendrites
2004-2005	Ruperto-Carola University of Heidelberg, Heidelberg, Germany, scientific assistant, Faculty of Medicine
2003-2005	Ruperto-Carola University of Heidelberg, Heidelberg, Germany, teaching assistant, physics
2002-2003	Christian-Albrecht University, Kiel, Germany, teaching assistant, biology

Other Training & Professions

2008-present	PhD-student representative of the Brain Research Institute
2007-present	Founding of the Institutes SOLA runners-club “HIFO-Hitchhikers”
2007-present	Language centre of ETH Zurich, Switzerland New Greek language studies
2003-2006	Institute of foreign language studies, Heidelberg, Germany Italian language studies, Diploma
2000-2001	Civil Service, Malteser Foundation, Kiel, Germany

Publications

Theses

1. **Benjamin F. Grewe**, 2006
   "*Dendritic Signaling in L5A Pyramidal Neurons of the Somatosensory Cortex.*"
   Diploma thesis in physics, supervisor: Bert Sakmann, Ruperto-Carola University of Heidelberg, Germany

Articles

1. **Benjamin F. Grewe**, Audrey Bonan and Andreas Frick, 2010
   "Backpropagation of realistic action potential output along apical and basal dendrites of slender-tufted L5A pyramidal neurons" (Front in Cell Neurosc, 2010, *18*:4-13)

2. **Benjamin F. Grewe**, Dominik Langer, Björn Kampa and Fritjof Helmchen, 2010
   "High-speed in vivo calcium imaging reveals spike trains in neuronal networks with near-millisecond precision." (Nature Methods, 2010, *7*:399-405)

3. **Benjamin F. Grewe** and Fritjof Helmchen, 2009
   "Optical probing of neuronal ensemble activity"
   (Curr. Opin. Neurobiology, 2009, *19*:520-9)

4. Mélissa Farinelli, Fabrice Heitz, **Benjamin F. Grewe**, Shiva Tyagarajan, Fritjof Helmchen, and Isabelle Mansuy.
   "*Protein Phosphatase-1 Promotes Neuroprotection by Modulating NR2B-Containing NMDA Receptors*" (submitted)

5. Jeanne Ster, José María Mateos, **Benjamin F. Grewe**, Fritjof Helmchen and Urs Gerber
   "*Activation of group II metabotropic glutamate receptors inhibits mossy fiber transmission while exciting pyramidal cells and interneurons in rat hippocampus*"
   (in preparation)

Book Chapters

1. **Benjamin F. Grewe** and Fritjof Helmchen,
   "High-speed two-photon calcium imaging of neuronal population activity using acousto-optic deflectors", (in: Imaging in Neuroscience, a Laboratory Manual;
   editors: F. Helmchen and A. Konnerth, CSHL press, Woodbury, NY, in press)

Conference abstracts and proceedings (*selected*)

1. **36th SFN annual meeting,** Atlanta USA, 2006,
   Grewe, Benjamin, Frick, *"Forward and backward propagation of dendritic signals in slender-tufted L5A pyramidal neurons of somatosensory cortex in vitro"* (Poster)
2. **Cellular and molecular neurobiology of mental diseases**, Giessbach, Switzerland,2008, Grewe Benjamin & Helmchen, *"Fast scanning approaches for imaging of cortical activity in vivo"* (Poster)
3. **Computation in neuro-circuits,** Ascona, Switzerland, 2008
   Grewe, Benjamin & Helmchen, *"Development of a fast acousto-optic scanner for two-photon imaging of neuronal networks"* (Poster & Talk)
4. ***opt*ETH PhD-student symposium**, Zürich 2008
   "*High-speed two-photon calcium imaging of neuronal network dynamics in vivo using acousto-optic scanners*", Zürich, Switzerland (Poster)
5. **39th SFN annual meeting,** Chicago, USA, 2009
   Benjamin F. Grewe, Dominik Langer, Björn Kampa, Fritjof Helmchen, 2009, "*High-speed two-photon calcium imaging of neuronal network dynamics in vivo using acousto-optic scanners*" (Poster)
6. **Brain-Fair Zürich**, public day, April 2009 & March 2010
   "*Wie verarbeitet unser Gehirn Informationen?*" (General Poster, in German)
7. **Neural Networks *in silico* workshop**, Max Planck Florida Institute, Jupiter, USA, 2010
   "*High-speed two-photon calcium imaging of neuronal network dynamics in vivo using acousto-optic scanners*" (*Talk*)
8. **Imaging brain circuits in health and disease***,* Jacques-Monod Conference, Roscoff, 2010, "*Current applications of acousto-optic high-speed imaging in the intact brain"* (*Talk*)

Invited talks

1. Dept. of Cellular Physiology (A.Konnerth) , LMU, Munich, Germany, 2009
   "*High-speed two-photon calcium imaging of neuronal network dynamics in vivo using acousto-optic scanners*"
2. Max-Planck-Institut für Neurobiologie (T.Bonhoeffer), Münich, Germany, 2009,
   "*High-speed two-photon calcium imaging of neuronal network dynamics in vivo using acousto-optic scanners*"
3. Max-Planck-Institut für Biologische Kybernetik (J.Kerr), Tübingen, Germany, 2009
   "*High-speed two-photon calcium imaging of neuronal network dynamics in vivo using acousto-optic scanners*"
4. Neuroscience Dept. of Physiology, UCL (T.Margrie), London, GB, 2010
   "*High-speed two-photon calcium imaging of neuronal network dynamics in vivo using acousto-optic deflectors*"
5. ETH- Zürich, Microscopy & Nanoscopy Conference, May 2010
   "High-speed calcium imaging of neuronal signals mediated by acousto optic deflection"
6. Dept. of Neurobiology, Harvard Med. School (Reid RC), Boston MA, USA, June 2010
   "High-speed optical probing of neuronal network activity in the intact mouse brain"